

SYNAPTIC, CIRCUIT, AND BEHAVIORAL INSIGHTS INTO CDKL5 DEFICIENCY DISORDER

Sheng Tang

A DISSERTATION

in

Neuroscience

Presented to the Faculties of the University of Pennsylvania

in

Partial Fulfillment of the Requirements for the

Degree of Doctor of Philosophy

2018

Supervisor of Dissertation

Co-Supervisor of Dissertation

Zhaolan (Joe) Zhou, Ph.D.

Douglas A. Coulter, Ph.D.

Associate Professor of Genetics

Professor of Pediatrics

Graduate Group Chairperson

Joshua I. Gold, Ph.D., Professor of Neuroscience

Dissertation Committee

Eric D. Marsh, M.D., Ph.D., Associate Professor of Neurology

Michael Granato, Ph.D., Professor of Cell and Developmental Biology

Marc V. Fuccillo, M.D., Ph.D., Assistant Professor of Neuroscience

Ethan M. Goldberg, M.D., Ph.D., Assistant Professor of Neurology

SYNAPTIC, CIRCUIT, AND BEHAVIORAL INSIGHTS INTO CDKL5 DEFICIENCY DISORDER

COPYRIGHT

2018

Sheng Tang

This work is licensed under the
Creative Commons Attribution-
NonCommercial-ShareAlike 3.0
License

To view a copy of this license, visit

<https://creativecommons.org/licenses/by-nc-sa/3.0/us/>

ACKNOWLEDGMENT

To my thesis advisors:

Thank you, Joe, for taking on a first-year graduate student who knew virtually nothing about either brains or mice and entrusting him with and challenging him to an incredibly difficult yet rewarding project. Over the last four years, you have provided a tremendous amount of resources to allow me to pursue my unique training path, and in the process, helped me learn a great deal about science and about being a scientist. I would not have come this far without your consistent support and wise advice.

Thank you, Doug, for your generosity in adopting and mentoring a student armed with little more than the audacity to try a new kind of science. Your capacity for constant innovation and your willingness to collaborate with others who think differently are what make your laboratory an exhilarating place to be. There is nothing quite like working with “live” brain, and no matter where I go and what kind of science I move on to, being an electrophysiologist will always be part of my identity.

To my former and current colleagues:

Thank you, Judy, for teaching me most of what I know about rodent behavior and the inner thoughts of mice. I could not have come this far without your mentorship, and your work in the CDKL5 field has left a lasting legacy that will continue to grow.

Thank you, Yolanda, for being the caretaker of thousands of mice and having an astounding genotyping accuracy that all of us continue to take for granted. Without your competence and attention to detail, our mouse colony would probably be a box of mystery chocolates.

Thank you, Barbara, for being my partner on the CDKL5 project and for sharing with me the countless challenges and rare triumphs along the path forward. I argue that a GFP-labeled neuron does not truly glow green until two have seen it. It has been a rewarding experience to work with you, and our dialogue has not only made me a better scientist but also changed my perspective of science for the better.

Thank you, Cuiyong, for showing a clueless and clumsy graduate student how to “patch-clamp.” Without your mentorship and encouragement, I would still be patching and clamping onto extracellular debris rather than actual cells.

Thank you, Haji, for being the engineer who has a solution to every problem. Few of my experiments would have succeeded without your building many of the necessary components – and occasionally, entire electrophysiologic rigs – from scratch.

And thank you, to all of my colleagues in the Zhou and Coulter labs, past and present. Your intellect, kindness, and work ethic continue to inspire me every day.

To my thesis committee:

Thank you, Eric, Michael, Marc, and Ethan for always having my best interests at heart. Each of you has brought a unique perspective, offering feedback that has allowed me to see my project in a different light. You have challenged me to design audacious experiments and undertake high-risk science, but at the same time, you have also been the much-needed reality check, showing tremendous empathy and understanding that science is difficult and rarely gives us what we expect.

Thank you, NGG, BGS, and MSTP, for admitting me to your programs and providing the means for my training at Penn. You deserve credit for having effective training programs for young scientists and doctors, but you deserve even more credit for building a community of bright, enthusiastic, and diverse people.

Thank you, my friends in Philadelphia and afar, for your support. It is inspiring to know that most non-scientists actually care very much about science, and your understanding of what I do has provided me with a much-needed connection to the world outside my bench and rig.

Thank you, my parents, Yan Shen and Yongrui Tang. I do not remember much about our first years in America, but I know that it was not easy. Your drive, perseverance, and faith in a brighter future are the reasons I am writing these sentences today. This dissertation is dedicated to you.

I would like to acknowledge my funding sources and awards that I have received, including NIH T32HD083185, T32GM007170, F30NS100433, the Hearst Foundation Fellowship (2015), the NIMH MD/PhD Student Conference Travel Award (2015), and the Jameson-Hurvich Travel Award (2017).

ABSTRACT

SYNAPTIC, CIRCUIT, AND BEHAVIORAL INSIGHTS INTO CDKL5 DEFICIENCY DISORDER

Sheng Tang

Zhaolan (Joe) Zhou

Douglas A. Coulter

Mutations in the X-linked cyclin-dependent kinase-like 5 (*CDKL5*) gene cause a severe neurodevelopmental disorder named CDKL5 deficiency disorder (CDD). In humans, CDD is characterized by early-onset epilepsy, severe intellectual disability, autistic features, and various comorbidities. Mice lacking functional CDKL5 protein show a constellation of behavioral deficits, including impaired learning and memory, reduced sociability, and increased stereotypy, that are reminiscent of human symptoms. Despite its simple genetic etiology, how the loss of CDKL5 leads to the unique symptomatology of CDD is not well understood. Using genetically modified mouse models of CDD, we dissect the cellular origins of behavioral, circuit, and synaptic phenotypes in CDD. We find that impaired learning and memory primarily originates from CDKL5 loss in forebrain glutamatergic neurons, whereas autistic-like features primarily originate from CDKL5 loss in forebrain GABAergic neurons. At the cellular and circuit level, loss of CDKL5 in glutamatergic neurons leads to altered pyramidal neuron morphology and concomitant changes in excitatory and inhibitory synaptic transmission, resulting in disrupted spatiotemporal dynamics of microcircuits. In contrast, loss of CDKL5 in GABAergic neurons leads to a non-cell autonomous change in excitatory synaptic transmission and circuit hyperexcitability. Consistent with this finding, acute pharmacologic reduction of glutamatergic synaptic signaling rescues selective phenotypes of CDD in mice. Taken together, our results suggest that CDKL5 plays distinct roles in forebrain glutamatergic and GABAergic neurons to regulate cellular morphology, synaptic function, and circuit excitability, and that modulation of synaptic transmission provides a novel therapeutic avenue to treat CDD.

TABLE OF CONTENTS

ACKNOWLEDGMENT	III
ABSTRACT	V
LIST OF ILLUSTRATIONS	IX
CHAPTER 1 - INTRODUCTION	1
Overview	1
The Genetics and Clinical Features of CDKL5 Deficiency Disorder	2
CDKL5 Protein: Molecular Features and Expression Profiles	4
Generation and Characterization of CDKL5-Deficient Mice	5
Network, Circuit, and Cellular Phenotypes of CDKL5-Deficient Mice	6
Genetic Dissection of the Cellular Origins of CDD-Related Phenotypes	7
CHAPTER 2 – LOSS OF CDKL5 IN GLUTAMATERGIC NEURONS DISRUPTS HIPPOCAMPAL MICROCIRCUITRY AND LEADS TO MEMORY IMPAIRMENT IN MICE	9
Abstract	9
Introduction	10
Results	12
Nex-cKO mice exhibit impaired hippocampal-dependent learning and memory	12
Altered morphology of CA1 pyramidal neurons of Nex-cKO mice	14
Enhanced excitatory synaptic activity in CA1 pyramidal neurons of Nex-cKO mice	15
Enhanced inhibitory synaptic activity in CA1 pyramidal neurons of Nex-cKO mice	17
Disrupted spatiotemporal dynamics of the CA1 microcircuit in Nex-cKO mice	18
Discussion	20
Materials and Methods	26
Figures	42

CHAPTER 3 – GABAERGIC NEURON DYSFUNCTION AND ALTERED GLUTAMATERGIC SIGNALING UNDERLIE AUTISTIC-LIKE FEATURES IN CDKL5-DEFICIENT MICE	58
Abstract.....	58
Introduction	59
Results	61
Mice lacking CDKL5 in GABAergic neurons show autistic-like features	61
Dlx-cKO mice show a non-cell autonomous enhancement of excitatory synaptic transmission	63
Dlx-cKO mice show aberrant paired-pulse facilitation leading to circuit hyperexcitability	63
Acute NMDAR blockade ameliorates autistic-like features in CDKL5-deficient mice.....	64
Discussion.....	66
Materials and Methods	69
Figures	78
CHAPTER 4 – CDKL5 REGULATES THE ELABORATION OF THE DENDRITIC TREE IN ADULT MICE	88
Abstract.....	88
Introduction	89
Results	90
Reduced dendritic complexity in CDKL5-deficient mice in adulthood.....	90
Loss of CDKL5 limits dendritic arborization.....	91
Unaltered dendritic spine density in CDKL5-deficient mice.....	92
Discussion.....	92
Materials and Methods	94
Figures	95
CHAPTER 5 – EXTENDED DISCUSSION AND FUTURE DIRECTIONS.....	99
Cellular Origins of CDKL5 Deficiency Disorder-Related Phenotypes.....	99
Epilepsy in CDKL5 Deficiency Disorder	99
Phenotypic Heterogeneity in CDKL5 Deficiency Disorder	100
CDKL5 Deficiency Disorder and Interspecies Differences	101

BIBLIOGRAPHY 103

LIST OF ILLUSTRATIONS

Chapter 2

Figure 1. Generation of Nex-cKO mice and validation of conditional knockout strategy.....	p42
Figure 2. Assessment of home-cage locomotion, anxiety-related behavior, motor coordination, olfaction, repetitive behavior, nesting, and hind limb clasping in Nex-cKO mice.....	p43
Figure 3. Unaltered sociability in Nex-cKO mice.	p44
Figure 4. Impaired hippocampal-dependent learning and memory in Nex-cKO mice...p45	
Figure 5. Decreased dendritic complexity in CA1 pyramidal neurons of Nex-cKO mice.....	p46
Figure 6. Analysis of spine density and morphology in CA1 pyramidal neurons of Nex-cKO mice.	p48
Figure 7. Unaltered intrinsic membrane properties in CA1 pyramidal neurons of Nex-cKO mice.	p49
Figure 8. Increased mEPSC frequency in CA1 pyramidal neurons of Nex-cKO mice...p50	
Figure 9. Unaltered AMPA/NMDA ratio in CA1 pyramidal neurons of Nex-cKO mice...p51	
Figure 10. Increased mIPSC frequency in CA1 pyramidal neurons of Nex-cKO mice..p52	
Figure 11. Disrupted spatiotemporal dynamics of the CA1 microcircuit in Nex-cKO mice.....	p53
Figure 12. VSDI summary data, standardization of stimulus intensity, and paired-pulse ratio.	p55
Figure 13. Model of synaptic and circuit abnormalities in Nex-cKO mice.	p57

Chapter 3

Figure 1. Generation and validation of mice lacking CDKL5 selectively in forebrain GABAergic neurons (Dlx-cKO).	p78
Figure 2. Dlx-cKO mice show unaltered locomotion, anxiety-related behavior, and motor coordination.	p79
Figure 3. Dlx-cKO mice show preserved learning and memory, but impaired cognitive flexibility.	p80

Figure 4. Dlx-cKO mice show reduced sociability, increased stereotypic behaviors and impaired nesting.p81

Figure 5. Unaltered inhibitory synaptic transmission at CA1 pyramidal neurons in Dlx-cKO mice.p82

Figure 6. Dlx-cKO mice show a non-cell autonomous enhancement of excitatory synaptic transmission.p83

Figure 7. Dlx-cKO mice show aberrant paired-pulse facilitation.p84

Figure 8. Generation of CDKL5 R59X knock-in mice.....p85

Figure 9. Acute NMDAR blockade ameliorates autistic-like features, but not learning and memory, in CDKL5-deficient mice.p86

Chapter 4

Figure 1. Reduced dendritic complexity of hippocampal CA1 pyramidal neurons in adult CDKL5 R59X mice.p95

Figure 2. Unaltered dendritic complexity of hippocampal CA1 pyramidal neurons in juvenile CDKL5 R59X mice.p96

Figure 3. Loss of CDKL5 limits dendritic arborization in adulthood.....p97

Figure 4. Unaltered spine density of hippocampal CA1 pyramidal neurons in juvenile and adult CDKL5 R59X mice.p98

CHAPTER 1 - INTRODUCTION

Overview

Since the first reports linking the X-linked cyclin-dependent kinase-like 5 (*CDKL5*) gene to a severe childhood epileptic encephalopathy, *CDKL5* deficiency disorder (CDD) has come to be recognized as an independent clinical entity that has features distinct from classic Rett syndrome and other neurodevelopmental disorders (Fehr et al., 2012; Kalscheuer et al., 2003; Tao et al., 2004; Weaving et al., 2004). To date, at least several hundred cases of CDD have been reported worldwide, with the majority of patients being heterozygous females. Clinically, early-onset epilepsy is the most prominent feature of CDD, with seizures persisting throughout life despite treatment. Developmental delay is common, with most patients experiencing a range of comorbid symptoms that can include motor dysfunction, intellectual disability, communication deficit, feeding and gastrointestinal problems, sleep disturbance, and breathing abnormalities.

The establishment of mouse models of CDD has confirmed the importance of this gene for proper brain development and neurologic function. In addition, they have provided an *in vivo* setting to discover and validate various protein-protein interactions and signaling pathways involving *CDKL5* and test newly uncovered therapeutics. Importantly, animal models represent an opportunity to address two unanswered questions: 1) What are the most prominent phenotypes in mouse models of CDD at the cellular, circuit, and behavioral levels, and 2) Do the behavior phenotypes arise from shared or distinct cellular and circuit mechanisms?

The Genetics and Clinical Features of CDKL5 Deficiency Disorder

To date, at least several hundred cases of CDD have been recorded, with the incidence of the disorder estimated at 1/500,000 live births (Hector et al., 2017). Prior to the identification of its genetic etiology, most cases of CDD bore other clinical diagnoses, including atypical Rett syndrome, infantile spasms, West Syndrome, and Lennox-Gastaut Syndrome (Hanefeld, 1985; Mirzaa et al., 2013). In 2003, the clinical syndrome was reported for the first time in association with genetic lesions in two patients commonly disrupting *CDKL5* (Kalscheuer et al., 2003). Subsequently, numerous studies confirmed the existence of *CDKL5* mutations in the Hanefeld variant of Rett syndrome characterized by early-onset seizures (Evans et al., 2005; Mari et al., 2005; Scala et al., 2005; Tao et al., 2004; Weaving et al., 2004), and the disorder came to be recognized as an independent clinical entity (Fehr et al., 2012). The vast majority of patients are females heterozygous for a mutation in *CDKL5*, although hemizygous male patients have also been reported.

CDD typically arises from *de novo* mutations in the cyclin-dependent kinase-like 5 (*CDKL5*) gene, which resides in the distal portion of the short arm of the X chromosome (Xp22). The gene was initially named serine-threonine kinase 9 (*STK9*) upon first identification of the DNA sequence, but its protein sequence similarity to CDKL family proteins led to its present name. CDD is distinguished from disorders that involve duplications of *CDKL5*, of which a small number of cases have been reported. These patients have features such as intellectual disability and autistic features, but typically do not suffer from epilepsy (Szafranski et al., 2015).

The most prominent and disabling symptom of CDD is early-onset, treatment-resistant epilepsy (Bahi-Buisson et al., 2008). The prevalence of epilepsy in the disorder

is estimated to be more than 95% in both female and male patients, with the median age of onset at 6 weeks (Bahi-Buisson et al., 2008; Fehr et al., 2016b). The epilepsy associated with CDD is heterogeneous in both presentation and progression, but a subset of patients has been described to involve three distinct stages (Bahi-Buisson et al., 2008). Infantile spasms are common, accompanied by eventual development of myoclonic and tonic-clonic seizures in many patients (Bahi-Buisson et al., 2008; Grosso et al., 2007). Electrographic features such as slowing of background activity, focal and multifocal discharges, and burst suppression have been reported, with significant heterogeneity in presentation and progression of electroclinical features across case studies (Klein et al., 2011; Melani et al., 2011). The long-term efficacy of anti-epileptic drugs is low, with one study reporting a 12-month responder rate of 24% (Müller et al., 2016).

Although seizures are typically the presenting symptom of CDD, patients suffer from significant comorbidities, including profound intellectual disability, language deficit, motor impairment, autonomous dysfunction, gastrointestinal issues, and sleep disturbance (Bahi-Buisson et al., 2008; Fehr et al., 2016a; Mangatt et al., 2016). Interestingly, male patients appear, on average, to have greater impairment of motor function as compared to female patients (Fehr et al., 2016a). Patients with truncating mutations outside the catalytic domain may have milder symptoms (Fehr et al., 2016b; 2015), but the establishment of clear genotype-phenotype correlations have been hampered by the limited size of patient cohorts. In addition to the differential impact of various mutations in *CDKL5*, random X-chromosome inactivation likely contributes to the clinical heterogeneity in female patients (Hagebeuk et al., 2013; Weaving et al., 2004). In order to better understand the clinical progression of CDD and its associated

comorbidities, at least one major international effort has been initiated to conduct a coordinated natural history study.

CDKL5 Protein: Molecular Features and Expression Profiles

The CDKL5 protein is highly conserved among vertebrates, with 96% identity at the amino acid level between the mouse and human orthologues of CDKL5. Nearly all pathogenic missense mutations in patients cluster within the amino(N)-terminal kinase domain of *CDKL5*, suggesting that perturbed kinase function likely underlies the pathophysiology of the disorder (Hector et al., 2017).

The approximately 300-amino acid catalytic domain of CDKL5 bears significant similarity to that of cyclin-dependent kinases (CDKs) in many organisms (Manning et al., 2002). However, even among the CDKL family, CDKL5 is unique in possessing a long carboxy(C)-terminal domain of about 700 amino acids, a feature that is conserved across most mammalian species (UniProt Consortium, 2018; Zhu et al., 2013). Although previous studies suggest that this C-terminal domain can serve as a negative regulator of CDKL5 kinase activity and is capable of affecting protein sub-cellular localization within heterologous cell lines (Lin et al., 2005; Rusconi et al., 2008), its *in vivo* function remains unclear. In addition, the CDKL5 protein also encodes two putative nuclear localization sequences (NLS) and a nuclear export sequence (NES) within this C-terminal region, suggested to serve in shuttling between the nucleus and cytoplasm (Bertani et al., 2006). However, the limited availability of tools to visualize and tag endogenous CDKL5 *in vivo* has made this result difficult to replicate. Several CDKL5-interacting proteins have been identified, including AMPH1, DNMT1, NGL-1, PSD-95,

MIB1, and SHTN1 (Kameshita et al., 2008; Mertz et al., 2015; Nawaz et al., 2016; Ricciardi et al., 2012; Sekiguchi et al., 2013; Zhu et al., 2013). However, the specific cellular context and functional significance of these interactions remain unclear.

Although multiple *CDKL5* isoforms have been identified, one major isoform is highly enriched in the brains of humans, rats, and mice (Hector et al., 2016). Within the brain, there is evidence that CDKL5 protein is expressed most highly in neurons of the forebrain and at relatively low levels in glia (Kang et al., 2011; Wang et al., 2012; Zeisel et al., 2015; Zhang et al., 2014). In addition to its localization in the nuclear and cytoplasmic compartments (Rusconi et al., 2008), CDKL5 has been found, in multiple studies, to also be localized at the postsynaptic density, sites of excitatory synapses (Bayés et al., 2012; Reim et al., 2017; Ricciardi et al., 2012; Zhu et al., 2013). CDKL5 also follows an interesting temporal expression pattern, present at relatively low levels embryonically and rising during early postnatal development (Hector et al., 2016).

Generation and Characterization of CDKL5-Deficient Mice

The high level of conservation of its sequence, expression pattern, and localization motivated the generation of an animal model to study the *in vivo* functions of CDKL5. The first *Cdkl5* constitutive knockout (KO) mice were generated via the deletion of mouse *Cdkl5* exon 6, mimicking a splice site mutation in a patient that resulted in the skipping of corresponding human *CDKL5* exon 7 (Wang et al., 2012). No full-length functional CDKL5 protein was detectable in the brains of these *Cdkl5* KO mice. Male KO mice exhibited normal growth, brain and body weight, and lack of gross brain pathology (Wang et al., 2012). However, a battery of behavioral assays revealed adult *Cdkl5* KO

mice to have deficits in multiple domains, including alterations in anxiety-related phenotypes, locomotion activity, impaired motor coordination, social interaction deficits, increased repetitive behaviors, and impaired learning and memory (Wang et al., 2012), mirroring the numerous comorbidities of human CDD. Furthermore, *Cdkl5* KO mice showed abnormal auditory event-related potentials (ERPs) reflective of long-range circuit communication deficits (Wang et al., 2012). Three subsequent studies, two of which generated independent *Cdkl5* KO alleles, replicated the majority of these behavioral findings (Amendola et al., 2014; Jhang et al., 2017; Okuda et al., 2018), although some discrepancies exist, likely due to differences in background strains, protocols, and specific parameters in assessing behavioral phenotypes.

Network, Circuit, and Cellular Phenotypes of CDKL5-Deficient Mice

To date, a total of three distinct *Cdkl5* KO mouse lines have been generated (Amendola et al., 2014; Okuda et al., 2017; Wang et al., 2012). The lack of spontaneous seizures and obvious electrographic abnormalities in adult *Cdkl5* KO mice, despite EEG monitoring at multiple ages, has been a surprising but consistent finding. Seizure threshold in *Cdkl5* KO mice has also been assessed through the use of chemoconvulsants, including kainate and N-methyl-D-aspartic acid (NMDA) (Amendola et al., 2014; Okuda et al., 2017). Both juvenile (4-week) and adult (13 week) *Cdkl5* KO mice were found to be differentially susceptible to NMDA, but not kainate (Okuda et al., 2017), suggesting a potential underlying change in network excitability.

At the cellular level, neuronal morphology has been consistently found to be altered *in vitro* in cultured neurons upon CDKL5 knockdown and *in vivo* in *Cdkl5* KO

mice. Specifically, dendritic arborization is reduced in multiple brain regions in adult *Cdkl5* KO mice (Amendola et al., 2014; Fuchs et al., 2014; Tang et al., 2017). Spine density has also been found to be altered, but the specific changes have been context-dependent, with some studies discovering an excess of “immature” spines and others discovering reduced spine number and stability (Ricciardi et al., 2012; Sala et al., 2016). Related to these morphologic changes, excitatory synaptic activity (Ricciardi et al., 2012; Sala et al., 2016; Tang et al., 2017), microcircuit activity (Tang et al., 2017), and synaptic plasticity in the form of long-term potentiation (Okuda et al., 2017; Sala et al., 2016) have all been found to be altered, although the specific changes again appear to be highly context-dependent.

Genetic Dissection of the Cellular Origins of CDD-Related Phenotypes

An imbalance in excitation and inhibition (E/I) is thought to be a fundamental network mechanism that underlies behavioral abnormalities in neurodevelopmental disorders (Rubenstein and Merzenich, 2003). The balancing forces of excitation and inhibition are apparent in the cellular architecture of many brain regions, particularly the cortex and hippocampus, where excitatory glutamatergic pyramidal neurons are modulated by inhibitory GABAergic interneurons (Harris and Mrsic-Flogel, 2013; Tremblay et al., 2016). A disruption of either glutamatergic or GABAergic signaling, resulting in an overall E/I imbalance, is a frequent finding in animal models, with many studies demonstrating changes originating at the synaptic level (Lee et al., 2017; Nelson and Valakh, 2015). For specific disorders, the underlying mechanism of E/I imbalance has been attributed to the dysfunction of subsets of genetically defined neurons, in that conditional knockout mice are capable of recapitulating many of the phenotypes of the

respective constitutive knockout (Chao et al., 2010; Judson et al., 2016). These findings have not only provided mechanistic insight into the circuit and network changes that generate abnormal behavior, but also motivated the investigation of specific cell- and circuit-based therapies that seek to ameliorate behavioral deficits (Sahin and Sur, 2015; Tyson and Anderson, 2014).

In mice, CDKL5 expression is highest in the forebrain, but found in both excitatory glutamatergic and inhibitory GABAergic neurons (Johnson et al., 2017; Wang et al., 2012). The complex constellation of phenotypes found in *Cdkl5* KO mice raises an intriguing question: do these behavioral phenotypes originate from common or distinct cellular and circuit mechanisms? More specifically, how does the loss of CDKL5 lead to the dysfunction of glutamatergic and GABAergic neurons and consequently, the neuronal circuits and networks that generate behavior? Similar to previous studies involving *Mecp2* and *Ube3a* (Chao et al., 2010; Judson et al., 2016), we took advantage of genetic Cre-expressing mouse lines (Goebbels et al., 2006; Monory et al., 2006) that defined these broad classes of neurons and began our investigation through the generation of *Cdkl5* conditional knockout (cKO) mice. By conducting assays at multiple levels, we sought to 1) dissect the cellular origins of the behavioral phenotypes of CDD in mice, and 2) gain mechanistic insight into the roles of CDKL5 in synaptic and circuit function.

CHAPTER 2 – LOSS OF CDKL5 IN GLUTAMATERGIC NEURONS DISRUPTS
HIPPOCAMPAL MICROCIRCUITRY AND LEADS TO MEMORY IMPAIRMENT IN
MICE

Adapted from: Tang S, Wang ITJ, Yue C, Takano H, Terzic B, Pance K, Lee JY, Cui Y, Coulter DA, Zhou Z. Loss of CDKL5 in glutamatergic neurons disrupts hippocampal microcircuitry and leads to memory impairment in mice. *Journal of Neuroscience*. 2017 Jul;3:0539-17.

Abstract

CDKL5 deficiency disorder (CDD) is a neurodevelopmental disorder characterized by epileptic seizures, severe intellectual disability, and autistic features. Mice lacking cyclin-dependent kinase-like 5 (CDKL5) display multiple behavioral abnormalities reminiscent of the disorder, but the cellular origins of these phenotypes remain unclear. Here, we find that ablating CDKL5 expression specifically from forebrain glutamatergic neurons impairs hippocampal-dependent memory in male conditional knockout mice. Hippocampal pyramidal neurons lacking CDKL5 show decreased dendritic complexity but a trend toward increased spine density. This morphological change is accompanied by an increase in the frequency of spontaneous miniature EPSCs and interestingly, miniature IPSCs. Using voltage-sensitive dye imaging to interrogate the evoked response of the CA1 microcircuit, we find that CA1 pyramidal neurons lacking CDKL5 show hyperexcitability in their dendritic domain that is constrained by elevated inhibition in a spatially and temporally distinct manner. These results suggest a novel role for CDKL5 in the regulation of synaptic function and uncover an intriguing microcircuit mechanism underlying impaired learning and memory.

Introduction

CDD is characterized by early-onset epilepsy, severe intellectual disability, autistic features, and various comorbidities (Bahi-Buisson and Bienvenu, 2012; Fehr et al., 2016a; Kalscheuer et al., 2003; Weaving et al., 2004). It is caused by mutations in the X-linked gene, cyclin-dependent kinase-like 5 (*CDKL5*), a member of a highly conserved family of serine-threonine kinases (Kilstrup-Nielsen et al., 2012). Mice that constitutively lack *CDKL5* recapitulate several key features of the disorder, including impaired hippocampal-dependent memory, deficits in motor coordination, and autistic-like phenotypes such as reduced sociability and increased repetitive behavior (Amendola et al., 2014; Fuchs et al., 2014; 2015; Wang et al., 2012). However, the cellular origins and circuit mechanisms contributing to these phenotypes have yet to be identified, thus limiting the insight into the pathogenic mechanisms that underlie CDD.

Cdkl5 mRNA and protein expression is highly enriched in neurons of the forebrain (Wang et al., 2012), where glutamatergic and GABAergic cell types predominate (Hébert and Fishell, 2008; Poulin et al., 2016). In excitatory neurons, *CDKL5* has been found to localize to the postsynaptic density, where it interacts with postsynaptic density protein 95 (PSD-95), netrin-G1 ligand (NGL-1), and Rac1 (Chen et al., 2010; Ricciardi et al., 2012; Zhu et al., 2013). *CDKL5* knockdown or constitutive knockout result in changes in the dendritic branching, spine density, and synaptic function of glutamatergic neurons (Chen et al., 2010; Ricciardi et al., 2012; Sala et al., 2016; Zhu et al., 2013). However, the directionality of these changes appears to be highly context-dependent. For example, shRNA-mediated knockdown of *CDKL5* in cultured mouse hippocampal neurons leads to an increase in immature spine numbers (Ricciardi et al., 2012), whereas downregulation of *CDKL5* by the *in utero* electroporation

of an shRNA construct in the rat reduces overall spine density (Zhu et al., 2013). In adult *Cdkl5* constitutive knockout mice, both spine stability and spine density are reduced in the somatosensory cortex (Sala et al., 2016). Given that CDKL5 is also expressed in GABAergic neurons (Rusconi et al., 2008), the extent to which these cellular and morphological phenotypes are the result of cell-autonomous dysfunction in excitatory neurons or a consequence of loss of CDKL5 in GABAergic neurons remain unknown. Furthermore, how these cellular phenotypes contribute to functional deficits at the synapse, circuit, and even behavioral level remains to be determined.

Given that CDKL5 is highly expressed in excitatory neurons and is localized to the postsynaptic density of excitatory synapses, we carried out conditional knockout studies of CDKL5 in excitatory neurons and set out to 1) determine the contribution of excitatory neuronal dysfunction to behavioral abnormalities in CDD, 2) investigate how CDKL5 loss affects dendrite and spine morphology *in vivo* in mice, 3) examine the resulting synaptic and circuit dysfunction in a behaviorally relevant microcircuit. We find that loss of CDKL5 in forebrain excitatory neurons impairs hippocampal-dependent memory and alters neuronal morphology. In addition, hippocampal pyramidal neurons lacking CDKL5 show enhanced spontaneous synaptic activity, evidenced by the elevation of mEPSC and mIPSC frequency. Interestingly, the alteration of synaptic excitation and inhibition leads to a complex, layer-specific disruption of CA1 microcircuit dynamics. Our findings suggest a glutamatergic neuron-specific mechanism for learning and memory impairment in CDD and reveal a novel role for CDKL5 in regulating synaptic and circuit function *in vivo*.

Results

Nex-cKO mice exhibit impaired hippocampal-dependent learning and memory

Cdkl5 constitutive knockout mice exhibit a broad range of behavioral phenotypes, including impaired learning and memory, decreased social behavior, increased repetitive behavior, decreased anxiety-related behavior, and impaired motor coordination (Amendola et al., 2014; Fuchs et al., 2014; 2015; Wang et al., 2012). CDKL5 protein expression is highest in the forebrain (Wang et al., 2012), where glutamatergic and GABAergic neurons predominate. To isolate the cellular origins of CDD-related phenotypes, we generated a mouse line selectively lacking CDKL5 in forebrain excitatory neurons (Nex-cKO), using the Nex-Cre mouse line (Goebbels et al., 2006) (Fig. 1A). We then confirmed the cell type-specific loss of CDKL5 in excitatory neuron-rich regions of the forebrain using western blot analysis of microdissected tissues (Fig. 1B). In whole hippocampal lysates of Nex-cKO mice, CDKL5 protein levels were reduced by ~85% (WT, 0.445, Nex-cKO, 0.068; Mann-Whitney test, $U=0$, $p=0.029$) (Fig. 1C). We first carried out a battery of behavioral tests to assess basic sensory and motor functions, including home-cage locomotion, anxiety-related behavior, rotarod, olfaction, repetitive behavior, and nesting, and found that these behaviors were unaltered in Nex-cKO mice compared to wild type littermates (Fig. 2A-F). Interestingly, we noted the emergence of a robust hind limb clasp phenotype in Nex-cKO starting at around postnatal day (P) 80 that became fully penetrant by approximately P120 (Fig. 2G).

We next assessed sociability and learning and memory, two aspects of behavior impaired in constitutive *Cdkl5* knockout mice that mirror the symptomatology of human CDD (Wang et al., 2012). Compared to wild type littermates, adult Nex-cKO mice demonstrated similar social behavior in the three-chamber social approach test, showing

a strong preference for investigating a novel mouse over a novel object (Fig. 3A,B), as well as similar levels of direct social interaction with a novel mouse (WT, 64.1 ± 7.3 ; Nex-cKO, 53.4 ± 3.9 , Mann-Whitney test, $p=0.55$) (Fig. 3C). In contrast, on the Y-maze test, Nex-cKO mice exhibited significantly decreased spontaneous alternation (WT, $65.9 \pm 2.2\%$; Nex-cKO, $53.9 \pm 2.3\%$; unpaired t-test, $t_{41}=3.737$, $p=0.0006$) (Fig. 4A), suggestive of an impairment in spatial working memory. On the Barnes maze assay, Nex-cKO mice made more errors on both forward (WT, 44.3 ± 5.0 errors; Nex-cKO, 71.8 ± 5.8 errors; unpaired t-test, $t_{26}=2.991$, $p=0.006$) and reversal (WT, 52.1 ± 5.7 errors; Nex-cKO, 71.8 ± 5.8 errors; Mann-Whitney test, $U=19$, $p=0.0005$) probe trials, and showed increased number of perseverations (WT, 2.4 ± 0.4 errors; Nex-cKO, 5.1 ± 0.4 errors; unpaired t-test, $t_{26}=3.896$, $p=0.0006$) to the original target during the reversal probe trial, suggesting a deficit in hippocampal-dependent memory (Fig. 4C-E). Interestingly, Nex-cKO mice also showed modestly increased locomotor activity in specific contexts outside of the home cage, as shown by higher activity during the social choice phase of the social approach assay (WT, 23.4 ± 1.0 m; Nex-cKO, 27.3 ± 0.8 m; Mann-Whitney test, $U=311$, $p=0.0015$) and increased total number of entries on the Y-maze assay (WT, 29.3 ± 1.3 entries; Nex-cKO, 40.2 ± 2.8 entries; unpaired t-test, $t_{41}=3.294$, $p=0.002$) (Fig 3D, 4B). Taken together, of the numerous phenotypes exhibited by *Cdkl5* constitutive knockout mice, Nex-cKO mice appear to recapitulate a relatively isolated impairment in hippocampal-dependent learning and memory upon the loss of CDKL5 from forebrain excitatory neurons.

Altered morphology of CA1 pyramidal neurons of Nex-cKO mice

CDKL5 has been found to interact with proteins that modulate the actin cytoskeleton (Chen et al., 2010) as well as the postsynaptic density (Ricciardi et al., 2012). However, the impact of CDKL5 loss on pyramidal neuron morphology has been highly context-dependent, varying across *in vitro* knockdown studies and *in vivo* studies in *Cdkl5* constitutive knockout mice (Chen et al., 2010; Ricciardi et al., 2012; Sala et al., 2016; Zhu et al., 2013). The Nex-cKO mouse line presented us with a unique opportunity to examine the excitatory neuron-autonomous consequences of CDKL5 loss on cellular morphology. We chose to focus our morphologic studies on CA1 pyramidal neurons, due to 1) previous findings suggesting that CDKL5 expression is highly enriched in the CA1 region (Cembrowski et al., 2016) and 2) the relatively specific impairment in hippocampal-dependent learning and memory phenotype in Nex-cKO mice. By crossing Nex-cKO mice with a Thy1-GFPm allele (Feng et al., 2000), we were able to analyze dendritic complexity and dendritic spine density *in vivo*. Compared to wild type littermates, adult Nex-cKO mice showed a significant decrease in the complexity of the basal and proximal apical dendrites of CA1 neurons, as shown by Sholl analysis (Linear mixed effect model analysis, interaction of genotype and distance from soma; basal dendrites: $F_{19,875}=3.27$, $p=3.12 \times 10^{-6}$; apical dendrites: $F_{23,1051}=2.26$, $p=0.001$) (Fig. 5A-E), confirming the results of a previous RNAi-mediated CDKL5 knockdown study (Chen et al., 2010) and constitutive knockout study (Amendola et al., 2014). In Nex-cKO mice, total basal dendrite length also showed a trend toward a reduction (Linear mixed effect model analysis, fixed effect of genotype (Nex-cKO – WT), $-458.9 \mu\text{m}$, $F_{1,4.42}=4.86$, $p=0.086$) (Fig. 5D). Next, we compared spine density in CA1 pyramidal neurons of wild type and Nex-cKO mice. In Nex-cKO mice, we found, surprisingly, trends toward an

increase in spine density, particularly in the apical dendrites of CA1 pyramidal neurons (Linear mixed effect model analysis, fixed effect of genotype (Nex-cKO – WT), 2.204 spines/10 μm , $F_{1,3.5}=8.22$, $p=0.054$). (Fig. 6B, E). Reconstruction and analysis of spine morphology in three-dimensional confocal image stacks also revealed a trend toward an increase in spine volume in Nex-cKO mice (basal dendritic spines: linear mixed effect model analysis, fixed effect of genotype (Nex-cKO – WT), 0.0234 μm^3 , $F_{1,3.63}=5.88$, $p=0.079$) (Figure 6C, F). Given that spine volume is positively correlated with spine maturity and the strength of the excitatory synapse it contains (Arellano et al., 2007; Harris and Stevens, 1989; Nimchinsky et al., 2002), our findings suggest that CA1 pyramidal neurons in Nex-cKO mice tend to have slightly increased density of morphologically mature dendritic spines.

Enhanced excitatory synaptic activity in CA1 pyramidal neurons of Nex-cKO mice

Because decreased dendritic branching and increased spine volume and density are not typically observed in concert, we next asked how this morphology affected function, particularly related to the intrinsic and synaptic properties of CA1 pyramidal neurons. Using the whole-cell patch-clamp technique in *ex vivo* hippocampal slices, we first investigated the intrinsic membrane properties and input-output properties of CA1 neurons in wild type and Nex-cKO mice. We found no significant differences in the action potential threshold (Linear mixed effect model analysis, $F_{1,5.87}=0.4$, $p=0.551$) (Fig. 7A), input resistance (Linear mixed effect model analysis, $F_{1,5.97}=0.73$, $p=0.427$) (Figure 7B), and an input-output curve correlating the amount of injected current to the number of action potentials (Linear mixed effect model analysis, $F_{6,204.02}=0.75$, $p=0.611$) (Figure 7C), suggesting that CA1 neurons lacking CDKL5 are comparable to wild type neurons

in their intrinsic membrane properties and their ability to generate action potentials. Next, we investigated excitatory synaptic transmission by recording miniature excitatory synaptic currents (mEPSCs). In Nex-cKO mice, we found a significant reduction in mEPSC inter-event intervals (Linear mixed effect model analysis, interaction of genotype and cumulative frequency bin, $F_{19,696}=5.28$, $p=4.63 \times 10^{-12}$), which resulted in a trend toward increased overall mEPSC frequency (Linear mixed effect model analysis, fixed effect of genotype, (Nex-cKO - WT), 0.58 Hz, $F_{1,3.08}=9.57$, $p=0.052$) (Fig. 8B,C), whereas mEPSC amplitude was unaltered (Linear mixed effect model analysis, $F_{1,3.93}=0.28$, $p=0.623$) (Figure 8D-E).

Given the evidence supporting enhanced spontaneous excitatory synaptic activity in Nex-cKO mice, we next asked whether this change represented a specific enhancement of AMPA- or NMDA-dependent currents. To estimate the relative contributions of AMPA- and NMDA-dependent currents in the same neuron, we performed recordings of evoked EPSCs at holding potentials of -70 mV and +40 mV (Etherton et al., 2009; 2011a). Nex-cKO mice showed similar amplitudes of the AMPA- (Fig. 9A,C) and NMDA-dependent EPSC components of evoked EPSCs (Linear mixed effect model analysis, AMPA-EPSC: $F_{1,5.16}=0.27$, $p=0.625$; NMDA-EPSC: $F_{1,4.65}=0.54$, $p=0.498$) (Fig. 9B,D). Importantly, the NMDA/AMPA ratio was unaltered in Nex-cKO mice (Linear mixed effect model analysis, $F_{1,3.44}=0.06$, $p=0.821$). (Fig. 9E). These results suggest that the enhancement of excitatory synaptic activity in Nex-cKO mice is unlikely to be attributed to a specific change in ionotropic glutamate receptor subtype.

Enhanced inhibitory synaptic activity in CA1 pyramidal neurons of Nex-cKO mice

Imbalances in excitation-inhibition (E/I) are commonly found in mouse models of neurodevelopmental disorders and thought to underlie a range of pathologic phenotypes, including impaired learning and memory (Bateup et al., 2013; Kepecs and Fishell, 2014; Nelson and Valakh, 2015; Rubenstein and Merzenich, 2003; Sahin and Sur, 2015; Shcheglovitov et al., 2013; Yizhar et al., 2011). Given our findings of enhanced excitatory synaptic activity in Nex-cKO mice, we next investigated whether the excitatory neuron-specific loss of CDKL5 also affects inhibitory synaptic transmission. To assess inhibition, we carried out whole-cell patch clamp recordings of miniature inhibitory postsynaptic currents (mIPSCs) from CA1 pyramidal neurons in wild type and Nex-cKO mice. To avoid the potential confound of depolarization-induced suppression of inhibition (Wilson and Nicoll, 2001) and other depolarization-induced changes, we used a high-chloride internal solution that allowed the recording of mIPSCs at a voltage near the resting membrane potential of CA1 pyramidal neurons. We found that CA1 pyramidal neurons in Nex-cKO mice showed a significant reduction in mIPSC inter-event intervals (Linear mixed effect model analysis, interaction of genotype and cumulative frequency bin, $F_{19,656}=2.32$, $p=0.001$), which resulted in a trend toward increased mIPSC frequency (Linear mixed effect model analysis, fixed effect of genotype (Nex-cKO – WT), 0.792 Hz, $F_{1,3.5}=7.83$, $p=0.057$) (Fig. 10B,C), whereas mIPSC amplitude was unaltered (Linear mixed effect model analysis, $F_{1,3.5}=0.01$, $p=0.92$) (Fig. 10D,E), suggesting an enhancement in spontaneous inhibitory synaptic activity onto pyramidal neurons. Intriguingly, we also found a significant increase in mIPSC decay time (Linear mixed effect model analysis, fixed effect of genotype (Nex-cKO – WT), 1.356 ms, $F_{1,3.74}=17.2$, $p=0.016$) (Fig. 10G). Together, the enhancement of mIPSC frequency and slowed decay

kinetics in Nex-cKO mice contributed to a significantly enhanced inhibitory charge transfer rate (Linear mixed effect model analysis, fixed effect of genotype (Nex-cKO – WT), 213 pA*ms/s, $F_{1,3.5}=12.86$, $p=0.029$) (Fig. 10H). These results suggest that as a result of CDKL5 loss, CA1 pyramidal neurons in Nex-cKO mice show an enhancement of both spontaneous excitatory and inhibitory synaptic activity.

Disrupted spatiotemporal dynamics of the CA1 microcircuit in Nex-cKO mice

Our whole-cell patch-clamp studies revealed an elevation of both excitatory and inhibitory synaptic activity in Nex-cKO mice. An imbalance of excitation and inhibition, therefore, is not readily apparent from these findings alone. However, our whole-cell recordings assessed synaptic activity only at the soma and did not directly assess the spatiotemporal integration of excitation and inhibition occurring along the dendrites of pyramidal neurons. Given the distinct spatial distribution of excitatory and inhibitory synapses in the dendritic and somatic domains of CA1 pyramidal neurons (Bloss et al., 2016), increases in excitation and inhibition are not likely to “cancel out.” Therefore, we next asked whether circuit function in Nex-cKO mice might be affected in a more complex manner. To investigate the contribution of synaptic changes to a behaviorally-relevant circuit function, we investigated how CA1 pyramidal neurons respond to stimulation at the Schaffer collaterals, a source of monosynaptic excitatory input that is critical for learning and memory *in vivo*. We used voltage-sensitive dye imaging (VSDI), a technique that allows the quantitative analysis of evoked excitatory and inhibitory responses across time and space (Carlson and Coulter, 2008; Coulter et al., 2011). In order to compare Schaffer-evoked responses in CA1 regions of wild type and Nex-cKO mice, we normalized stimulus intensities based on the excitability of individual slices. No

significant differences were found for the half-maximal stimulus intensities (Linear mixed effect model analysis, $F_{1,6.27}=1.1$, $p=0.332$) and the elicited presynaptic fiber volley amplitudes (Linear mixed effect model analysis, $F_{1,8.06}=0.27$, $p=0.619$) in WT and Nex-cKO mice, suggesting that comparable stimuli were used in our VSDI experiments (Fig. 12F, G).

To fully assess both the magnitude and spatial spread of VSDI responses, we generated regions of interest (ROIs) in the *stratum radiatum* (proximal apical dendritic layer) and *stratum pyramidale/oriens* (cell body and basal dendritic layer), both proximal and distal to the site of stimulation (Fig. 11A). In wild type mice, Schaffer collateral stimulation typically evokes a fast, temporally-restricted depolarization in *stratum radiatum* that is followed by a hyperpolarizing response in the *stratum pyramidale/oriens* (Fig. 11B, C, D, F), likely reflective of feedforward/feedback inhibition that is strongest in the perisomatic region (Pouille and Scanziani, 2001). In contrast, Schaffer collateral stimulation in Nex-cKO mice led to a significantly enhanced depolarization in *stratum radiatum* in a region proximal to the stimulus (Linear mixed effect model analysis, interaction of genotype and time, $F_{5,201.55}=3.97$, $p=0.002$; generalized linear hypothesis tests with Holm's method to adjust for multiple comparisons, 8 ms: $z=3.79$, $p=9.06 \times 10^{-4}$; 10 ms: $z=3.01$, $p=0.013$) (Fig. 11F and Fig. 12C), demonstrating dendritic hyperexcitability consistent with the observed increase in spontaneous excitatory synaptic activity. Paired-pulse ratios from extracellular field recordings in the *stratum radiatum* were similar between wild type and Nex-cKO mice (Linear mixed effect model analysis, $F_{1,7.91}=0.002$, $p=0.966$) (Fig. 12I), suggesting that the observed dendritic hyperexcitability is unlikely to be of presynaptic origin, which is also consistent with previous findings localizing CDKL5 to the postsynaptic density (Ricciardi et al., 2012).

Interestingly, in the *stratum pyramidale/oriens* of Nex-cKO mice proximal to the stimulus, we observed an enhancement of both depolarization and hyperpolarization (Linear mixed effect model analysis, interaction of genotype and time, $F_{5,201.30}=7.61$, $p=1.42 \times 10^{-6}$; generalized linear hypothesis tests with Holm's method to adjust for multiple comparisons, 8 ms: $z=3.28$, $p=0.0062$; 10 ms: $z=2.66$, $p=0.039$; 40 ms: $z=-2.38$, $p=0.07$) (Fig. 11D and Fig. 12A), suggesting an increase in perisomatic inhibition that is consistent with our finding of increased spontaneous inhibitory synaptic activity. However, in the *stratum pyramidale/oriens* distal to the site of the stimulus, Nex-cKO mice showed only enhanced hyperpolarization (Linear mixed effect model analysis, of genotype and time, $F_{5,201.20}=2.25$, $p=0.051$; generalized linear hypothesis tests with Holm's method to adjust for multiple comparisons, 20 ms, $z=-3.1$, $p=0.012$) (Fig. 11E and Fig. 12B), suggesting that the spread of excitation is highly constrained in space by enhanced inhibition. Taken together, these results 1) confirm the dual enhancement of both excitatory and inhibitory synaptic activity identified in whole-cell recordings and 2) show that, due to the differential spatial distribution of excitatory and inhibitory synapses, the dual enhancement does not "cancel out" but rather, alters the activation of the CA1 circuit in a spatially and temporally distinct manner (Fig. 13).

Discussion

In this study, we uncover the cellular origins of learning and memory impairment in a mouse model of CDD through the generation of a forebrain excitatory neuron-specific *Cdkl5* knockout line (Nex-cKO). Nex-cKO mice demonstrate impaired hippocampal-dependent memory, along with context-dependent hyperactivity and hind limb claspings. At the cellular level, we observe that altered neuronal morphology in Nex-

cKO mice is accompanied by increased spontaneous excitatory and inhibitory synaptic activity, leading to altered spatiotemporal dynamics in the CA1 microcircuit that is relevant to learning and memory. Together, these findings reveal the glutamatergic origins of learning and memory impairment in CDD and support a novel role for CDKL5 in regulating synaptic and circuit function in glutamatergic neurons.

We chose to focus on male hemizygous conditional knockout mice to examine the role of CDKL5 in excitatory neurons, avoiding the potential confound introduced by random X-inactivation in heterozygous females, which leads to mosaic CDKL5 protein expression. However, because most patients with CDD are female, future studies should aim to determine, in female heterozygous knockout and conditional knockout mice, the nature and extent of cellular and circuit abnormalities, and how these changes are affected by variable patterns of X-inactivation. In this regard, the development of tools to discriminate *Cdkl5* expression at cellular resolution in mosaic females will greatly facilitate the investigation of cellular and circuit endophenotypes and behavioral deficits.

Disruption of hippocampal-dependent memory in Nex-cKO mice

The finding of a relatively isolated deficit in hippocampal-dependent memory in Nex-cKO mice suggests that these symptoms in CDD likely have origins in the glutamatergic neuron, while other features likely arise from different cell types and associated circuits. These results point toward the value of a cell type-specific approach to isolate the cellular signaling changes underlying CDD-related phenotypes. For example, biochemical studies in *Cdkl5* constitutive knockout mice to date have focused on the cortex and hippocampus, regions where glutamatergic neuron types predominate

(Hébert and Fishell, 2008; Poulin et al., 2016). Therefore, the changes in AKT-mTOR pathway activity (Amendola et al., 2014; Sala et al., 2016; Wang et al., 2012) and the phosphorylation of molecules such as GSK3 β (Fuchs et al., 2014; 2015) and HDAC4 (Trazzi et al., 2016) reported likely represent the consequences of CDKL5 loss from glutamatergic neurons. Interestingly, pharmacologic treatment targeting these signaling changes appear to ameliorate learning and memory deficits in *Cdkl5* constitutive knockout mice (Fuchs et al., 2015; Trazzi et al., 2016), although other phenotypes have not yet been examined. Our findings confirm the importance of glutamatergic signaling in hippocampal-dependent learning and memory in CDD, but suggest that other features of CDD may arise from distinct cellular origins and may therefore involve distinct signaling pathways. Therefore, additional studies are necessary to determine the function of CDKL5 in other cell types, which may underlie symptoms such as reduced sociability, altered anxiety-related behavior, and impaired motor coordination. For example, in the forebrain, where CDKL5 expression is enriched, GABAergic neurons constitute a second cell type that merits further investigation.

Similar to reports from *Cdkl5* constitutive knockout mice (Amendola et al., 2014; Wang et al., 2012), we did not find any evidence of spontaneous behavioral seizures in Nex-cKO mice. The contribution of genetic background to seizure susceptibility and differences in brain connectivity between humans and mice (Oh et al., 2014) are likely the cause. However, our results reveal a potential circuit-level mechanism for hyperexcitability, supporting a conserved role for CDKL5 in regulating the excitability of neuronal networks.

Altered CA1 pyramidal neuron morphology in Nex-cKO mice

Our morphological studies reveal two sets of changes that stand in contrast to one another – reduced dendritic complexity and trends toward increased spine density and volume. One possibility is that the reduction in dendritic complexity is a secondary, homeostatic response to altered spine density and morphology and enhanced excitatory synaptic activity. Activity-dependent dendritic retraction is known to occur both *in vivo* and *in vitro* and has been documented in a model of Timothy syndrome involving a mutation in the voltage-gated calcium channel $Ca_v1.2$ (Krey et al., 2013; Wong and Ghosh, 2002). Interestingly, elevated GSK-3 β activity, which is associated with activity-dependent shrinkage of dendrites (Rui et al., 2013), has been found in mouse models of CDD (Fuchs et al., 2014). The converse possibility, altered spine density and morphology being secondary to reduced dendritic complexity, seems less likely in the setting of an overall increase in excitatory synaptic activity in Nex-cKO mice. Because these contrasting findings typically do not accompany each other in models of neurodevelopmental disorders (Penzes et al., 2011), a third possibility is simply that CDKL5 regulates dendrite and synapse development through distinct mechanisms. This hypothesis may be consistent with recent findings in which neuronal activity in immature neurons leads to the induction of CDKL5 protein levels, while neuronal activity in mature neurons leads to the degradation of CDKL5 (La Montanara et al., 2015). CDKL5, therefore, may have distinct functions during stages of development that uniquely affects the processes of dendrite growth, spine generation, and activity-dependent pruning. One such example of a family of kinases that serve two contrasting cellular functions is the doublecortin-like kinases (DLCKs), which promote dendrite growth but suppress synapse maturation (Shin et al., 2013).

Altered synaptic inhibition in Nex-cKO mice

Given that we selectively ablated CDKL5 expression from excitatory neurons, we were surprised to find altered inhibition in Nex-cKO mice. CDKL5 is not believed to interact with inhibitory synaptic proteins (Ricciardi et al., 2012), and it therefore may be tempting to conclude that the observed increase in inhibition in Nex-cKO is a compensatory response by GABAergic cells to mitigate E/I balance. However, such compensatory changes in GABAergic synaptic activity do not typically accompany increased excitatory synaptic activity and circuit hyperexcitability in other animal models (Bateup et al., 2013; Chao et al., 2010; Flavell et al., 2006; Luikart et al., 2011; Tsai et al., 2012). A recent study in constitutive *Cdkl5* knockout mice discovered an upregulation of parvalbumin- and VGAT-positive puncta at the cell bodies of pyramidal neurons in the visual cortex (Pizzo et al., 2016). This finding is consistent with our results, which suggest an enhancement of perisomatic inhibition in the hippocampal CA1 region of Nex-cKO mice. Interestingly, our whole-cell recordings also revealed a significant enhancement of mIPSC decay time, potentially suggesting an alteration in the composition of GABA_A receptor subunits (Goldstein et al., 2002). Therefore, it is possible that CDKL5 also regulates inhibitory synaptic function through a distinct mechanism that has yet to be discovered. For example, CDKL5 kinase activity may regulate the localization and function of postsynaptic scaffolding proteins such as gephyrin or subunits of the GABA receptor in excitatory neurons through post-translational modification.

Disrupted microcircuit dynamics in Nex-cKO mice

Our voltage-sensitive dye imaging results suggest that the enhancement of excitatory and inhibitory synaptic activity do not neatly “cancel out”. Voltage-sensitive dye imaging allowed the analysis of the spread of excitation and inhibition, capturing, in Nex-cKO mice, hyperexcitation that was spatiotemporally constrained by elevated inhibition (Fig. 11 and Fig. 12). Given the interactions of the Schaffer collateral pathway with direct cortical input *in vivo* (Ang et al., 2005; Backus et al., 2016; Colgin, 2016), it is not surprising that such a circuit disturbance could underlie behavioral dysfunction. A prolonged Schaffer-evoked IPSP in Nex-cKO mice could impair oscillations across multiple frequency bands *in vivo* and have profound effects on neuronal firing patterns and synaptic plasticity, both of which could contribute to deficits in learning and memory.

Our findings emphasize the value of circuit profiling, particularly in models where multiple synaptic abnormalities are present. Given increasing evidence supporting the circuit specificity of neurophysiological findings in animal models (DeNardo et al., 2012; Etherton et al., 2011b; O’Hare et al., 2016; Qiu et al., 2011; Shepherd and Katz, 2011), targeted analysis of behaviorally relevant cell types and associated microcircuits are most likely to yield insight into the mechanisms responsible for pathological phenotypes. For example, a recent study found that the loss and gain of MeCP2 in mice led to convergent phenotypes of CA1 pyramidal neuron hypersynchrony (Lu et al., 2016). In addition, chronic forniceal deep-brain stimulation (DBS) can rescue both impaired learning and memory and underlying circuit dysfunction across these multiple models of Rett syndrome (Hao et al., 2015; Lu et al., 2016), illustrating the potential of neural circuit studies to reveal avenues of therapy in disorders with diverse molecular etiologies. Our findings that CDKL5 plays an essential role in excitatory neurons to regulate

hippocampal-dependent memory and circuit function suggest that in addition to therapies that seek to correct the underlying signaling changes, the modulation of circuit activity may also serve as a therapeutic target to ameliorate CDD-associated learning and memory deficits.

Materials and Methods

Generation of *Cdkl5* conditional knockout mice. An identical targeting construct and strategy was used from the generation of *Cdkl5* constitutive knockout mice (Wang et al., 2012). The targeting construct was confirmed by sequencing, linearized, and subsequently electroporated into mouse sv129 ES cells. Correctly targeted ES cell clones were independently injected into C57BL/6 blastocysts and subsequently implanted into pseudopregnant females. Chimeric offspring were backcrossed to C57BL/6, and the F₁ hybrid bred to FLP deleter mice for removal of the neomycin cassette. In tissues expressing Cre recombinase, the excision of exon 6 results in the same genetic lesion as the previously generated *Cdkl5* constitutive knockout line, causing a reading frame shift and a TAA stop codon in the 5' end of exon 7, resulting in the truncation of CDKL5 at the N-terminal kinase domain. The *Cdkl5* floxed mouse line is available at Jackson Laboratory (Stock No. 030523).

Animal husbandry. Experiments were conducted in accordance with the ethical guidelines of the National Institutes of Health and with the approval of the Institutional Animal Care and Use Committee of the University of Pennsylvania. The *Cdkl5*^{fllox} allele was generated on a congenic sv129:C57BL/6 background and backcrossed to C57BL/6

for at least 10 generations. Nex-Cre mice (Goebbels et al., 2006) (RRID: MGI: 4429523), generously shared by Professor Klaus-Armin Nave (Max Planck Institute of Experimental Medicine, Göttingen, Germany) and Professor Eros Lazzerini Denchi (The Scripps Research Institute, La Jolla, CA), were obtained on a sv129 background and also backcrossed to C57BL/6 for at least 10 generations before breeding. Mice were genotyped using a PCR-based strategy to detect the presence of the *Cdkl5* conditional knockout allele containing a *loxP*-flanked exon 6. The genotyping primers (5'-CCACCCTCTCAGTAAGGCAGCAG-3' and 5'-GTCCTTTTGCCACTCAATTCCATCC-3' give rise to a 653-bp product from the wild-type allele and 765-bp product from the conditional knockout allele with unexcised exon 6. For genotyping of Nex-Cre, primers and genotyping strategy were identical to that used in Goebbels et al, 2006.

Mice were group-housed in cages of three to five in a 12-h light/dark cycle with food and water provided ad libitum. Each breeding cage consisted of two homozygous female mice (genotype: *Cdkl5*^{fllox}/*Cdkl5*^{fllox}) and one male mouse (genotype: Nex-Cre/+). Male littermates (genotypes: *Cdkl5*^{fllox}/y;+/+ and *Cdkl5*^{fllox}/y;Nex-Cre) were weaned at 3 weeks of age and housed together, with all experiments performed on age-matched adult mice between 9 and 12 weeks of age.

For spine imaging, homozygous female mice (genotype: *Cdkl5*^{fllox}/*Cdkl5*^{fllox}) were bred to male mice carrying an allele expressing Thy1-GFP (line M) (RRID: IMSR_JAX:007788). Male littermates (genotypes: *Cdkl5*^{fllox}/y;+/+;Thy1-GFPm/+ and *Cdkl5*^{fllox}/y;Nex-Cre;Thy1-GFPm/+) were weaned at 3 weeks of age and housed together, with all experiments performed on age-matched adult mice between 9 and 12 weeks of age.

Western blot. Adult male mice (genotypes: *Cdkl5^{fllox/y};+/+* and *Cdkl5^{fllox/y};Nex-Cre*) were sacrificed by cervical dislocation. After decapitation, brains were removed and sectioned into 1 mm coronal slices using a mouse brain matrix. Tissue was dissected from the somatosensory cortex, striatum, hippocampus, and cerebellum and homogenized in lysis buffer containing 1% NP-40, pH 8.0. Protein concentration was measured using the Bradford assay and a total of 20 µg protein was loaded for each lane.

Primary antibodies used in this study are anti-N-terminal CDKL5 (generated in Wang et al, 2012; diluted 1:500), anti-GAPDH (MA5-15738, Invitrogen; RRID: AB_10977387 ;diluted 1:1000), and anti-β actin (AB8226, Abcam; RRID: AB_306371; diluted 1:1000). Secondary antibodies (Licor) are goat anti-rabbit IRDye 800CW (RRID: AB_10796098) and donkey anti-rabbit IRDye 680RD (RRID: AB_10954442) at dilutions of 1:10,000. Standard protocols were used for the Odyssey Infrared Imaging System for visualization and quantification.

Behavioral assays. All animal behavioral studies were carried out blinded to genotype. Mice were allowed to habituate to the testing room for at least 1 hour before the test, and testing was performed at the same time of day. All animal behaviors were performed on adult male mice at 9-12 weeks of age, and the analysis of behavioral data was carried out by a researcher blinded to genotype.

Elevated zero maze. The elevated zero maze (Stoelting, Illinois, USA) consists of a circular-shaped platform elevated above the floor. Two opposite quadrants of the maze are enclosed (wall height, 12 inches), whereas the other two are open (wall height, 0.5 inches). Mice were placed in one of the closed quadrants and their movement traced

over the course of 5 min. Analysis, including the quantification of percent of time spent in open arms and the number of entries, was performed manually using a stopwatch. An entry was defined as a transition from a closed to open arm, or vice versa, that involves all four paws.

Three-chambered social approach assay. The social approach assay was performed as previously described (Fairless et al., 2013; Sankoorikal et al., 2006). The social choice test was carried out in a three-chambered apparatus that consisted of a center chamber and two end chambers. Before the start of the test and in a counter-balanced sequence, one end chamber was designated the “social chamber,” into which a stimulus mouse would be introduced, and the other end chamber was designed the “nonsocial chamber.” Two identical clear, Plexiglas cylinders with multiple holes to allow for air exchange were placed in each end chamber. In the habituation phase of the test, the test mouse was placed in the center chamber and allowed to explore all three chambers for 10 min. During this acclimation period, baseline measurements of how much time the mouse spent in each of the three chambers and the distance traveled by the test mouse were collected.

In the social choice phase of the test, a stimulus mouse (adult gonadectomized A/J mice; The Jackson Laboratory) was placed in the cylinder in the social chamber while a novel object was simultaneously placed into the other cylinder in the non-social chamber. During the 5-min social choice period, chamber times and numbers of transitions among chambers were again recorded.

In the direct social interaction test, the cylinders were removed simultaneously following the social choice test, and the amount of time test and stimulus mice spent in

direct contact (sniffing, allogrooming) was measured. If fighting persisted for more than several seconds, the mice were removed from the apparatus and excluded from the study.

Y-maze. Spontaneous alternation behavior was measured on a Y-maze apparatus (San Diego Instruments, California, USA), composed of three arms (Arm A: 8"x5"x3"; Arms B and C: 6"x5"x3"). For habituation, the test mouse was placed in each of the three arms, facing the center, and allowed to make one choice to enter another arm. For testing, the mouse was placed in Arm C, facing the center, and allowed to freely explore the maze for 5 min. A spontaneous alternation was defined an entry into the arm less recently explored. Percent spontaneous alternation was calculated as the number of spontaneous alternations over the total number of entries. For example, the sequence C,B,A,B,C,B,A,C (starting in arm C) resulted in a percent spontaneous alternation of $4/6 = 67\%$.

Barnes maze. Hippocampal-dependent memory was assessed on a Barnes Maze apparatus (San Diego Instruments, California, USA), a circular platform with 36" diameter and 20 equally spaced escape holes along the perimeter, one of which leads to a "target" escape box. Bright lighting was used as stimulus to complete the task. The assay consisted of five phases: adaptation, forward acquisition training, forward probe trials, reversal training, and reversal probe trials. For adaptation, each mouse was placed in a dark start chamber in the middle of the maze for 10 s, then uncovered and guided gently to the escape box. Forward acquisition training consisted of 2 trials per day for 4 days, with each mouse starting in the dark start chamber in the middle of the maze and subsequently allowed to explore the maze for 3 minutes. The trial ends when the mouse enters the target escape hole or after 3 min have elapsed, after which the

mouse is guided gently to the escape hole. After reaching the escape hole, the mouse is allowed to remain there for 1 min. Forward probe trials were conducted on day 5, 24 hr after the last training day. During the probe trial, the maze is in the same position as the training days, and the target hole is closed. Each trial lasted 90 s, during which the number of errors (pokes into non-target holes) made prior to reaching the target hole is quantified. Days 6-10 consisted of reversal training, conducted using a similar protocol as forward acquisition training, except that the target was a stable escape hole moved 180° from its location during forward acquisition training. Reversal probe trials were conducted on day 11 and identically to forward probe trials. In addition to quantifying the number of total errors, the number of perseverations, defined as pokes into the previous target hole during forward acquisition training, was counted.

Locomotor assay. Locomotor activity was measured by beam breaks in a photobeam frame (Med Associates, Vermont, USA). Mice were individually placed into a clean home cage-like environment lined with bedding and resting within a photobeam frame. The number of beam breaks as a measure of locomotor activity was quantified over 30 min in 5-min bins.

Accelerating Rotarod assay. Mice were placed on an accelerating Rotarod apparatus (Med Associates) for 25 trials (5 trials a day on 5 consecutive days) with at least 15 min of rest between the trials. Each trial lasted for a maximum of 5 min, during which the rod accelerated linearly from 3.5 to 35 rpm. The amount of time for each mouse to fall from the rod was recorded for each trial.

Olfaction. Mice were tested for whether they could detect and differentiate odors in a habituation-dishabituation protocol modified from Yang and Crawley. Mice were

presented with cotton-tipped wooden applicators dipped in water, vanilla, or swiped across the bottom of an unfamiliar social cage. Each stimulus was presented for 2 min with a 1-min inter-trial interval. Time spent sniffing was defined as when the animal was oriented with its nose 2 cm or closer toward the cotton tip.

Repetitive behavior. Mice were individually placed into a clean home cage-like environment lined with bedding. After allowing 5 min for habituation, 10 min of activity was videotaped for each mouse. The duration of repetitive behavior, defined as grooming or digging, was scored manually using a stopwatch.

Nesting. Nesting behavior was scored as previously described (Deacon, 2006). Four- to five-week old mice were assessed for amount of cotton material used after 20 h and for the height and shape of the nest.

Hind limb clasping. Mice were suspended by the base of their tail at least 6 inches above a flat surface for up to 2 minutes. If a period of sustained clasping (at least 2 s) of the hind limbs or all four limbs were observed, the mouse was scored as a positive for the hind limb clasping phenotype.

Dendritic branching and dendritic spine analysis. All steps of sectioning, imaging, and data analysis were performed by a researcher blinded to genotype. Adult male mice 9 weeks of age (genotypes: *Cdk15^{fllox}/y*;+/+;Thy1-GFPm/+ and *Cdk15^{fllox}/y*;Nex-Cre;Thy1-GFPm/+) were transcardially perfused with 4% paraformaldehyde. Brains were extracted and post-fixed additionally for 1 hr. For dendritic branching analysis, brains were embedded in 2% agar and sectioned coronally at 200 μ m on a Leica VT1000S vibratome. For dendritic spine analysis, brains were cryoprotected by sinking in 30% sucrose in PBS, frozen in OCT (Sakura Finetek, California, USA). Frozen brains were

sectioned coronally at 50 μm on a Leica CM3050S cryostat. For both dendrite and spine imaging, unstained sections were mounted with CFMR2 (Citifluor, London, UK).

GFP-positive pyramidal neurons located in the hippocampal CA1 region (approximately between Bregma coordinates -1.34 to -1.94) with well-preserved morphology were chosen for imaging. For dendritic branching, confocal image stacks were taken on a laser scanning confocal microscope (Leica TCS SP8, 488 laser) with a 20X/0.75NA immersion objective at 1X zoom. Each neuron was oriented diagonally and centered in a field of view with dimensions 553.57 μm x 553.57 μm , with a step size of 0.5 μm . For dendritic spines, secondary and tertiary dendritic branches of basal and proximal apical dendrites, excluding the apical tuft, of CA1 pyramidal neurons were imaged. Image stacks were taken with a 63x/1.40NA oil immersion objective at 4X zoom. Each dendritic segment was centered in a field of view with dimensions 43.93 μm x 10.95 μm , with a step size of 0.22 μm and total depth spanning a depth of less than 7 μm .

All image analysis was performed by a researcher blinded to genotype. For dendritic branching analysis, the dendrites of each neuron was traced in a supervised manner using Imaris FilamentTracer (Bitplane, Massachusetts, USA) (RRID: SCR_007366). Each branch was individually traced using a combination of the Autopath and Autodepth functions, with the center of the soma designated as the dendrite beginning point. The basal and apical dendritic trees were separately traced. Sholl analysis was automatically performed by Imaris, and the statistics were exported for analysis.

For spine analysis, 3-dimensional blind deconvolution was first performed on confocal image stacks with an iterative constrained Tikhonov-Miller algorithm (DeconvolutionLab, ImageJ) using a point-spread function generated from the imaging parameters (PSF Generator, ImageJ). The deconvolved image stack was imported into Imaris and analyzed. The dendritic backbone of each segment was first traced using the Autopath function and a cone-type dendrite diameter was built using a contrast threshold of 0.2 and dendrite maximum diameter of 1 μm . A sample spine was drawn from the dendritic backbone using the Autopath function. Subsequently, seed points for spine heads with a maximum distance of 3 μm from the dendritic backbone, with the manual addition of seed points for any longer spines and curation of obvious false-positives and false-negative detections. Imaris performed automated computation of spine density and estimation of morphometric parameters for individual spines, including spine length, terminal diameter, and volume.

Ex vivo slice preparation. All steps of electrophysiological experiments, including data collection and analysis, were performed by a researcher blinded to genotype. Acute hippocampal slices were prepared from mice 9 to 12 weeks of age. Animals were anesthetized with isoflurane and transcardially perfused with ice-cold oxygenated (95% O_2 , 5% CO_2) cutting artificial cerebrospinal fluid (aCSF) solution (comprised of (mM): 2.5 KCl, 1.25 NaH_2PO_4 , 5 MgSO_4 , 0.5 CaCl_2 , 200 sucrose, 25 NaHCO_3 , 25 glucose, ~ 300 mOsm, 7.2-7.4 pH). After decapitation, brains were removed for sectioning in the same ice-cold cutting aCSF using a Vibratome (Leica Microsystems 1200S). For whole-cell patch-clamp recordings of mE/IPSCs and the measurement of intrinsic membrane properties, 350- μm transverse hippocampal sections were prepared. For all voltage-sensitive dye experiments, 400- μm transverse hippocampal sections were prepared.

Slices were recovered in the same cutting aCSF solution at 32 °C for 30 min and transferred to an oxygenated room-temperature solution composed of 50% cutting aCSF and 50% regular aCSF (comprised of (mM): 125 NaCl, 2.5 KCl, 1.25 NaH₂PO₄, 10 glucose, 26 NaHCO₃, 2 CaCl₂, 1 MgCl₂, ~300 mOsm, 7.2-7.4 pH) for 30 min. Subsequently, slices were transferred to 100% regular aCSF at room temperature for an additional 30 min before recording. All recordings were performed at 34 °C.

Intrinsic membrane properties. A pipette internal solution comprised of (mM): 130 K-gluconate, 6.3 KCl, 1 MgCl₂, 0.5 EGTA, 10 HEPES, 4 MgATP, 0.3 NaGTP, 280-290 mOsm) was used. Input resistance was measured using 10 mV test pulses, in the absence of any resistance compensation. An input-output curve was generated in current-clamp mode using 300-ms constant-current steps of increasing intensity (0-120 μA at 20-μA intervals) and counting the number of action potentials during the time window. Spike threshold (action potential threshold) was determined in current-clamp mode using depolarizing current steps in 10 pA increments until single action potentials were elicited, and the threshold voltage was determined as the membrane potential at the beginning of the sharp upward rise of the depolarizing phase of the action potential.

mEPSCs. A pipette internal solution comprised of (mM): 140 KCH₃OSO₃, 5 KCl, 0.5 EGTA, 1 MgCl₂, 10 HEPES, 5 MgATP, 0.25 NaGTP, ~292 mOsm, E_{Cl} = -78.8 mV was used. Pipettes 4-6 MΩ in resistance were pulled from borosilicate glass capillaries (World Precision Instruments, 1B150F-4) on a Sutter Instruments P-1000 pipette puller. Voltage-clamp traces 5 min in duration were recorded at a holding potential of -70 mV in the presence of 1 μM tetrodotoxin (Tocris). All recordings were conducted with access resistance of less than 20 MΩ, leak current of less than 100 pA, and an applied series resistance compensation of 80%. Cells that did not maintain these parameters for the

duration of the recording were eliminated. Analysis of mEPSCs was performed using pCLAMP10 (Axon Instruments, Molecular Devices) using a variable-amplitude template method, generated from a stable recording of at least 50 mEPSC events. Each trace was first low-pass filtered at 1 kHz, and negative-going mEPSCs were detected using a template match threshold of 4, without fitting.

mIPSCs. In order to record mIPSCs while maintaining a hyperpolarized membrane voltage, a high-chloride pipette internal solution (comprised of (mM): 100 CsCH₃O₃S, 50 CsCl, 10 HEPES, 0.2 BAPTA, 3 KCl, 1 MgCl₂, 0.25 GTP-Tris, 2.5 creatine phosphate disodium, 2 MgATP, ~296 mOsm, E_{Cl} = -23.7 mV) was used. Pipettes 4-6 MΩ in resistance were pulled from borosilicate glass capillaries (World Precision Instruments, 1B150F-4) on a Sutter Instruments P-1000 pipette puller. Voltage-clamp traces 3 min in duration were recorded at a holding potential of -70 mV in the presence of 1 μM tetrodotoxin (Tocris) and 2 mM kynurenic acid (Sigma Aldrich). All recordings were conducted with access resistance of less than 20 MΩ, leak current of less than 100 pA, and an applied series resistance compensation of 80%. Cells that did not maintain these parameters for the duration of the recording were eliminated. Analysis of mIPSCs was performed using pCLAMP10 (Axon Instruments, Molecular Devices) using a variable-amplitude template method, generated from a stable recording of at least 50 mIPSC events. Each trace was first low-pass filtered at 1 kHz, and negative-going mIPSCs were detected using a template match threshold of 4, without fitting.

Evoked AMPA/NMDA currents. A pipette internal solution (comprised of (mM): 125 CsCH₃O₃S, 4 NaCl, 1 EGTA, 10 HEPES, 4 MgATP, 0.3 NaGTP, 10 creatine phosphate disodium, 0.1 spermine tetrahydrochloride) was used. A concentric bipolar tungsten microelectrode was used for stimulation of the Schaffer collaterals. To normalize the

stimulus intensity for evoked currents, the minimal stimulus to achieve a threshold evoked response was first determined. Subsequently, a stimulus twice the intensity of the minimal stimulus was used to elicit evoked currents. Voltage-clamp traces were recorded at a holding potential of -70 mV (for AMPA-EPSCs) or +40 mV (for NMDA-EPSCs) in the presence of 50 μ M picrotoxin (Tocris). For each cell, at least 10 trials were averaged to obtain a representative response at each holding potential. The peak EPSC amplitude at -70 mV was taken as the magnitude of the AMPA-EPSCs. To estimate the NMDA-dependent contribution to the EPSC at +40 mV, the EPSC amplitude at 75 ms post-stimulus was used. Control experiments using the selective NMDA antagonist D-AP5 confirmed that at 75 ms, the AMPA-dependent contribution to the EPSC at +40 mV is very small compared to the NMDA-dependent contribution. To calculate the NMDA/AMPA ratio, the magnitude of the NMDA-dependent component at +40 mV was divided by the peak amplitude of the AMPA-EPSC at -70 mV.

Extracellular field recordings. Pipettes 2-4 M Ω in resistance were pulled from borosilicate glass capillaries (World Precision Instruments, 1B150F-4) on a Sutter Instruments P-1000 pipette puller and filled with regular aCSF. Recordings were conducted in the stratum radiatum of CA1, 400-500 μ m from the site of stimulation. For stimulation of the Schaffer collateral pathway, a concentric bipolar stimulation electrode (World Precision Instruments) was placed in stratum radiatum at the CA3-CA1 junction. The half-maximal stimulus intensity was determined for each slice by generating a standardized curve using stimuli of increasing intensity (0-200 μ A) and approximating the minimum intensity that elicited the half-maximal fEPSP amplitude. The peak amplitude of the presynaptic fiber volley preceding the field EPSP, measured from

baseline, was used as an approximation of the number of fibers recruited by a given stimulus.

Paired-pulse ratios. Two successive stimuli with a 60-ms interval were applied at the approximate half-maximal stimulus intensity. An average trace from five trials was generated for each slice. The paired-pulse ratio was calculated as the amplitude of the second EPSP divided by the amplitude of the first EPSP.

Voltage-sensitive dye imaging. Following recovery, each slice was bulk-loaded with 100 μ L of a solution containing the voltage-sensitive dye di-2-ANEPEQ (Antić and Zecević, 1995; Habib-E-Rasul Mullah et al., 2013) (JPW1114, Molecular Probes) diluted at 0.05 mg/mL in aCSF. Each slice was stained for 14 min, washed with aCSF, and imaged in an interface chamber using an 80x80 CCD camera recording with a 1 kHz frame rate (NeuroCCD; RedShirt Imaging). Illumination was provided by a 530 nm Green LED (Thor Labs, M530L3-C2). A filter set (Chroma Technologies 11007v2 wide Green) was used to allow excitation at 510-560 nm and collection of emitted fluorescence at a wavelength >592 nm. Trials lasted 1000 ms each, with a 20 s inter-trial interval. Interleaved trials without stimulation allowed for background subtraction.

All data analysis was performed in IGOR (Wavemetrics) on the average of 12 trials. Data were displayed as the change in fluorescence divided by the resting fluorescence ($\Delta F/F$). Regions of interest (ROIs) were drawn proximal (0-270 μ m) and distal (270-540 μ m) to the site of stimulation, with the following approximate dimensions (in pixels): 30x30 for stratum radiatum and 15x30 for stratum pyramidale/oriens. Like other dyes of the ANEPP family, di-2-ANEPEQ decreases in fluorescence upon membrane depolarization. To be consistent with electrophysiological conventions,

depolarizing $\Delta F/F$ signals were displayed as upward signals (warmer colors) and hyperpolarization $\Delta F/F$ signals were displayed as downward signals (colder colors). Snapshots of VSDI represent a 70x70 pixel trimmed window, corresponding to an approximately 635x635 μm field of view.

Statistical analyses. On the basis of previously published CDKL5 mouse models, we chose similar sample sizes for all behavioral experiments performed. For assays other than behavior, we determined approximate sample size and power from effect sizes found in related models of neurodevelopmental disorders. Importantly, the number of mice used for each experiment were pre-determined prior to the start of the experiment.

For behavioral assays, statistical analyses were performed using Prism (GraphPad). All data sets were analyzed using the D'Agostino-Pearson omnibus test for normality. Data sets with normal distributions were analyzed for significance using unpaired Student's two-tailed *t*-test. Data sets with non-normal distribution were analyzed using the Mann-Whitney test. Two-way repeated measures ANOVA was conducted for the appropriate data sets with Holm-Sidak's multiple comparison test, using adjusted $*p < 0.05$.

All other assays that involved sub-sampling of animals were analyzed using R (The R Project for Statistical Computing). Each data set was analyzed using a "linear mixed effect model," where *Genotype* was modeled as a fixed effect term and *Animal* was modeled as a random effect term. This model accounts for both between-animal and between-cell variation. For each assay, null and alternative models were constructed using the *lmer* function in the lme4 package (Bates et al., 2015) in the following format:

```
m0 = lmer(Outcome ~ (1 | Animal), REML=TRUE)
```

```
m1 = lmer(Outcome ~ Genotype + (1 | Animal), REML=TRUE)
```

For data sets involving a third term (e.g. time), the following null and alternative models were constructed, in order to test the significance of an interaction between Genotype and the third term:

```
m0 = lmer(Outcome ~ Time + Genotype + (1 | Animal), REML=TRUE)
```

```
m1 = lmer(Outcome ~ Time*Genotype + (1 | Animal), REML=TRUE)
```

To make statistical comparisons, the *KRmodcomp* function from the *pbkrtest* package (Halekoh and Højsgaard, 2014) was used:

```
KRmodcomp(m0, m1)
```

The *KRmodcomp* function reports a modified F-test statistic based on the Kenward and Roger approximation (Kenward and Roger, 1997), which accounts for the small sample sizes in our study, modified numerator and denominator degrees of freedom, and a p-value. The estimated effect of Genotype is obtained from the alternative model constructed using the *lmer* function from *lme4*.

For post-hoc comparisons of VSDI time point data, we used the *glht* function from the *multcomp* package (Hothorn et al., 2008), with the p-values adjusted for multiple comparisons using Holm's method:

```
summary(glht(m1, linfct = K %*% X), test = adjusted(type = "holm"))
```

where the argument for *linfct* is a matrix of coefficients representing the linear hypotheses to be tested. For voltage-sensitive dye imaging data, a total of six between-

Genotype comparisons were made, corresponding to six pre-selected time points post-stimulus (0/8/10/20/40/60 ms). For each test, the z score and adjusted p-value are reported.

For the analysis of cumulative distributions (mEPSC and mIPSC inter-event intervals and amplitudes), all samples from each individual cell was sorted, binned, and averaged at percent intervals, effectively generating a binned cumulative distribution curve for each cell. Data from all cells of a given genotype were plotted at these distinct binned percent intervals with the mean and error bars indicating s.e.m. The results were analyzed using linear mixed effect models, incorporating a third term, “cumulative frequency bin.” In two experiments (mEPSCs, AMPA/NMDA-EPSCs), Grubbs’ test for outliers was applied with a threshold of $p < 0.01$ on both wild type and mutant data sets, with the excluded value noted in the figure legends.

All graphs are plotted using Prism (GraphPad). In our figures, p-values between 0.05 and 0.1 are shown explicitly, and the symbol * is used to denote all p-values less than 0.05.

Figures

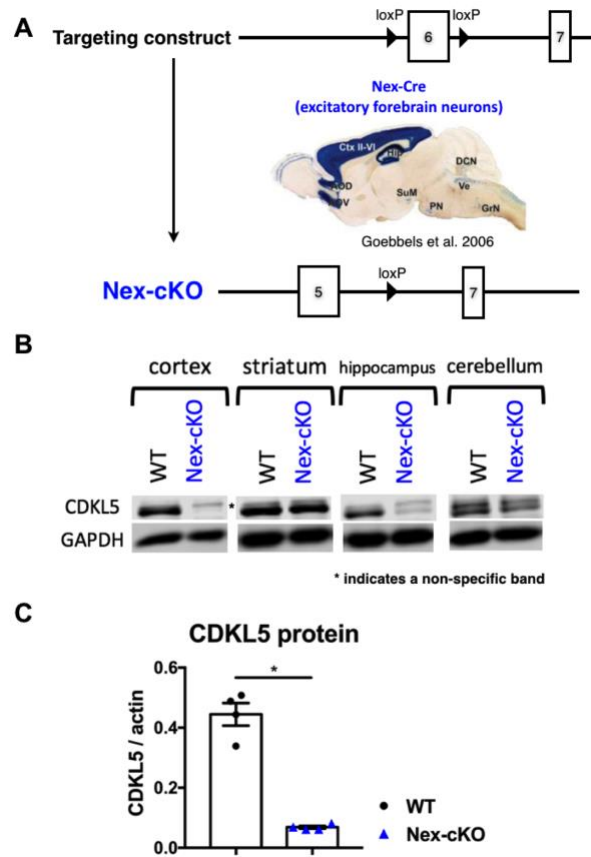


Figure 1. Generation of Nex-cKO mice and validation of conditional knockout strategy.

(A) Schematic of targeting construct, expression pattern of Nex-Cre (Goebbels et al., 2006), and the Cre-dependent excision of exon 6 of a floxed *Cdkl5* allele. Nex-cKO (Nex-Cre; *Cdkl5^{fllox/y}*) male mice have a selective deletion of CDKL5 in forebrain glutamatergic neurons. (B) Because of the lack of a suitable antibody for CDKL5 immunohistochemistry, western blotting was used to validate the cell type-specificity of knockout. In the cortex and hippocampus, brain regions enriched in glutamatergic neurons, CDKL5 levels are significantly reduced. In the striatum and cerebellum, where Nex-Cre expression is low, CDKL5 levels are not grossly altered. GAPDH was used as loading control in this panel. (C) CDKL5 protein levels are reduced by about 85% in whole hippocampal lysates of Nex-cKO mice. β -actin was used as loading control in this panel. Mann-Whitney test, n=4 mice for WT, n=4 mice for Nex-cKO. Data are mean \pm s.e.m., *p<0.05.

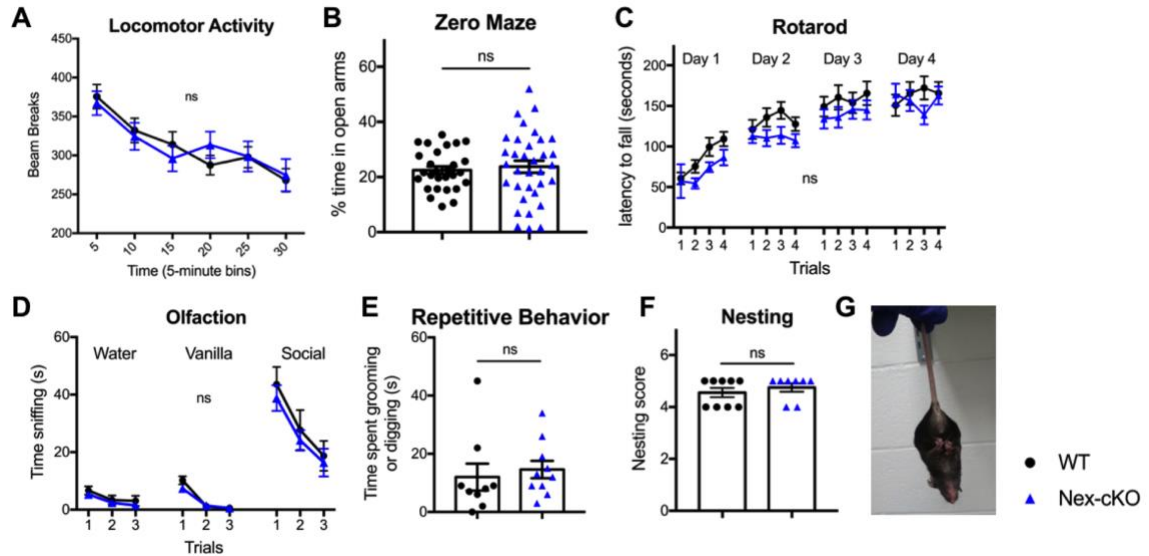


Figure 2. Assessment of home-cage locomotion, anxiety-related behavior, motor coordination, olfaction, repetitive behavior, nesting, and hind limb claspings in Nex-cKO mice.

(A) Nex-cKO mice exhibit unaltered locomotor activity during a 30-minute exploration of a home cage-like environment. (Two-way RM ANOVA, $n=13$ mice for WT, $n=25$ mice for Nex-cKO). (B) In the elevated zero maze, Nex-cKO and WT mice spend similar times in open arms, demonstrating unaltered anxiety-related behavior. (unpaired t-test, $n=28$ mice for WT, $n=34$ mice for Nex-cKO). (C) In the Rotarod assay, Nex-cKO and WT mice exhibit similar latencies to fall and improvement over multiple trials, demonstrating unaltered motor coordination and learning. (Two-way RM ANOVA, $n=27$ mice for WT, $n=30$ mice for Nex-cKO). (D) In the olfactory habituation-dishabituation test, Nex-cKO and WT mice spend similar times sniffing various odors, demonstrating an intact preference for social over non-social scents. Nex-cKO and WT mice also demonstrate similar levels of habituation after repeated exposures to the same scent. (Two-way RM ANOVA, $n=9$ mice for WT, $n=14$ mice for Nex-cKO). (E) Nex-cKO and WT mice exhibit similar levels of repetitive behavior (grooming or digging) in a home cage-like environment. (Mann-Whitney test, $n=9$ mice for WT, $n=10$ mice for Nex-cKO). (F) Nex-cKO and WT mice achieve similar scores in the nest building assay. (Mann-Whitney test, $n=9$ mice for WT, $n=8$ mice for Nex-cKO). (G) Image of a P120 Nex-cKO mouse suspended by the tail, exhibiting limb claspings. WT mice consistently splay their hind limbs outward in anticipation of landing. In contrast, Nex-cKO mice exhibit claspings of the hind limbs and sometimes also fore limbs. In a cohort of P120 mice, 0/11 of WT mice and 17/18 (94%) of Nex-cKO mice exhibited limb claspings. The phenotype of limb claspings begins to emerge in Nex-cKO mice at approximately P90. Data are mean \pm s.e.m.

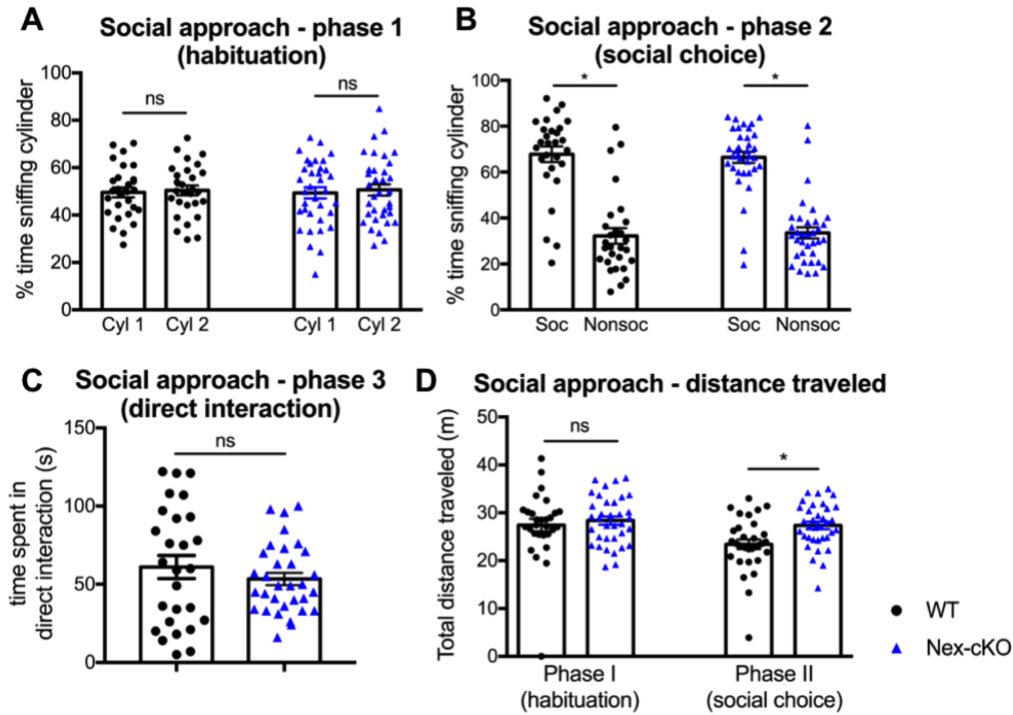


Figure 3. Unaltered sociability in Nex-cKO mice.

(A) WT and Nex-cKO mice did not exhibit a preference for either chamber during habituation (phase I) of the three-chambered social approach assay, when no stimulus mouse was present. (B) Similar to WT, Nex-cKO exhibited a strong preference for the social chamber during social choice (phase II) of the three-chambered social approach test. (C) Compared to WT, Nex-cKO mice exhibited similar levels of direct interaction with the stimulus mouse. (D) WT and Nex-cKO mice exhibit similar levels of activity during habituation, but Nex-cKO mice become hyperactive during the social choice phase. Mann-Whitney test for all experiments. WT, n=28 mice; Nex-cKO, n=35 mice. Data are mean \pm s.e.m., * $p < 0.05$.

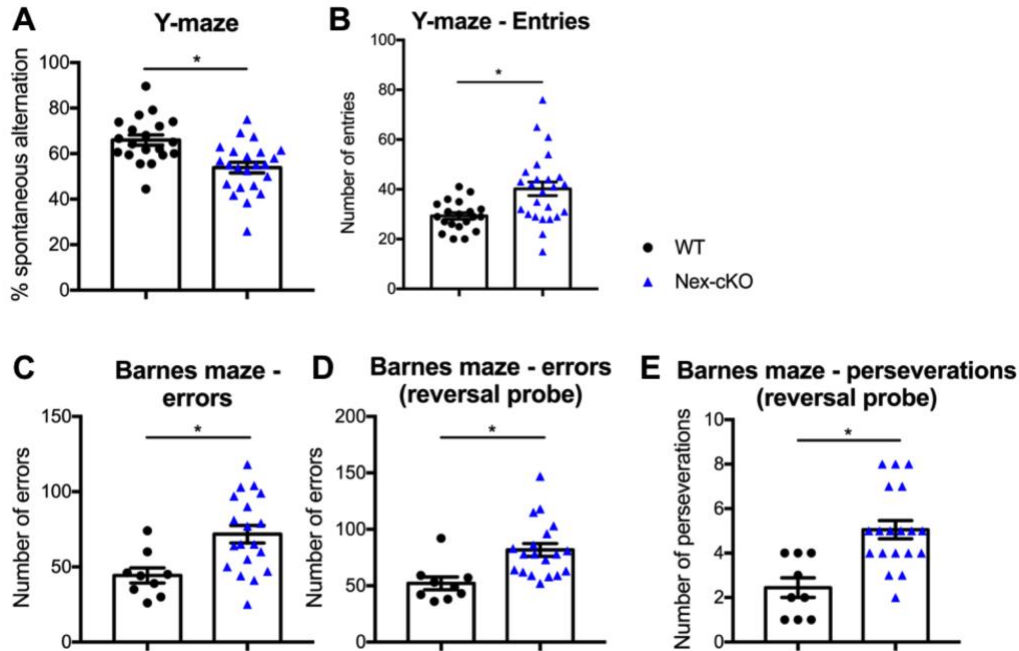


Figure 4. Impaired hippocampal-dependent learning and memory in Nex-cKO mice.

(A) Compared to wild type (WT) littermates, Nex-cKO mice showed decreased spontaneous alternation on the Y-maze assay (unpaired t-test, $n=20$ mice for WT and $n=23$ mice for Nex-cKO). (B) During the Y-maze assay, Nex-cKO mice make a greater number of total entries into arms (unpaired t-test). (C, D) During both the forward (C) and reversal (D) probe trials of the Barnes maze assay, Nex-cKO mice made more errors before reaching the target hole (forward probe: unpaired t-test; reversal probe: Mann-Whitney test; $n=9$ mice for WT and $n=19$ mice for Nex-cKO). (E) During the reversal probe trials of the Barnes maze assay, Nex-cKO mice also made more incorrect visits (perseverations) to the previous escape hole (unpaired t-test). Data are mean \pm s.e.m., $*p<0.05$.

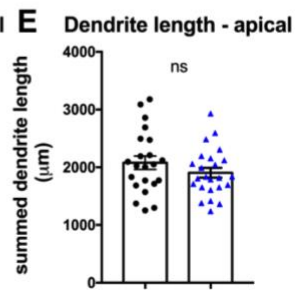
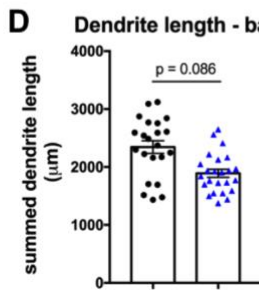
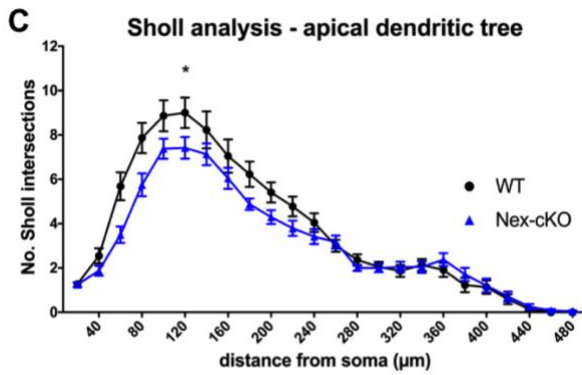
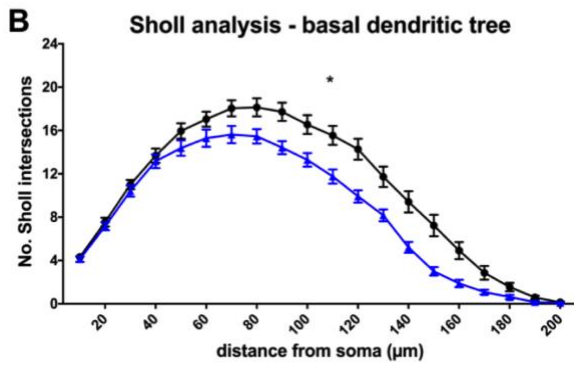
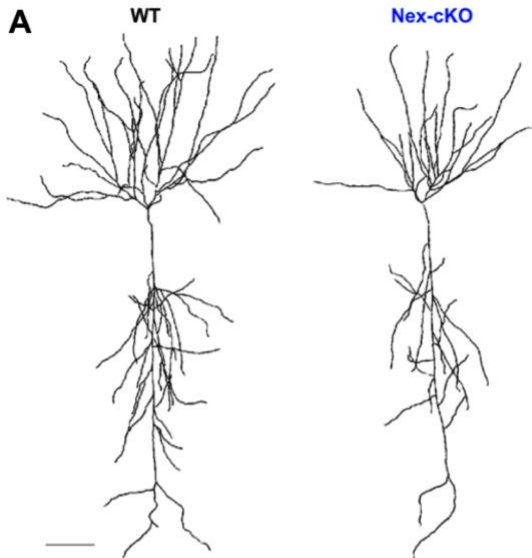


Figure 5. Decreased dendritic complexity in CA1 pyramidal neurons of Nex-cKO mice.

(A) Representative tracings of neurons from WT and Nex-cKO mice. Scale bar indicates 50 μm . (B) Decreased branching of the basal dendritic tree in Nex-cKO mice. (C) Decreased branching of proximal apical dendrites in Nex-cKO mice. (B-C) Linear mixed effect model analysis, interaction of genotype and distance from soma, random effect of animal. (D) A trend toward decreased total basal dendritic length in Nex-cKO mice. (E) Similar total apical dendritic length between WT and Nex-cKO mice. (D-E) Linear mixed effect model analysis, fixed effect of genotype, random effect of animal. For all dendritic branching analysis, $n=22$ cells/3 mice for WT and $n=24$ cells/4 mice for Nex-cKO. Data are mean \pm s.e.m., $*p<0.05$.

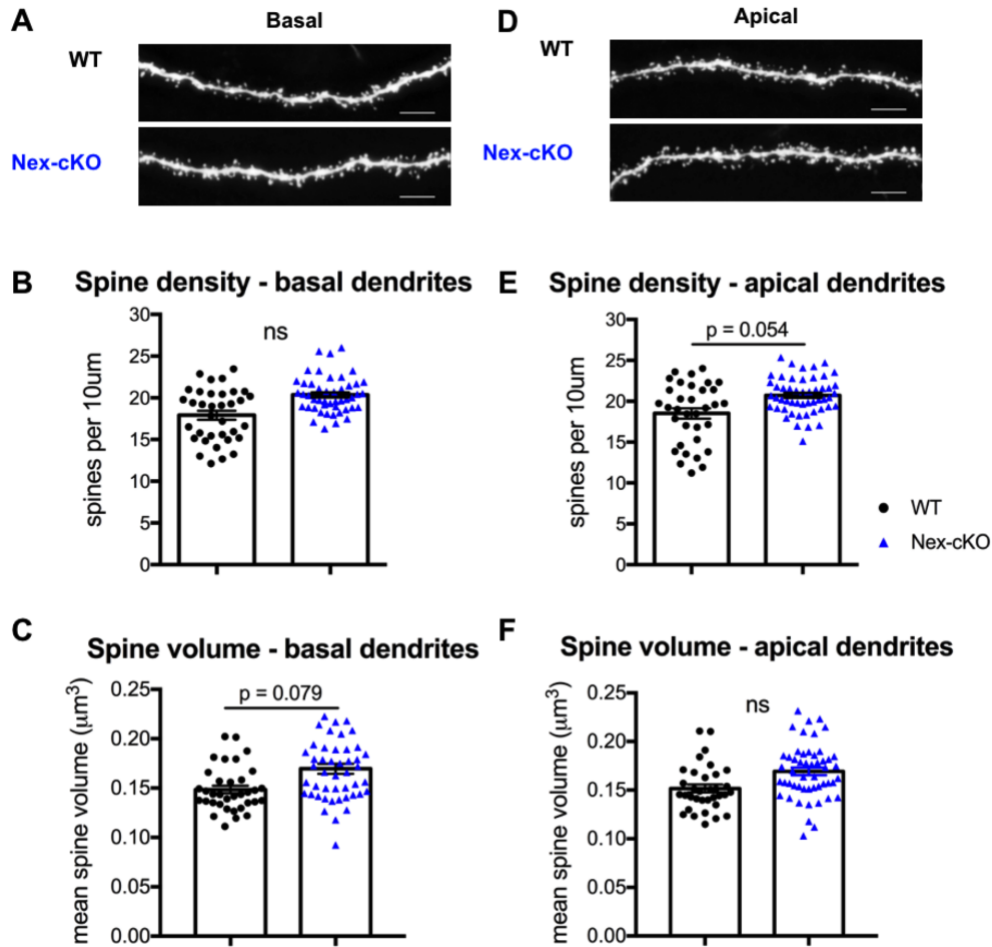


Figure 6. Analysis of spine density and morphology in CA1 pyramidal neurons of Nex-cKO mice.

(A, D) Representative segments from basal and proximal apical (excluding the apical tuft) dendrites of WT and Nex-cKO mice. Scale bar indicates 5 μm . (B) Similar spine density at basal dendrites in Nex-cKO mice. (C) A trend toward increased spine volume at basal dendrites in Nex-cKO mice. (E) A trend toward increased spine density at proximal apical dendrites in Nex-cKO mice (F) Similar spine volume at proximal apical dendrites in Nex-cKO mice. (B,C,E,F) Linear mixed effect model analysis, fixed effect of genotype, random effect of animal. For all spine analysis, one dendritic segment was imaged per cell. For basal dendritic spines, $n=35$ cells/3 mice for WT, $n=47$ cells/3 mice for Nex-cKO. For proximal apical dendritic spines, $n=34$ cells/3 mice for WT and $n=51$ cells/3 mice for Nex-cKO). Data are mean \pm s.e.m.

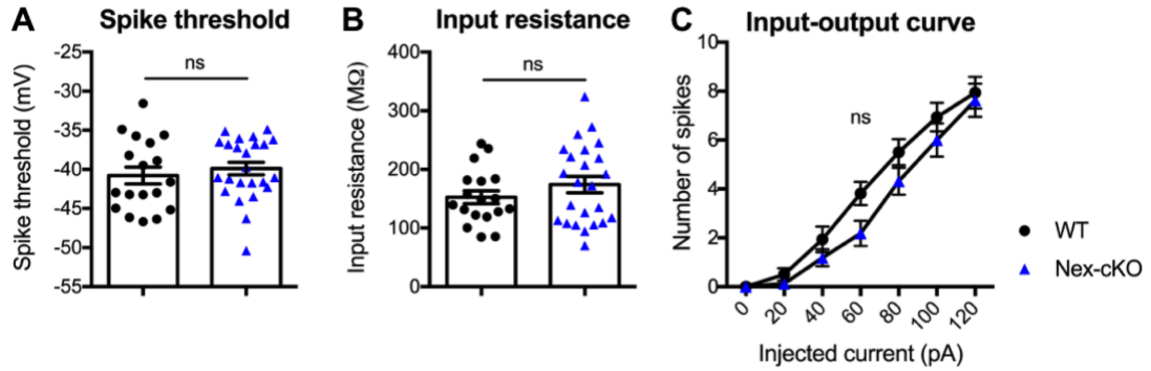


Figure 7. Unaltered intrinsic membrane properties in CA1 pyramidal neurons of Nex-cKO mice.

(A) Unaltered spike threshold in Nex-cKO mice. (B) Unaltered input resistance in Nex-cKO mice. (A-B) Linear mixed effect model analysis, fixed effect of genotype, random effect of animal. (C) Unaltered input-output curve in Nex-cKO mice. For the input-output curve, incremental 300 ms current steps were applied, and the number of spikes was counted for each current amplitude. (C) Linear mixed effect model analysis, interaction of genotype and current injected, random effect of animal. For all intrinsic membrane property experiments: n=18 cells/4 mice for WT and n=24 cells/3 mice for Nex-cKO. Data are mean \pm s.e.m.

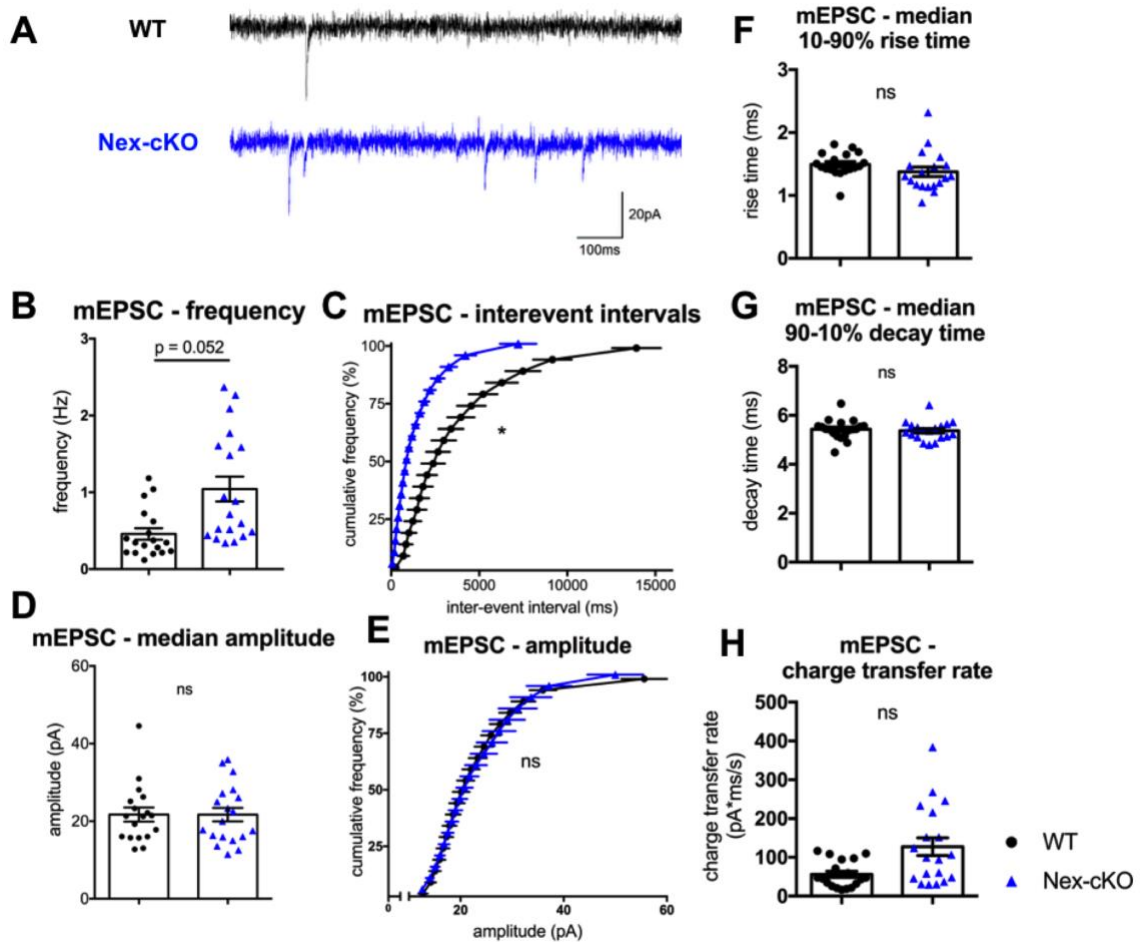


Figure 8. Increased mEPSC frequency in CA1 pyramidal neurons of Nex-cKO mice.

(A) Representative traces of mEPSCs recorded from WT and Nex-cKO mice. (B) A trend toward increased frequency of mEPSCs in Nex-cKO mice. (C) Decreased inter-event interval of mEPSCs in Nex-cKO mice. (D-E) Unaltered mEPSC amplitude in Nex-cKO. (F) Unaltered mEPSC 10-90% rise time in Nex-cKO mice. (G) Unaltered mEPSC 90-10% decay time in Nex-cKO mice. (H) Unaltered mEPSC charge transfer rate in Nex-cKO mice. (B, D, F, G, H) Linear mixed effect model analysis, fixed effect of genotype, random effect of animal. (C, E) Linear mixed effect model analysis, interaction of genotype and cumulative frequency bin, random effect of animal. For all mEPSC analysis, one data point (WT, mEPSC frequency = 3.95 Hz) was eliminated in Grubb's test for outliers ($p < 0.01$); $n = 18$ cells/3 mice for WT and $n = 19$ cells/3 mice for Nex-cKO. Data are mean \pm s.e.m. * $p < 0.05$.

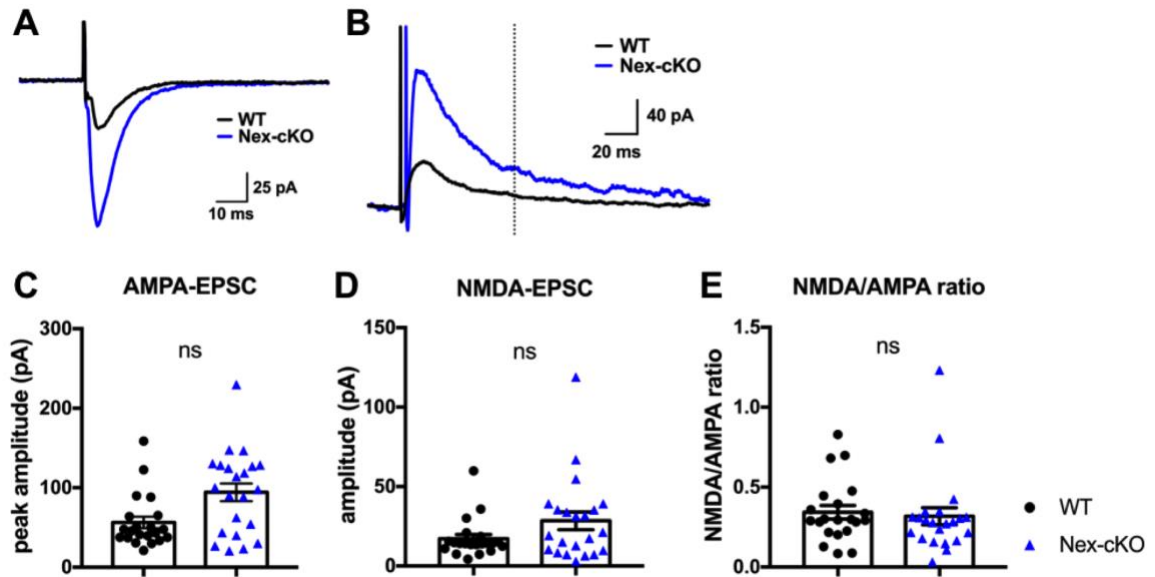


Figure 9. Unaltered AMPA/NMDA ratio in CA1 pyramidal neurons of Nex-cKO mice. (A) Representative evoked AMPA-dependent EPSCs recorded at -70 mV. (B) Representative evoked compound EPSCs recorded at +40 mV. Dotted line indicates 75 ms post-stimulus, a time point at which the AMPA-dependent contribution is considered negligible. (C) Similar amplitudes of AMPA-dependent EPSCs recorded at -70 mV. (D) Similar amplitudes of NMDA-dependent component of EPSCs. (E) Unaltered NMDA/AMPA ratio in Nex-cKO mice. (C, D, E) Linear mixed effect model analysis, fixed effect of genotype, random effect of animal. One data point (WT, AMPA-EPSC = 305.1 pA) was eliminated in Grubb's test for outliers ($p < 0.01$). $n = 21$ cells/4 mice for WT and $n = 22$ cells/4 mice for Nex-cKO. Data are mean \pm s.e.m.

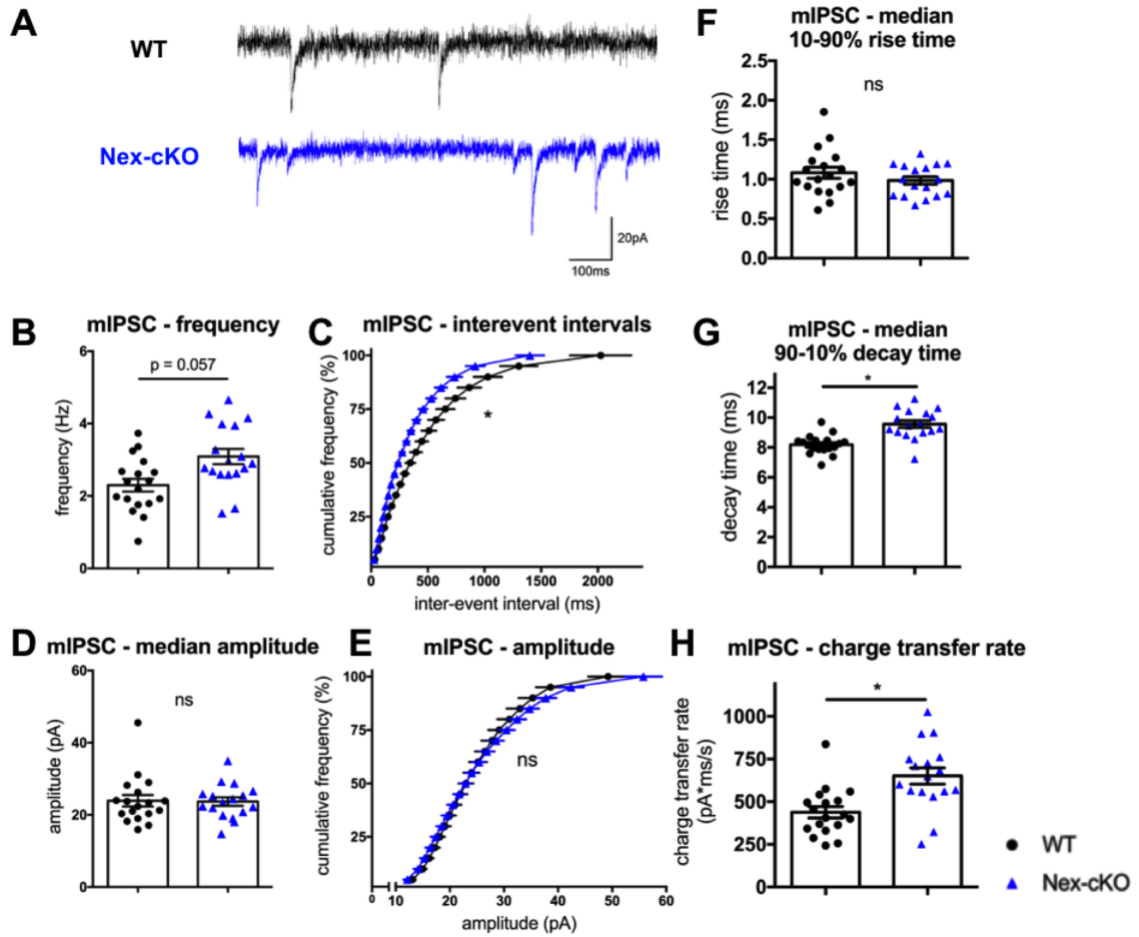


Figure 10. Increased mIPSC frequency in CA1 pyramidal neurons of Nex-cKO mice.

(A) Representative traces of mIPSCs recorded from WT and Nex-cKO mice. (B) A trend toward increased frequency of mIPSCs in Nex-cKO mice. (C) Decreased inter-event interval of mIPSCs in Nex-cKO mice. (D-E) Unaltered mIPSC amplitude in Nex-cKO mice. (F) Unaltered mIPSC 10-90% rise time in Nex-cKO mice. (G) Increased mIPSC 90-10% decay time in Nex-cKO mice. (H) Increased mIPSC charge transfer rate in Nex-cKO mice. (B, D, F, G, H) Linear mixed effect model analysis, fixed effect of genotype, random effect of animal. (C, E) Linear mixed effect model analysis, interaction of genotype and cumulative frequency bin, random effect of animal. For all mIPSC analysis, $n=18$ cells/3 mice for WT and $n=17$ cells/3 mice for Nex-cKO. Data are mean \pm s.e.m., * $p < 0.05$.

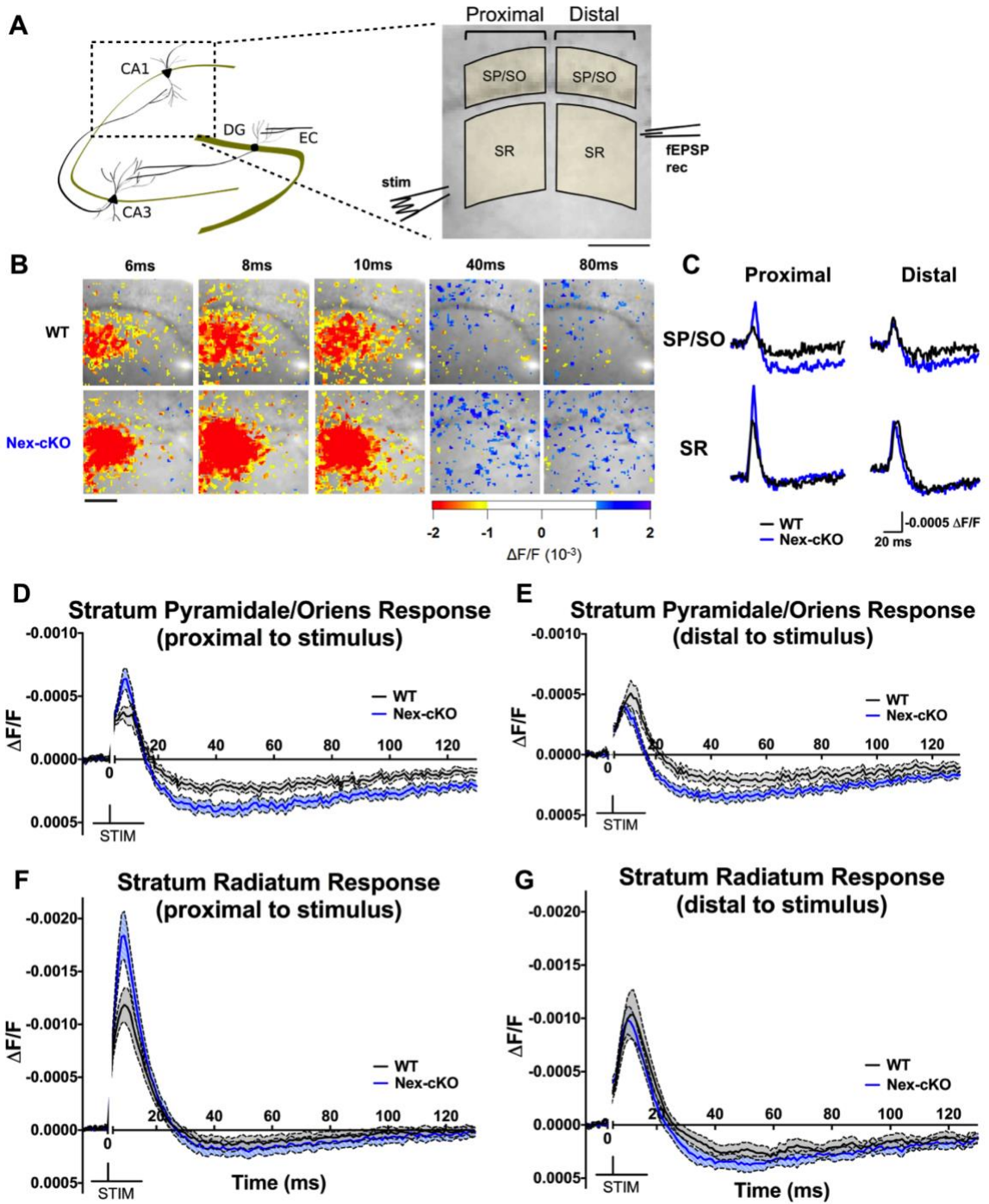


Figure 11. Disrupted spatiotemporal dynamics of the CA1 microcircuit in Nex-cKO mice

(A) Schematic of voltage-sensitive dye imaging (VSDI) showing the site of stimulation, site of field EPSP recording, and regions of interest (ROIs) used for analysis. SR: *stratum radiatum*; SP/SO: *stratum pyramidale/oriens*. Proximal and distal ROIs were drawn for SR and SP/SO to assess the spatiotemporal spread of excitation and inhibition. (B) Representative snapshots of Schaffer-evoked VSDI responses in WT and Nex-cKO mice. Depolarization is represented by warm colors while hyperpolarization is represented by cool colors. Pixels with $\Delta F/F$ changes of less than 1×10^{-3} (approximately 3x the noise level) were blanked. Scale bars in (A) and (B) indicate 200 μm . (C) Representative VSD responses in WT and Nex-cKO mice in the proximal and distal SP/SO and SR. Following current-clamp convention, depolarization (decrease in $\Delta F/F$) is displayed as an upward signal, while hyperpolarization (increase in $\Delta F/F$) is displayed as a downward signal. A stimulus artifact occurring at 1-4 ms post-stimulation was removed. (D-G) Averaged responses ($\Delta F/F$) in *stratum pyramidale/oriens* (D, E) and *stratum radiatum* (F, G) of WT and Nex-cKO slices during the 130 ms immediately following Schaffer collateral stimulation. Note that excitation is enhanced in proximal, but not distal regions, while inhibition is enhanced primarily in the SP/SO. Error envelopes represent mean \pm s.e.m. For all experiments, $n=19$ slices/7 mice for WT and $n=18$ slices/5 mice for Nex-cKO.

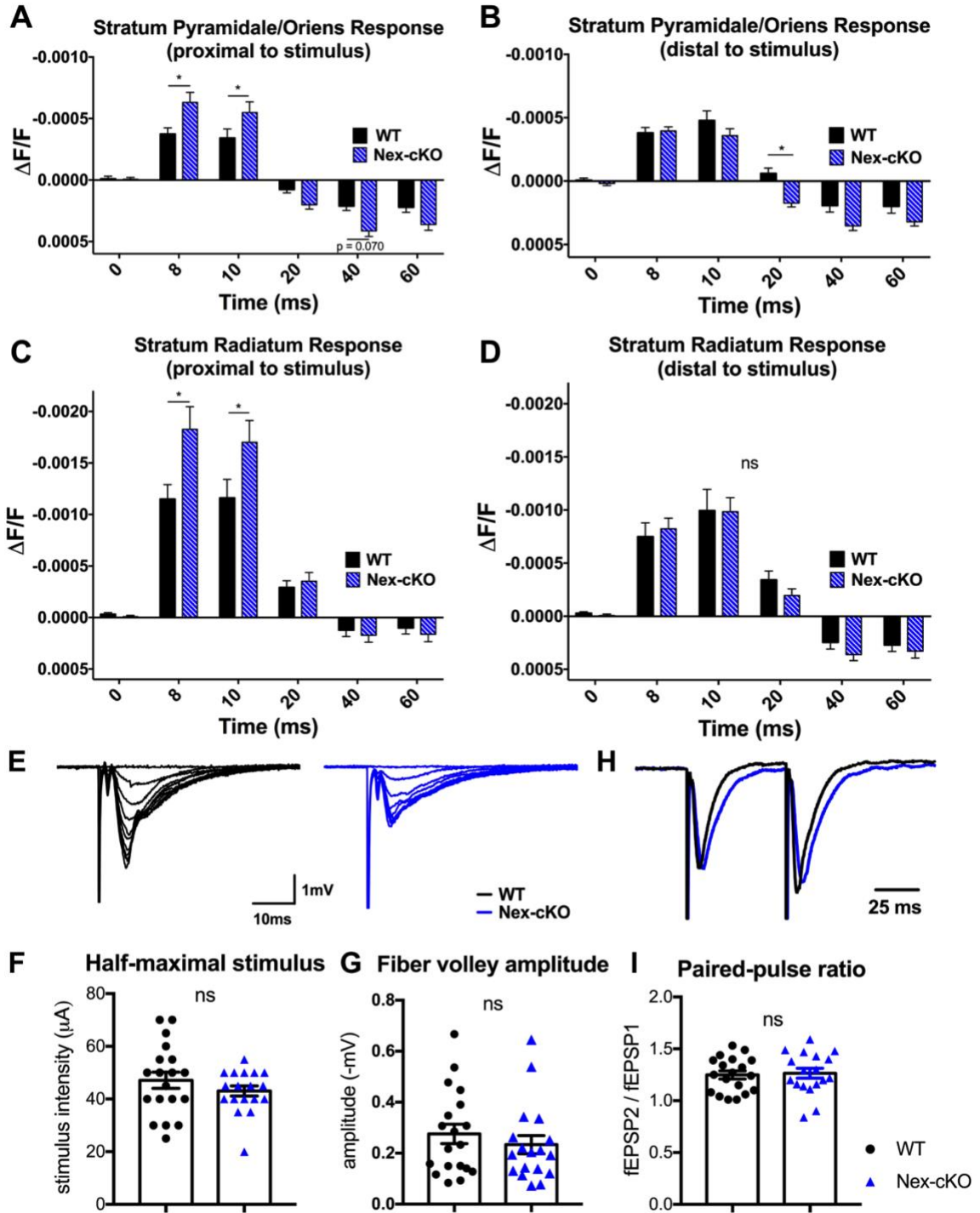


Figure 12. VSDI summary data, standardization of stimulus intensity, and paired-pulse ratio.

(A-D) Statistical comparisons of *stratum pyramidale/oriens* (A, B) and *stratum radiatum* (C, D) responses in WT and Nex-cKO mice at specific time points following stimulation. Note significantly enhanced excitation in Nex-cKO at 8-10 ms post-stimulus in proximal, but not distal, SR and SP/SO. Note significantly enhanced inhibition in Nex-cKO in the proximal and distal SP/SO at 40 ms and 20 ms post-stimulus, respectively. (A-D) Linear mixed effect model analysis, interaction of genotype and time point, random effect of animal. Generalized linear hypothesis tests were performed for individual time points with Holm's method to adjust for multiple comparisons. (E) Representative Schaffer-evoked field EPSP traces in WT and Nex-cKO mice recorded at incremental stimulus intensity from 0-200 μ a. The "half-maximal" stimulus intensity was defined as the stimulus required to elicit approximately 50% of the maximal Schaffer-evoked field EPSP amplitude in *stratum radiatum*. (F) Standardized half-maximal stimulus intensities used for voltage-sensitive dye imaging were not significantly different between WT and Nex-cKO mice. (G) Fiber volley amplitudes elicited at half-maximal stimulus intensities were not significantly different between WT and Nex-cKO mice. (H) Representative paired-pulse fEPSP responses from WT and Nex-cKO mice, elicited at half-maximal stimulus intensity using a 60 ms inter-stimulus interval. (I) Paired-pulse ratios of field EPSPs were not significantly different in WT and Nex-cKO mice. (F-I) Linear mixed effect model analysis, fixed effect of genotype, random effect of animal. For all experiments, n=19 slices/7 mice for WT and n=18 slices/5 mice for Nex-cKO. Data are mean \pm s.e.m. *p<0.05.

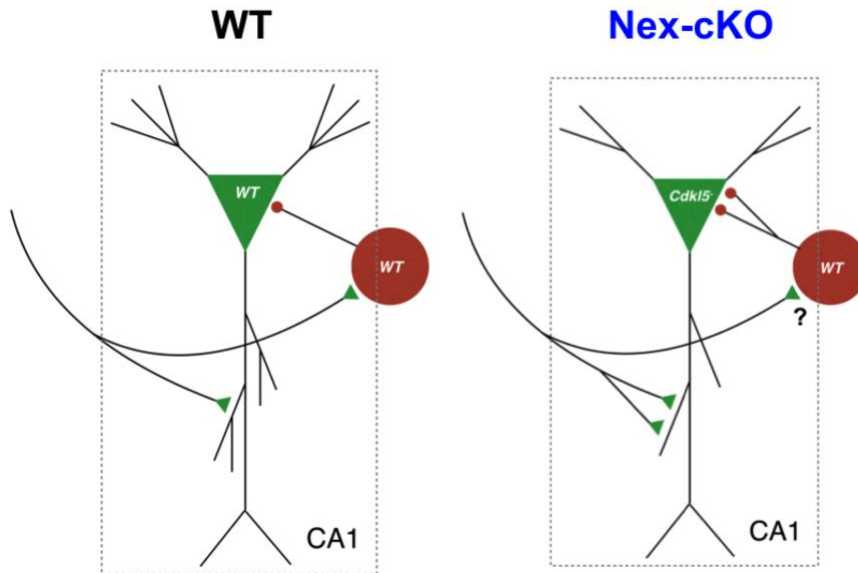


Figure 13. Model of synaptic and circuit abnormalities in Nex-cKO mice.

In WT mice, the Schaffer collateral pathway predominantly activates excitatory synapses in the proximal dendrites (*stratum radiatum*) of CA1 pyramidal neurons. Activation of local interneurons leads to inhibition primarily in the cell body layer (*stratum pyramidale*). In mice lacking CDKL5 selectively in excitatory neurons, the concomitant upregulation of excitatory and inhibitory synaptic activity leads to exaggerated synaptic responses that alter the spatiotemporal dynamics of the CA1 microcircuit.

CHAPTER 3 – GABAERGIC NEURON DYSFUNCTION AND ALTERED GLUTAMATERGIC SIGNALING UNDERLIE AUTISTIC-LIKE FEATURES IN CDKL5- DEFICIENT MICE

Contributions: Sheng Tang led this study, with help from I-Ting Judy Wang and Barbara Terzic for behavioral experiments, Cuiyong Yue and Hajime Takano for electrophysiologic experiments, and Zhaolan Zhou and Douglas Coulter for the review and interpretation of data. Yolanda Cui managed mouse colonies. Sheng Tang wrote this chapter with input from all authors.

Abstract

CDKL5 deficiency disorder (CDD) is characterized by epilepsy, intellectual disability, and autistic features. CDKL5-deficient mice exhibit a constellation of behavioral deficits reminiscent of CDD, including impaired learning and memory and social deficits. Previous studies have delineated the functions of CDKL5 in forebrain glutamatergic neurons in regulating cellular morphology, synaptic transmission, and learning and memory. However, the role of CDKL5 in GABAergic neurons remain unknown. Here, we find that selective deletion of CDKL5 in forebrain GABAergic neurons results in autistic-like features in mice. At the synaptic level, we discover a non-cell autonomous enhancement of glutamatergic transmission that leads to circuit hyperexcitability. Furthermore, acute reduction of glutamatergic transmission ameliorates autistic-like features in CDKL5-deficient mice. Together, our findings suggest that GABAergic dysfunction and network hyperexcitability underlie autistic-like features in CDKL5-deficient mice and provide a novel therapeutic avenue to treat CDD-related symptoms.

Introduction

Mutations in cyclin-dependent kinase-like 5 (*CDKL5*) cause a severe neurodevelopmental disorder characterized by seizures, intellectual disability, and autistic features (Kalscheuer et al., 2003; Tao et al., 2004; Weaving et al., 2004). Mouse models of (CDD) have recapitulated numerous aspects of the human disorder, showing behavioral deficits such as impaired learning, reduced sociability, motor dysfunction, and altered anxiety-related behavior (Amendola et al., 2014; Jhang et al., 2017; Okuda et al., 2018; Wang et al., 2012). The extent to which these behavioral deficits arise from common or distinct mechanisms, however, remain unclear.

CDKL5 protein expression is enriched in the forebrain, primarily in glutamatergic and GABAergic neurons (Johnson et al., 2017; Wang et al., 2012; Zeisel et al., 2015). In glutamatergic neurons, CDKL5 has been found at the postsynaptic density, where it interacts with PSD-95 and NGL-1 (Ricciardi et al., 2012; Zhu et al., 2013). In addition, loss of CDKL5, both *in vitro* and *in vivo*, has been associated with altered dendritic spine density and morphology, altered excitatory synaptic transmission, and altered synaptic plasticity (Okuda et al., 2017; Ricciardi et al., 2012; Sala et al., 2016; Tang et al., 2017). At the behavioral level, mice lacking CDKL5 selectively in forebrain glutamatergic neurons (Nex-cKO) show impaired learning and memory (Tang et al., 2017), reminiscent of the intellectual disability found in CDD. Surprisingly, however, Nex-cKO mice did not show other behavioral deficits found in *Cdkl5* constitutive knockout mice, including alterations in sociability, stereotypic behavior, locomotion, motor coordination, and anxiety-related behavior (Tang et al., 2017). These results demonstrated the importance of CDKL5 function in glutamatergic neurons for learning and memory, but also suggested the potential roles of CDKL5 in other neuronal populations.

Loss of CDKL5 has been associated with numerous functional changes at the synaptic and circuit levels. A recent study found that CDKL5 knockout mice showed increased susceptibility to NMDA-induced seizures and correspondingly, increased NMDA-dependent synaptic transmission and enhanced long-term potentiation at hippocampal synapses (Okuda et al., 2017). Interestingly, Nex-cKO mice do not show a selective enhancement of NMDA signaling but instead a non-specific increase in glutamatergic synaptic transmission (Tang et al., 2017). Furthermore, Nex-cKO mice show concomitant changes in synaptic inhibition that constrain hyperexcitability at the circuit level. Taken together, the differences between *Cdkl5* constitutive knockout mice and Nex-cKO mice suggest that altered glutamatergic synaptic transmission may arise from both cell autonomous and non-cell autonomous mechanisms. In addition, the extent to which altered glutamatergic signaling underlies CDD-related behavioral phenotypes remains unclear.

Here, we demonstrate that the loss of CDKL5 in forebrain GABAergic neurons (Dlx-cKO) leads to autistic-like features in mice. Surprisingly, we find that excitatory synaptic transmission is enhanced in a non-cell autonomous manner, with the relative sparing of inhibitory synaptic transmission. Dlx-cKO mice also show hyperexcitability at the circuit level, exhibiting aberrant paired-pulse facilitation at perforant path-dentate gyrus synapses. In CDKL5-deficient mice, we find that acute, low-dose NMDAR blockade selectively ameliorates autistic-like features, demonstrating that an excess of glutamatergic synaptic transmission underlies selective behavioral deficits in CDD. Our findings support a novel mechanism by which GABAergic neuron-specific loss of CDKL5 and altered glutamatergic signaling contribute to the etiology of autistic-like behaviors in a mouse model of CDD.

Results

Mice lacking CDKL5 in GABAergic neurons show autistic-like features

To investigate the role of CDKL5 in GABAergic neurons, we generated conditional knockout mice lacking CDKL5 selectively in forebrain GABAergic neurons (Dlx-cKO) using the Dlx-5/6 Cre driver (Fig. 1A, B) (Monory et al., 2006). Dlx-cKO mice showed normal growth and body weight through adulthood and no obvious physical abnormalities (Fig. 1C). We therefore performed a battery of behavioral assays, similar to those in previous studies of *Cdkl5* constitutive KO and Nex-cKO mice. Like Nex-cKO mice, Dlx-cKO showed unaltered home-cage locomotion, anxiety-related behaviors, and motor coordination (Fig. 2). We next assessed learning and memory, a behavioral domain significantly impaired in both *Cdkl5* constitutive knockout mice and Nex-cKO mice. Unlike Nex-cKO mice, Dlx-cKO showed no impairment in spontaneous alternation behavior on the Y-maze, suggesting intact working memory (Fig. 3A, B). On the Barnes maze, an assay of spatial learning and memory, Dlx-cKO did not show a significant difference from wild type controls in the number of errors made on probe trials (Fig. 3C). However, when the target hole location was altered to the opposite side of the maze (reversal probe trials) after acquisition, Dlx-cKO mice showed a significant impairment in adjusting to this new target hole (Fig. 3D). Furthermore, Dlx-cKO mice also demonstrated an increased number of perseverations on reversal probe trials, or visits to the previous target hole location (Fig. 3E). These results suggest that although Dlx-cKO mice are comparable to wild type controls in several learning and memory assays, they demonstrate signs of cognitive inflexibility, a phenotype reminiscent of autism spectrum disorders.

On the three-chamber social approach assay, Dlx-cKO mice demonstrated significantly altered social behavior, showing a lack of preference for investigating a social stimulus as compared to an object (Fig. 4A, B). When allowed the opportunity for direct interaction with a novel stimulus mouse, Dlx-cKO mice also spent significantly less time initiating contact in comparison to wild type controls (Fig. 4C). To rule out the involvement of an olfactory deficit underlying reduced social preference, we conducted the olfactory habituation-dishabituation test. Dlx-cKO mice showed intact ability to discriminate between different scents and also habituated to repeated presentation of the same scent. Interestingly, however, Dlx-cKO mice showed reduced time sniffing a social scent, consistent with a reduced interest in social stimuli (Fig. 4D).

In addition to social behaviors, we also assessed stereotypic behaviors, another feature of autism spectrum disorder. In a home-cage like environment, Dlx-cKO mice showed significantly increased time engaging in stereotypic behaviors such as grooming and digging (Fig. 4E), and also exhibited a nesting deficit, considered by some to be a home-cage social behavior (Fig. 4F). Taken together, Dlx-cKO mice show a set of autistic-like features with relatively preserved learning and memory that stand in contrast to previous findings in Nex-cKO mice, which show selectively impaired learning and memory. These results demonstrate a segregation of behavioral deficits in *Cdk15* conditional knockout mice, suggesting that impaired learning and autistic-like features have distinct cellular origins in CDD.

Dlx-cKO mice show a non-cell autonomous enhancement of excitatory synaptic transmission

Although several functions of CDKL5 in excitatory neurons have been described, the role of CDKL5 in regulating inhibitory synaptic transmission is largely unknown. Given that CDKL5 protein is expressed in diverse populations of GABAergic neurons, we first assessed inhibitory synaptic transmission onto pyramidal neurons in the hippocampal CA1 region, which receive input from multiple GABAergic interneuron types. Surprisingly, recordings of miniature spontaneous inhibitory postsynaptic currents (mIPSCs) did not reveal significant differences in either amplitude, frequency, or kinetics between Dlx-cKO and wild type controls (Fig. 5A-F), suggesting that in adult Dlx-cKO mice, any alteration of inhibitory signaling directly onto pyramidal neurons is likely subtle. In contrast, when we examined excitatory neuron-to-excitatory neuron synaptic transmission through the recording of miniature spontaneous excitatory postsynaptic currents (mEPSCs) at CA1 pyramidal neurons, we found a significant enhancement of mEPSC frequency, but not amplitude, in Dlx-cKO mice (Fig. 6A-F). This finding suggests that as a result of the loss of CDKL5 in GABAergic neurons in mice, excitatory synaptic transmission is enhanced in a non-cell autonomous manner.

Dlx-cKO mice show aberrant paired-pulse facilitation leading to circuit hyperexcitability

The finding of enhanced excitatory synaptic transmission with relative sparing of inhibitory synaptic transmission suggests that Dlx-cKO mice may show hyperexcitability at the circuit level. We therefore interrogated the function of the perforant path-dentate gyrus pathway, a microcircuit that critically relies on both excitation and inhibition for

proper function and is often perturbed in disease states (Coulter et al., 2011; Dengler and Coulter, 2016; Goldberg and Coulter, 2013). Using voltage-sensitive dye imaging (Carlson and Coulter, 2008) as a readout, we assessed the layer-specific responses of the molecular layer, granule cell layer, as well as the downstream hilar region in response to paired-pulse stimulation (Fig. 7). At the inter-stimulus interval tested, wild type mice showed comparable responses to the first and second stimuli without significant facilitation or depression, whereas Nex-cKO mice showed a trend toward paired-pulse depression suggestive of circuit hypo-excitability (Fig. 7B-E). In contrast, Dlx-cKO mice exhibited enhanced paired-pulse facilitation, evident by an increase in depolarization upon a second successive stimulus (Fig. 7B-E). Furthermore, the facilitating response in Dlx-cKO mice is propagated through the granule cell layer to the downstream hilar region (Fig. 7A and data not shown). Taken together, these findings suggest that Dlx-cKO mice, in contrast to wild type and Nex-cKO mice, show an aberrant paired-pulse facilitation response that leads to circuit hyperexcitability upon repeated stimulation.

Acute NMDAR blockade ameliorates autistic-like features in CDKL5-deficient mice

The finding of enhanced excitatory synaptic transmission and circuit hyperexcitability in Dlx-cKO mice suggests that altered synaptic and circuit function may underlie aspects of behavior in *Cdkl5* constitutive knockout mice. A previous study found that excitatory synaptic transmission involving NMDA, rather than AMPA receptors, is selectively enhanced in *Cdkl5* knockout mice (Okuda et al., 2017). We therefore investigated the extent to which enhanced NMDA signaling is responsible for the behavioral deficits in CDKL5-deficient mice. We conducted our assays in a newly

generated *Cdkl5* knock-in mouse line (R59X), which carries an early nonsense mutation, mimicking a patient mutation, that results in the truncation of the catalytic domain of CDKL5 (Fig. 8A). Similar to our previously generated exon 6-deletion (knockout) mouse line, the R59X mutation was found to be a loss-of-function allele that led to the absence of full-length functional CDKL5 protein (Fig. 8B).

We first tested the possibility that enhanced NMDAR signaling may underlie impaired learning and memory in CDKL5-deficient mice. We used memantine, a non-competitive NMDA receptor blocker that has been previously found to rescue behavioral deficits in various mouse models of neurodevelopmental disorders (Chung et al., 2015; Figueiredo et al., 2013; Kang and Kim, 2015). Using the Y-maze as a preliminary screening assay, we found while R59X mice demonstrated a robust working memory deficit, acute memantine administration at a range of doses did not ameliorate this behavioral deficit (Fig. 9A). Notably, R59X mice also exhibit increased stereotypic behavior, characterized by prolonged bouts of grooming (Fig. 9B, C). Acute memantine administration significantly reduced both total time spent grooming and the duration of the longest grooming bout of R59X mice to a level similar to that of wild type controls (Fig. 9B, C). We also assessed social preference through a modified dyadic interaction assay, a quantitative assay of the time spent in direct social interaction with a novel stimulus mouse. Whereas vehicle-administered R59X mice showed significantly reduced social interaction, memantine ameliorated this deficit, significantly increasing the time spent by R59X mice in social interaction (Fig. 9D). This effect was specific to R59X mice, as memantine normalized the ratio of time spent in social interaction in pairs of R59X and wild type control mice co-tested side-by-side in identical cages (Fig. 9E).

Taken together, these results suggest that enhanced NMDAR signaling underlies autistic-like features, but not learning and memory deficits, in CDKL5-deficient mice.

Discussion

Segregation of behavioral deficits in *Cdkl5* conditional knockout mice

Our behavioral studies in Dlx-cKO mice revealed a set of autistic-like features characterized by reduced social preference and increased stereotypic behaviors, but relative preservation of other behaviors such as learning and memory, motor coordination, and anxiety-related behaviors. This behavioral profile stands in contrast to our previous findings in Nex-cKO mice, which exhibit selectively impaired learning and memory. Taken together, our results demonstrate a relative segregation of behavioral phenotypes of the *Cdkl5* constitutive knockout mice in Nex- and Dlx-cKO mice, suggesting that impaired learning primarily originates from the loss of CDKL5 in forebrain glutamatergic neurons, whereas autistic-like features primarily originate from the loss of CDKL5 in forebrain GABAergic neurons. Several phenotypes of constitutive knockout mice, including altered anxiety-related behavior, locomotion, and motor coordination, were not altered in either Nex-cKO and Dlx-cKO mice. These additional phenotypes may be mediated by 1) CDKL5 function in other cell populations and brain regions and/or 2) the synergistic functions of CDKL5 in forebrain glutamatergic and GABAergic neurons.

Excitation-inhibition imbalance in Dlx-cKO mice

In our electrophysiologic studies of Dlx-cKO mice, the most prominent change was, surprisingly, an enhancement in glutamatergic synaptic transmission. This change likely arises from a non-cell autonomous mechanism, especially in the absence of a concomitant change in GABAergic-glutamatergic inhibitory synaptic transmission. One possible explanation is that the loss of CDKL5 in GABAergic interneurons lead to a modulation of presynaptic release probability at glutamatergic synapses. A second explanation is that a transient alteration of GABAergic signaling earlier in development led to altered excitatory synaptogenesis, which persisted into adulthood. Interestingly, previous studies have found that GABAergic transmission cooperates with NMDA receptor activation during development for excitatory synapse formation (Wang and Kriegstein, 2008).

At the circuit level, our findings in Dlx-cKO mice suggest an excitation-inhibition imbalance that favors overall hyperexcitability. The paired-pulse stimulation paradigm assesses, in a frequency-dependent manner, the integration of excitatory and inhibitory synaptic transmission in the dentate gyrus and propagation to downstream regions. Previous work has shown that NMDA signaling is a necessary component for the paired-pulse facilitation response in the dentate gyrus, suggesting a potential mechanism for circuit excitability in Dlx-cKO mice (Joy and Albertson, 1993). Importantly, the response in Dlx-cKO mice strongly contrasts with that of Nex-cKO mice, which showed a tendency for paired-pulse depression and circuit hypo-excitability. Taken together, these results support a model by which CDKL5 loss in glutamatergic and GABAergic neurons lead to divergent changes in excitation-inhibition balance to generate distinct behavioral deficits.

NMDAR signaling underlies several behavior deficits in CDKL5-deficient mice

The finding of enhanced NMDAR signaling revealed a novel synaptic mechanism that may potentially underlie the behavioral deficits of CDKL5-deficient mice. Our results suggest that the acute reduction of NMDAR signaling ameliorates some, but not all features of CDD. Specifically, whereas acute memantine administration rescued repetitive behavior and significantly improved social interaction in R59X mice, it did not positively affect the learning and memory deficit of R59X mice. These results suggest that the behavioral deficits of CDD may have origins in additional or distinct synaptic mechanisms. For example, altered AMPA receptor-dependent synaptic transmission and altered inhibitory synaptic transmission have both been previously reported in CDD. Furthermore, subtypes of NMDA receptors, which are expressed in distinct patterns across brain regions (Goebel and Poesch, 1999), may contribute differentially to various behavioral deficits in CDKL5-deficient mice.

Taken together, our studies delineate the forebrain GABAergic origins of autistic-like features in CDKL5-deficient mice, showing for the first time that CDKL5 is required in this diverse population of neurons for proper neural development and function. At the synaptic and circuit levels, we reveal a non-cell autonomous mechanism that contributes to hyperexcitability in CDKL5-deficient mice. Finally, we show that acute reduction of NMDAR signaling can ameliorate certain behavioral deficits in CDKL5-deficient mice, highlighting a potentially important mechanism for development of CDD-related phenotypes in mice and supporting a novel therapeutic avenue for the treatment of these symptoms in humans.

Materials and Methods

The behavioral assay protocols here are identical to those described for the study of Nex-cKO mice (Chapter 2), with additional protocols and details elaborated below.

Mouse strains. The *Cdkl5* floxed mouse line with Cre-dependent excision of exon 6 (Tang et al. 2017) was used for the generation of conditional knockout mice. Dlx5/6-Cre, a mouse line expressing Cre in forebrain inhibitory neurons (Monory et al., 2006), was obtained from Jackson Laboratories (Stock No. 008199). The CDKL5 R59X knock-in line was generated as follows: a targeting vector was designed to insert a *frt*-flanked neomycin resistance (*neo*) cassette downstream of exon 5, and a single nucleotide change of C to T, leading to a nonsense mutation at arginine 59 (R59X) of the *Cdkl5* gene. The construct was electroporated into C57BL/6N embryonic stem (ES) cells. Correctly targeted ES cells were injected into BALB/c blastocysts and resulting chimeric mice were bred with B6.Cg-Tg(ACTFLPe)9205Dym/J (Jackson Laboratories, Stock No. 005703) to remove the *neo* cassette. Resulting offspring were bred to C57BL/6J mice (Jackson Laboratories, Stock No. 000664) for at least 10 generations. The R59X knock-in mouse line has been deposited at Jackson Laboratories (Stock No. 028856).

Mouse husbandry. Experiments were conducted in accordance with the ethical guidelines of the National Institutes of Health and with the approval of the Institutional Animal Care and Use Committee of the University of Pennsylvania. *Cdkl5*^{flox}, Dlx5/6-Cre, and R59X mice were backcrossed to C57BL/6 for at least 10 generations before breeding for experiments. Mouse lines were genotyped using a PCR-based strategy,

with their respective primer sequences and other details found on the Jackson Laboratories website under the appropriate stock numbers listed above. Mice were group-housed in cages of three to five in a 12-h light/dark cycle with food and water provided ad libitum.

For breeding of Dlx-cKO and wild type control mice, each breeding cage consisted of two homozygous female mice (genotype: *Cdkl5^{fllox}/Cdkl5^{fllox}*) and one male mouse (genotype: *Dlx5/6-Cre/+*). Male littermates (genotypes: *Cdkl5^{fllox}/y;+/+* and *Cdkl5^{fllox}/y; Dlx5/6-Cre*) were weaned at 3 weeks of age and housed together, with all experiments performed on age-matched adult mice between 9 and 12 weeks of age. For some behavioral experiments, wild type control mice (genotype: *Cdkl5^{fllox}/y;+/+*) from Nex-cKO breedings (Tang et al. 2017) were pooled with wild type control mice from Dlx-cKO breedings (genotype: *Cdkl5^{fllox}/y;+/+*).

For breeding of R59X and wild type control mice, each breeding cage consisted of two heterozygous female mice (genotype: *R59X/+*) and one male mouse (genotype: *+/y*). Male littermates (genotypes: *R59X/y* and *+/y*) were weaned at 3 weeks of age and housed together, with all experiments performed on age-matched adult mice between 9 and 12 weeks of age.

Western blot. Adult male mice were sacrificed by cervical dislocation. After decapitation, brains were removed and sectioned into 1 mm coronal slices using a mouse brain matrix. Tissue was dissected from the somatosensory cortex, striatum, hippocampus, and cerebellum and homogenized in lysis buffer containing 1% NP-40, pH 8.0. Protein concentration was measured using the Bradford assay and a total of 20 μ g protein was loaded for each lane. Primary antibodies used in this study are anti-N-

terminal CDKL5 (generated in Wang et al, 2012; diluted 1:500), anti-GAPDH (MA5-15738, Invitrogen; RRID: AB_10977387; diluted 1:1000), anti-EB2 (AB45767, Abcam, diluted 1:1000). Secondary antibodies (Licor) are goat anti-rabbit IRDye 800CW (RRID: AB_10796098) and donkey anti-rabbit IRDye 680RD (RRID: AB_10954442) at dilutions of 1:10,000. Standard protocols were used for the Odyssey Infrared Imaging System for visualization and quantification.

Behavioral assays. All animal behavioral studies were carried out blinded to genotype. Mice were allowed to habituate to the testing room for at least 1 hour before the test, and testing was performed at the same time of day. All animal behaviors were performed on adult male mice at 9-12 weeks of age, and the analysis of behavioral data was carried out by a researcher blinded to genotype.

Dyadic interaction. The dyadic interaction test is an abbreviated version of the three-chambered assay to quantitatively assess the duration of direct social interaction in two freely behaving mice. One week prior to the assay, male R59X and wild type control mice were singly housed to increase the motivation for social interaction and reduce aggression. Age-matched, novel, wild type male stimulus mice were group-housed. On the day of the test, test and stimulus mice were acclimated to the room for 1 hour prior to the start of the assay. Following this period, each test mouse is placed individually in a clear, round Plexiglass cage (Pinnacle Technology, Lawrence, Kansas, USA) measuring 8 inches tall and 9.5 inches in diameter, with a thin layer of bedding. Following 30 minutes of habituation in the cage, a novel, age-matched stimulus mouse was placed into the cage, and the mice were allowed to freely interact under video monitoring for 10 min. The total duration of social interaction initiated by the test mouse in the first 2 minutes was scored, and this included oro-genital sniffing, oro-facial sniffing,

close following, placing one or both paws on the stimulus mouse, or allogrooming of the stimulus mouse. “Co-tested pairs” refer to side-by-side tests involving two littermate R59X and wild type control mice, each interacting with a novel stimulus mouse in a separate cage.

Drug administration. Mice were acclimated to daily intraperitoneal (i.p.) injections of vehicle (saline) for three days prior to each set of behavioral assays. For each behavioral cohort, the entire cohort was administered either vehicle or drug, with the experimenter blinded to the genotypes of mice throughout. All animal behaviors were performed on adult male mice at 9-12 weeks of age, and the analysis of behavioral data was carried out by a researcher blinded to genotype. Vehicle and drug (memantine hydrochloride, Tocris Biosciences, United Kingdom) were diluted in saline at 10 μ L per gram mouse body weight for administration. Vehicle or drug was administered 1 hour prior to the start of each behavioral assay, and during this period, mice were allowed to habituate in the room where the assay would be carried out.

Ex vivo slice preparation. All steps of electrophysiological experiments, including data collection and analysis, were performed by a researcher blinded to genotype. Acute hippocampal slices were prepared from mice 9 to 12 weeks of age. Animals were anesthetized with isoflurane and transcardially perfused with ice-cold oxygenated (95% O₂, 5% CO₂) cutting artificial cerebrospinal fluid (aCSF) solution (comprised of (mM): 2.5 KCl, 1.25 NaH₂PO₄, 5 MgSO₄, 0.5 CaCl₂, 200 sucrose, 25 NaHCO₃, 25 glucose, ~300 mOsm, 7.2-7.4 pH). After decapitation, brains were removed for sectioning in the same ice-cold cutting aCSF using a Vibratome (Leica Microsystems 1200S). For whole-cell patch-clamp recordings of mE/IPSCs and the measurement of intrinsic membrane properties, 350- μ m transverse hippocampal sections were prepared.

For all voltage-sensitive dye experiments, 400- μm transverse hippocampal sections were prepared. Slices were recovered in the same cutting aCSF solution at 32 °C for 30 min and transferred to an oxygenated room-temperature solution composed of 50% cutting aCSF and 50% regular aCSF (comprised of (mM): 125 NaCl, 2.5 KCl, 1.25 NaH_2PO_4 , 10 glucose, 26 NaHCO_3 , 2 CaCl_2 , 1 MgCl_2 , ~300 mOsm, 7.2-7.4 pH) for 30 min. Subsequently, slices were transferred to 100% regular aCSF at room temperature for an additional 30 min before recording. All recordings were performed at 34 °C.

mEPSCs. A pipette internal solution comprised of (mM): 140 KCH_3OSO_3 , 5 KCl, 0.5 EGTA, 1 MgCl_2 , 10 HEPES, 5 MgATP, 0.25 NaGTP, ~292 mOsm, $E_{\text{Cl}} = -78.8$ mV was used. Pipettes 4-6 M Ω in resistance were pulled from borosilicate glass capillaries (World Precision Instruments, 1B150F-4) on a Sutter Instruments P-1000 pipette puller. Voltage-clamp traces 5 min in duration were recorded at a holding potential of -70 mV in the presence of 1 μM tetrodotoxin (Tocris). All recordings were conducted with access resistance of less than 20 M Ω , leak current of less than 100 pA, and an applied series resistance compensation of 80%. Cells that did not maintain these parameters for the duration of the recording were eliminated. Analysis of mEPSCs was performed using pCLAMP10 (Axon Instruments, Molecular Devices) using a variable-amplitude template method, generated from a stable recording of at least 50 mEPSC events. Each trace was first low-pass filtered at 1 kHz, and negative-going mEPSCs were detected using a template match threshold of 4, without fitting.

mIPSCs. In order to record mIPSCs while maintaining a hyperpolarized membrane voltage, a high-chloride pipette internal solution (comprised of (mM): 100 $\text{CsCH}_3\text{O}_3\text{S}$, 50 CsCl, 10 HEPES, 0.2 BAPTA, 3 KCl, 1 MgCl_2 , 0.25 GTP-Tris, 2.5 creatine phosphate disodium, 2 MgATP, ~296 mOsm, $E_{\text{Cl}} = -23.7$ mV) was used.

Pipettes 4-6 M Ω in resistance were pulled from borosilicate glass capillaries (World Precision Instruments, 1B150F-4) on a Sutter Instruments P-1000 pipette puller. Voltage-clamp traces 3 min in duration were recorded at a holding potential of -70 mV in the presence of 1 μ M tetrodotoxin (Tocris) and 2 mM kynurenic acid (Sigma Aldrich). All recordings were conducted with access resistance of less than 20 M Ω , leak current of less than 100 pA, and an applied series resistance compensation of 80%. Cells that did not maintain these parameters for the duration of the recording were eliminated. Analysis of mIPSCs was performed using pCLAMP10 (Axon Instruments, Molecular Devices) using a variable-amplitude template method, generated from a stable recording of at least 50 mIPSC events. Each trace was first low-pass filtered at 1 kHz, and negative-going mIPSCs were detected using a template match threshold of 4, without fitting.

Voltage-sensitive dye imaging. Following recovery, each slice was bulk-loaded with 100 μ L of a solution containing the voltage-sensitive dye di-2-ANEPEQ (Antić and Zecević, 1995; Habib-E-Rasul Mullah et al., 2013) (JPW1114, Molecular Probes) diluted at 0.05 mg/mL in aCSF. Each slice was stained for 14 min, washed with aCSF, and imaged in an interface chamber using an 80x80 CCD camera recording with a 1 kHz frame rate (NeuroCCD; RedShirt Imaging). Illumination was provided by a 530 nm Green LED (Thor Labs, M530L3-C2). A filter set (Chroma Technologies 11007v2 wide Green) was used to allow excitation at 510-560 nm and collection of emitted fluorescence at a wavelength >592 nm.

A concentric bipolar tungsten microelectrode was used for stimulation of the perforant path. Two successive stimuli were applied with an inter-stimulus interval of 200 ms. Two stimulation intensities (200 μ A and 400 μ A) were used. Imaging trials lasted a

total of 1000 ms each, with a 20 s inter-trial interval. Interleaved trials without stimulation allowed for background subtraction.

All data analysis was performed in IGOR (Wavemetrics) on the average of 12 trials. Data were displayed as the change in fluorescence divided by the resting fluorescence ($\Delta F/F$). Regions of interest (ROIs) were drawn for the molecular layer of the dentate gyrus, the dentate granule cell layer, and the hilus. Like other dyes of the ANEPP family, di-2-ANEPEQ decreases in fluorescence upon membrane depolarization. To be consistent with electrophysiological conventions, depolarizing $\Delta F/F$ signals were displayed as upward signals (warmer colors) and hyperpolarization $\Delta F/F$ signals were displayed as downward signals (colder colors). Snapshots of VSDI represent an 80x80 pixel window, corresponding to an approximately 1.7 x 1.7 mm field of view.

Statistical analyses. For behavioral assays involving *Dlx-cKO* mice, we chose similar sample sizes for all behavioral experiments based on previous published studies of *Cdkl5* constitutive knockout mice (Wang et al. 2012) and *Cdkl5* glutamatergic conditional knockout mice (Tang et al. 2017). For behavioral assays involving drug administration, we used saline-administered pilot cohorts to estimate effect sizes required for detecting significant wild type-mutant differences and used similar sample sizes for drug-administered cohorts. Importantly, the number of mice used were pre-determined prior to the start of each experiment.

For behavioral assays, statistical analyses were performed using Prism (GraphPad). All data sets were analyzed using the Shapiro-Wilk test for normality. Data sets with normal distributions were analyzed for significance using unpaired Student's two-tailed *t*-test. Data sets with non-normal distribution were analyzed using the Mann-

Whitney test. Two-way repeated measures ANOVA or the Kruskal-Wallis test was conducted for the appropriate data sets with Holm-Sidak's multiple comparison test, using adjusted $*p < 0.05$.

All other assays that involved sub-sampling of animals were analyzed using R (The R Project for Statistical Computing). Each data set was analyzed using a "linear mixed effect model," where *Genotype* was modeled as a fixed effect term and *Animal* was modeled as a random effect term. This model accounts for both between-animal and between-cell variation. For each assay, null and alternative models were constructed using the *lmer* function in the *lme4* package (Bates et al., 2015) in the following format:

$$m0 = \text{lmer}(\text{Outcome} \sim (1 \mid \text{Animal}), \text{REML}=\text{TRUE})$$
$$m1 = \text{lmer}(\text{Outcome} \sim \text{Genotype} + (1 \mid \text{Animal}), \text{REML}=\text{TRUE})$$

For data sets involving a third term (e.g. cumulative frequency bin), the following null and alternative models were constructed, in order to test the significance of an interaction between *Genotype* and the third term:

$$m0 = \text{lmer}(\text{Outcome} \sim \text{Bin} + \text{Genotype} + (1 \mid \text{Animal}), \text{REML}=\text{TRUE})$$
$$m1 = \text{lmer}(\text{Outcome} \sim \text{Bin} * \text{Genotype} + (1 \mid \text{Animal}), \text{REML}=\text{TRUE})$$

To make statistical comparisons, the *KRmodcomp* function from the *pbkrtest* package (Halekoh and Højsgaard, 2014) was used:

$$\text{KRmodcomp}(m0, m1)$$

The KRmodcomp function reports a modified F-test statistic based on the Kenward and Roger approximation (Kenward and Roger, 1997), which accounts for the small sample sizes in our study, modified numerator and denominator degrees of freedom, and a p-value. The estimated effect of Genotype is obtained from the alternative model constructed using the *lmer* function from lme4.

Post-hoc testing for linear mixed effect models (e.g. at cumulative frequency bins) was performed using the least-squares means method for multiple comparisons. The *lsmeans* package was used (Lenth, 2016) on the alternative model generated by *lmer*:

```
lsmeans(m1, pairwise ~ Genotype | Bin, mode='kenward-roger')
```

For the analysis of cumulative distributions (mEPSC and mIPSC inter-event intervals and amplitudes), all samples from each individual cell was sorted, binned, and averaged at percent intervals, effectively generating a binned cumulative distribution curve for each cell. Data from all cells of a given genotype were plotted at these distinct binned percent intervals with the mean and error bars indicating s.e.m. The results were analyzed using linear mixed effect models, incorporating a third term, “cumulative frequency bin.”

All graphs are plotted using Prism (GraphPad). In our figures, p-values between 0.05 and 0.1 are shown explicitly, * is used to denote all $0.01 < p < 0.05$, ** for $0.001 < p < 0.01$, *** for $0.0001 < p < 0.001$, and **** for $p < 0.0001$.

Figures

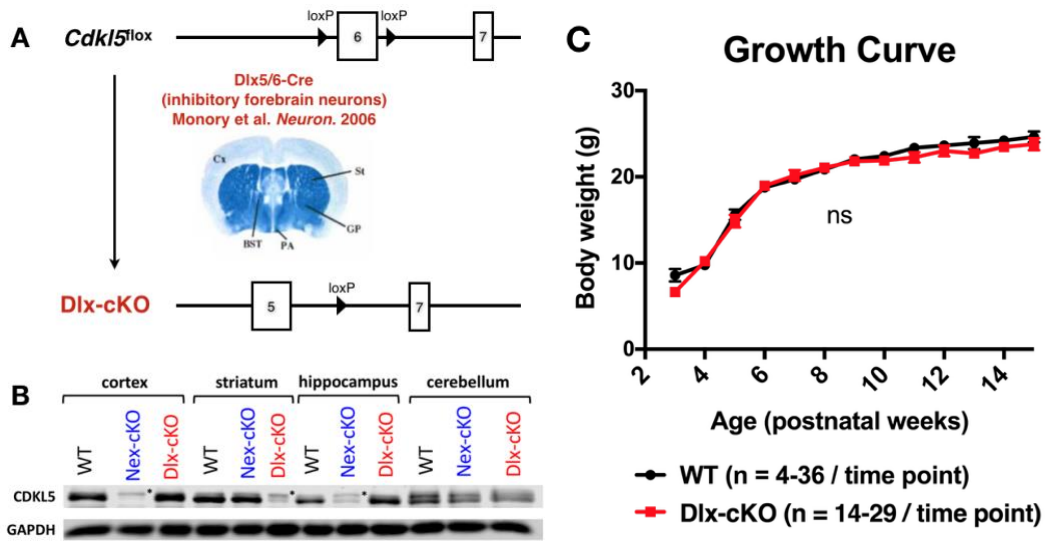


Figure 1. Generation and validation of mice lacking CDKL5 selectively in forebrain GABAergic neurons (Dlx-cKO).

(A) Schematic representing the generation of Dlx-cKO mice using a conditional exon 6-floxed *Cdkl5* mouse line (Tang et al., 2017) and the Dlx5/6-Cre driver (Monory et al., 2006). (B) Validation of the cell type-specificity of CDKL5 protein knockout using microdissected brain tissue. Dlx-cKO mice are compared to both WT and Nex-cKO (forebrain glutamatergic conditional knockout mice) (Tang et al., 2017). In regions enriched for glutamatergic neurons (e.g. cortex and hippocampus), Nex-cKO but not Dlx-cKO mice show a reduction in CDKL5 protein. In regions enriched for GABAergic neurons (e.g. striatum), Dlx-cKO mice but not Nex-cKO mice show a reduction in CDKL5 protein. In other brain regions (e.g. cerebellum), neither Dlx-cKO nor Nex-cKO mice show reductions in CDKL5 protein. Asterisk indicates non-specific band. (C) Unaltered body weight of Dlx-cKO mice at various ages.

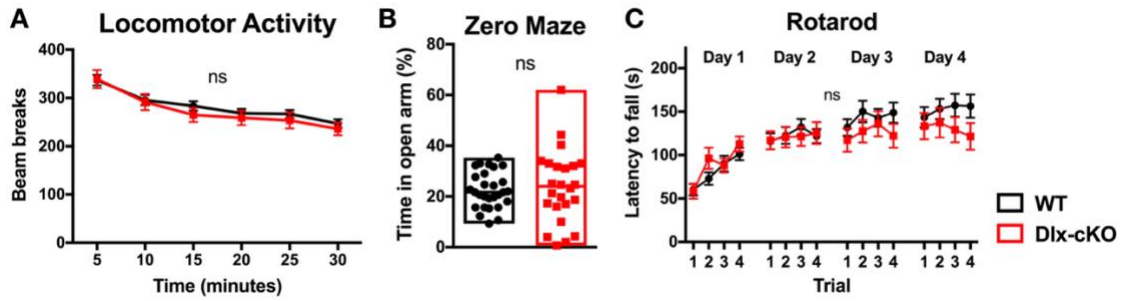


Figure 2. Dlx-cKO mice show unaltered locomotion, anxiety-related behavior, and motor coordination.

(A) Dlx-cKO mice show unaltered home-cage locomotion on the beam break assay. (B) Dlx-cKO mice, show unaltered anxiety-related behavior, as assessed by the percent time spent in open arms, on the elevated zero maze assay. (C) Dlx-cKO mice show unaltered motor coordination and learning on the Rotarod assay.

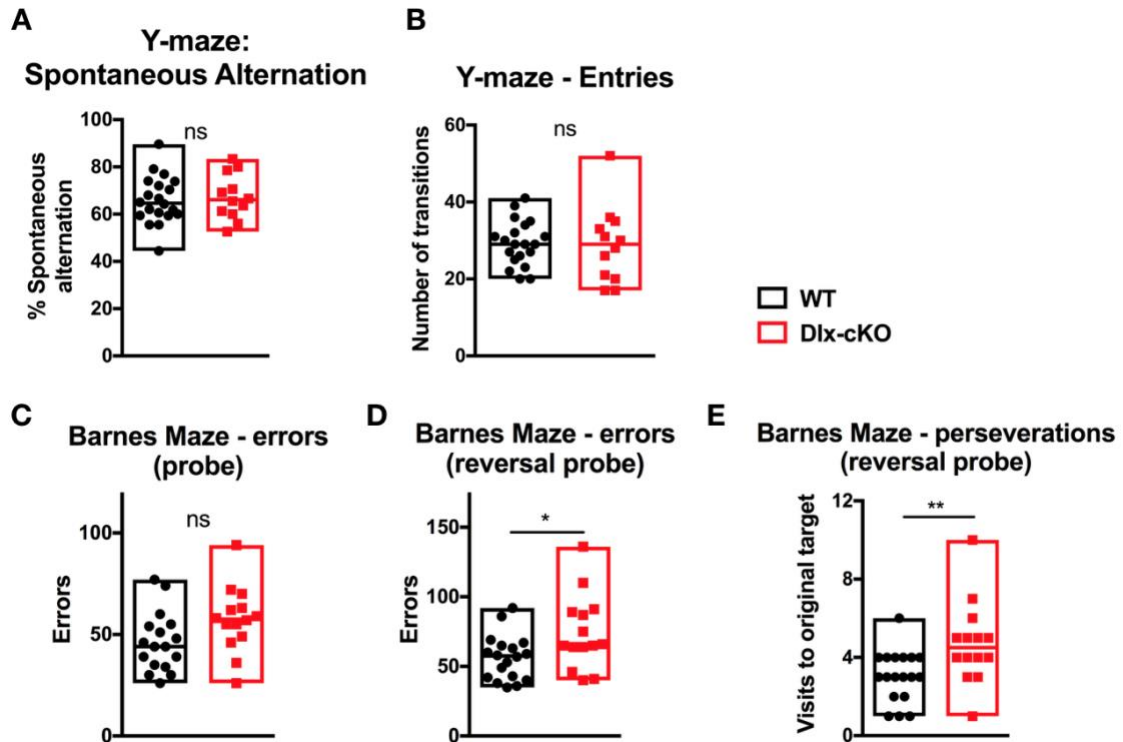


Figure 3. Dlx-cKO mice show preserved learning and memory, but impaired cognitive flexibility.

(A) Dlx-cKO mice show unaltered spontaneous alternation percentage in comparison to WT mice (WT, $n = 20$; Dlx-cKO: $n = 12$; unpaired t -test, ns). (B) The total number of entries made were not significantly different between Dlx-cKO and WT mice (unpaired t -test, ns). (C) Dlx-cKO mice did not show a significant difference in the total number of errors made on forward probe trials of the Barnes maze (WT, $n = 18$; Dlx-cKO: $n = 14$; unpaired t -test, ns). (D) Dlx-cKO mice made significantly more errors on the reversal probe trials of the Barnes maze (unpaired t -test, $p = 0.025$). (E) On the reversal probe trials, Dlx-cKO mice also made significantly more perseverations, or visits to the original target hole location (Mann-Whitney test, $p = 0.0061$).

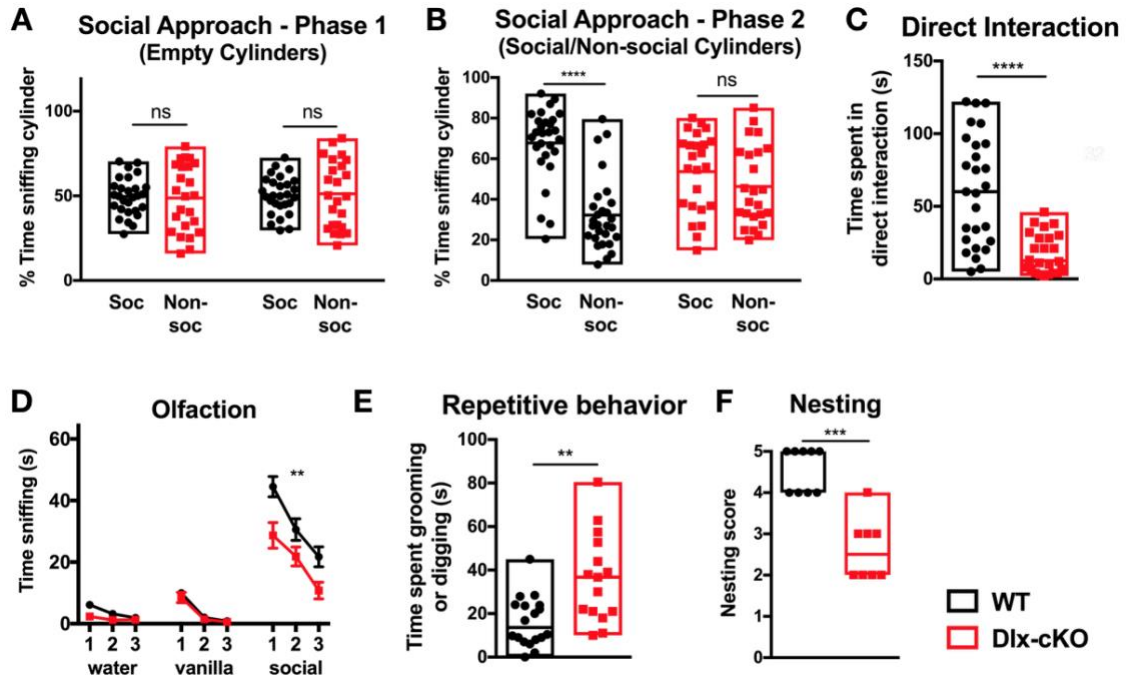


Figure 4. Dlx-cKO mice show reduced sociability, increased stereotypic behaviors and impaired nesting.

(A) Dlx-cKO mice showed similar times spent interacting with empty cylinders during the habituation phase of the three-chambered assay (WT, $n = 28$; Dlx-cKO, $n = 26$; unpaired t -tests, ns). (B) In contrast to wild type control mice, which showed a significant preference for interacting with the cylinder containing a social stimulus, Dlx-cKO mice did not show a significant difference in time spent sniffing the social and non-social cylinders (WT, Mann-Whitney test, $p < 0.0001$; Dlx-cKO, unpaired t -test, ns). (C) During the direct interaction phase of the assay, Dlx-cKO mice also spent significantly reduced time initiating social contact (Mann-Whitney test, $p < 0.0001$). (D) In the olfactory habituation-dishabituation test, Dlx-cKO mice showed unaltered ability to discriminate between odors and habituation to the same odor upon repeated presentation. However, Dlx-cKO mice show a reduced time sniffing a social scent compared to WT (WT, $n = 20$; Dlx-cKO, $n = 14$; two-way ANOVA with Holm-Sidak's multiple comparisons test: effect of trial, $p < 0.0001$; effect of genotype, $p = 0.0035$; effect of interaction, $p < 0.0001$). (E) Dlx-cKO mice spent significantly increased duration engaging in repetitive behaviors, including grooming and digging, in a home cage-like environment (WT, $n = 18$; Dlx-cKO, $n = 16$; unpaired t -test, $p = 0.0028$). (F) Dlx-cKO mice show significantly reduced nesting scores on the nesting assay (WT, $n = 9$; Dlx-cKO, $n = 8$; Mann-Whitney test, $p = 0.0002$).

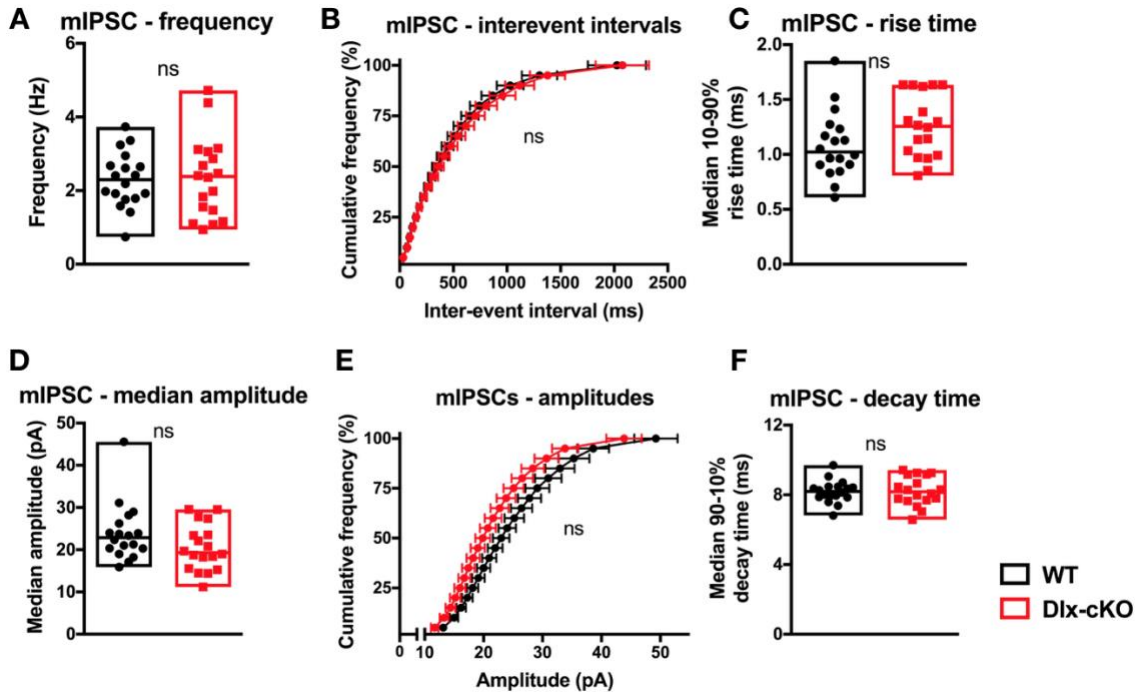


Figure 5. Unaltered inhibitory synaptic transmission at CA1 pyramidal neurons in Dlx-cKO mice.

(A) Dlx-cKO mice show unaltered mIPSC frequency at CA1 pyramidal neurons (WT, $n = 18$ cells / 3 mice; Dlx-cKO, $n = 18$ cells / 3 mice; linear mixed effect analysis, effect of genotype, ns). (B) The cumulative frequency distributions of mIPSC inter-event intervals were not significantly different between Dlx-cKO and WT mice (linear mixed effect analysis, effects of genotype and interaction, ns). (C) Dlx-cKO mice show unaltered median 10-90% mIPSC rise times (linear mixed effect analysis, effect of genotype, ns). (D) The median amplitude of mIPSCs is not significantly different between Dlx-cKO and WT mice (linear mixed effect analysis, effect of genotype, ns). (E) The cumulative frequency distributions of mIPSC amplitudes are not significantly different between Dlx-cKO and WT mice (linear mixed effect analysis, effects of genotype and interaction, ns). (F) Dlx-cKO mice show unaltered median 90-10% decay times at mEPSCs (linear mixed effect analysis, effect of genotype, ns).

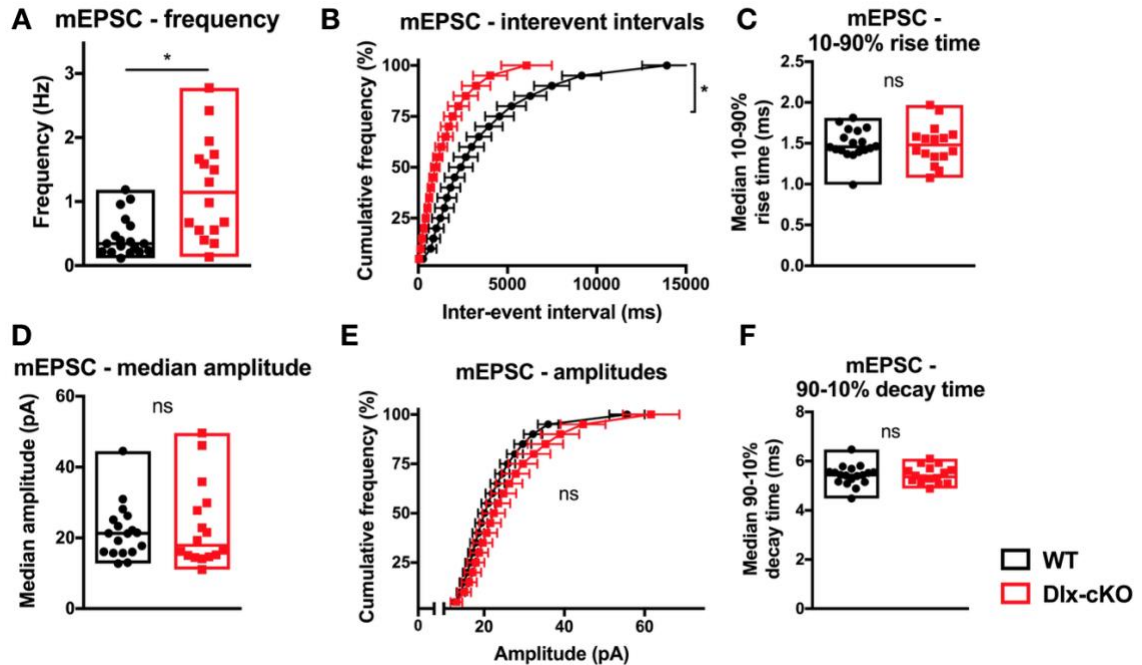


Figure 6. Dlx-cKO mice show a non-cell autonomous enhancement of excitatory synaptic transmission.

(A) Dlx-cKO mice show significantly enhanced mEPSC frequency at CA1 pyramidal neurons (WT, $n = 18$ cells / 3 mice; Dlx-cKO, $n = 16$ cells / 3 mice; linear mixed effect analysis, effect of genotype, $p = 0.034$). (B) The cumulative frequency distribution of mEPSC inter-event intervals is also significantly shifted in Dlx-cKO mice (linear mixed effect analysis with least-square means post-hoc testing, effect of genotype, $p = 0.096$, effect of interaction, $p = 2.3 \times 10^{-10}$). (C) The median 10-90% rise time of mEPSCs is unaltered in Dlx-cKO mice (linear mixed effect analysis, effect of genotype, ns). (D) The mEPSC median amplitude is unaltered in Dlx-cKO mice (linear mixed effect analysis, effect of genotype, ns). (E) The cumulative frequency distributions of mEPSC amplitudes are not significantly different between Dlx-cKO and WT mice (linear mixed effect analysis, effects of genotype and interaction, ns). (F) The median 90-10% decay times of mEPSCs is unaltered in Dlx-cKO mice (linear mixed effect analysis, effect of genotype, ns).

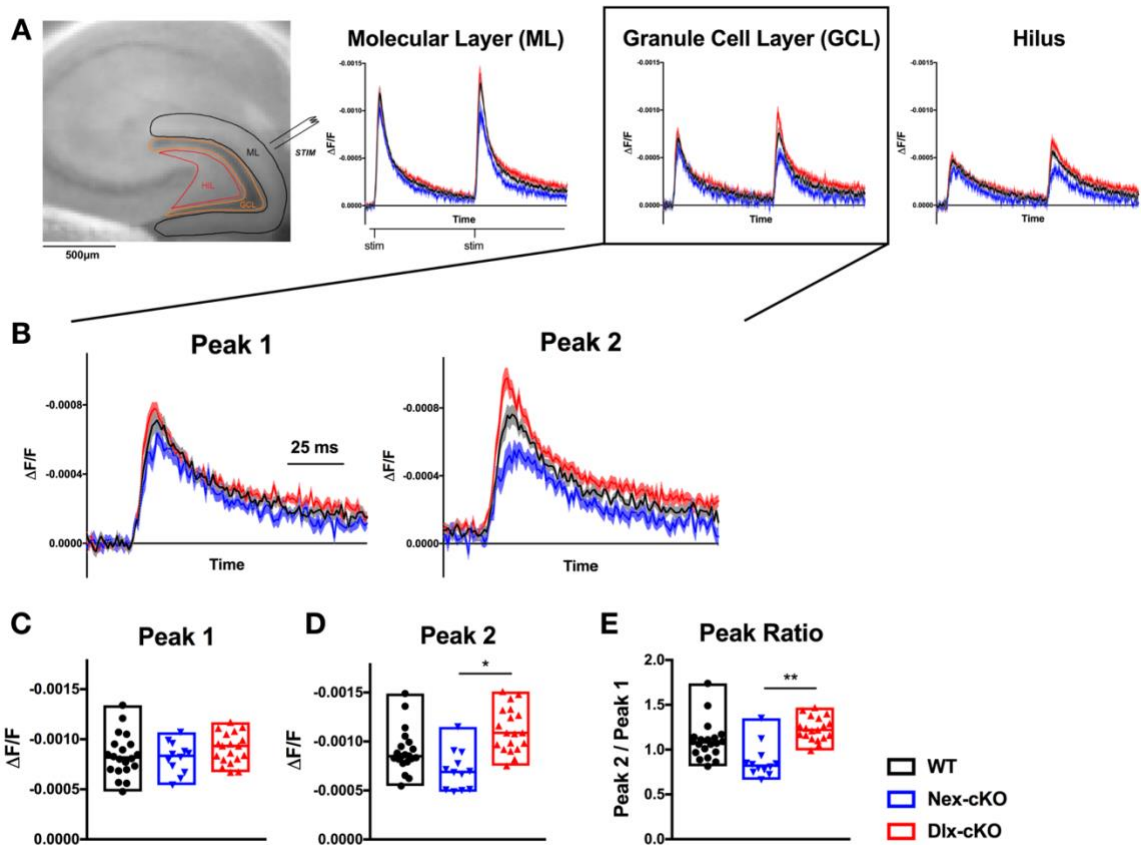


Figure 7. Dlx-cKO mice show aberrant paired-pulse facilitation.

(A) Schematic of voltage-sensitive dye imaging (VSDI) showing the site of stimulation at the perforant path and regions of interest (ROIs) used for analysis. ML: *molecular layer of the dentate gyrus*; GCL: *dentate granule cell layer*; HIL: *hilar region*. Averaged VSDI responses in response to a pair of stimuli (200 μ a intensity, 200 ms inter-stimulus interval) in the respective layers. Following current-clamp convention, depolarization (decrease in $\Delta F/F$) is displayed as an upward signal, while hyperpolarization (increase in $\Delta F/F$) is displayed as a downward signal. Error envelopes represent mean \pm s.e.m. (B) Zoomed-in views of peak VSDI responses of the GCL in WT, Nex-cKO and Dlx-cKO mice. (C) Peak amplitudes of the response to the first stimulus were not different between WT, Nex-cKO, and Dlx-cKO mice (linear mixed effect analysis, ns). (D) Peak amplitudes of the response to the second stimulus were significantly different between Nex-cKO and Dlx-cKO mice (linear mixed effect analysis with Tukey's correction for multiple comparisons: overall, $p = 0.024$; Nex-cKO vs Dlx-cKO, $p = 0.021$). (E) Ratios of peak amplitudes were significantly different between Nex-cKO and Dlx-cKO mice (linear mixed effect analysis with Tukey's correction for multiple comparisons: overall, $p = 0.012$; Nex-cKO vs Dlx-cKO, $p = 0.0092$). For all experiments, $n=20$ slices/5 mice for WT, $n = 12$ slices / 4 mice for Nex-cKO, and $n = 19$ slices / 5 mice for Dlx-cKO.

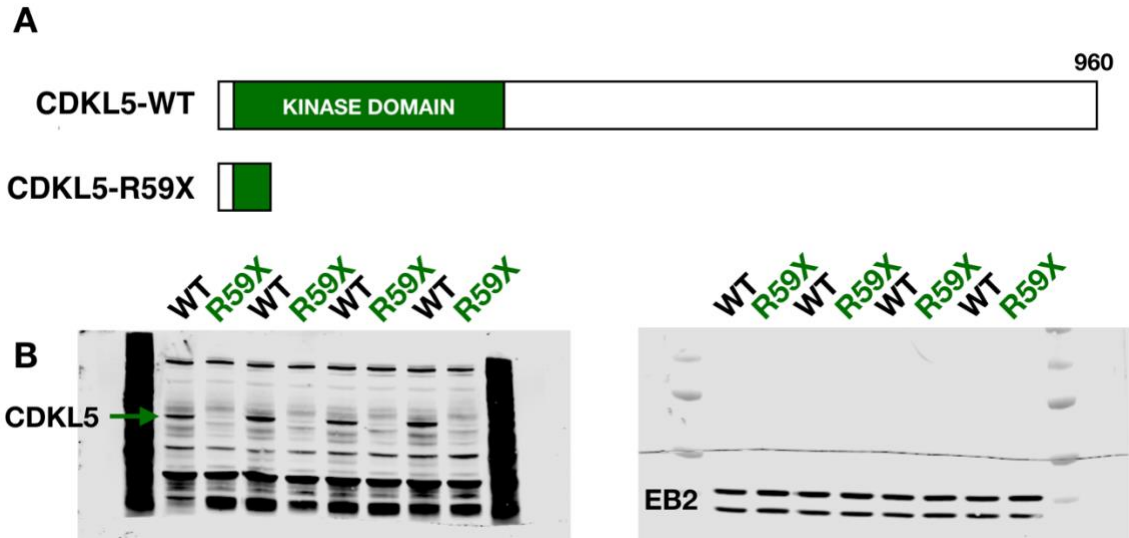


Figure 8. Generation of CDKL5 R59X knock-in mice.

(A) Schematic of the R59X non-sense mutation at arginine 59, which results in early truncation of the catalytic domain of CDKL5. (B) Validation of CDKL5 protein loss in R59X and wild type control male mice. Western blots of dissected whole cortex lysate in WT and R59X mice. Green arrow indicates band corresponding to CDKL5 protein. Total EB2 protein was used as a loading control.

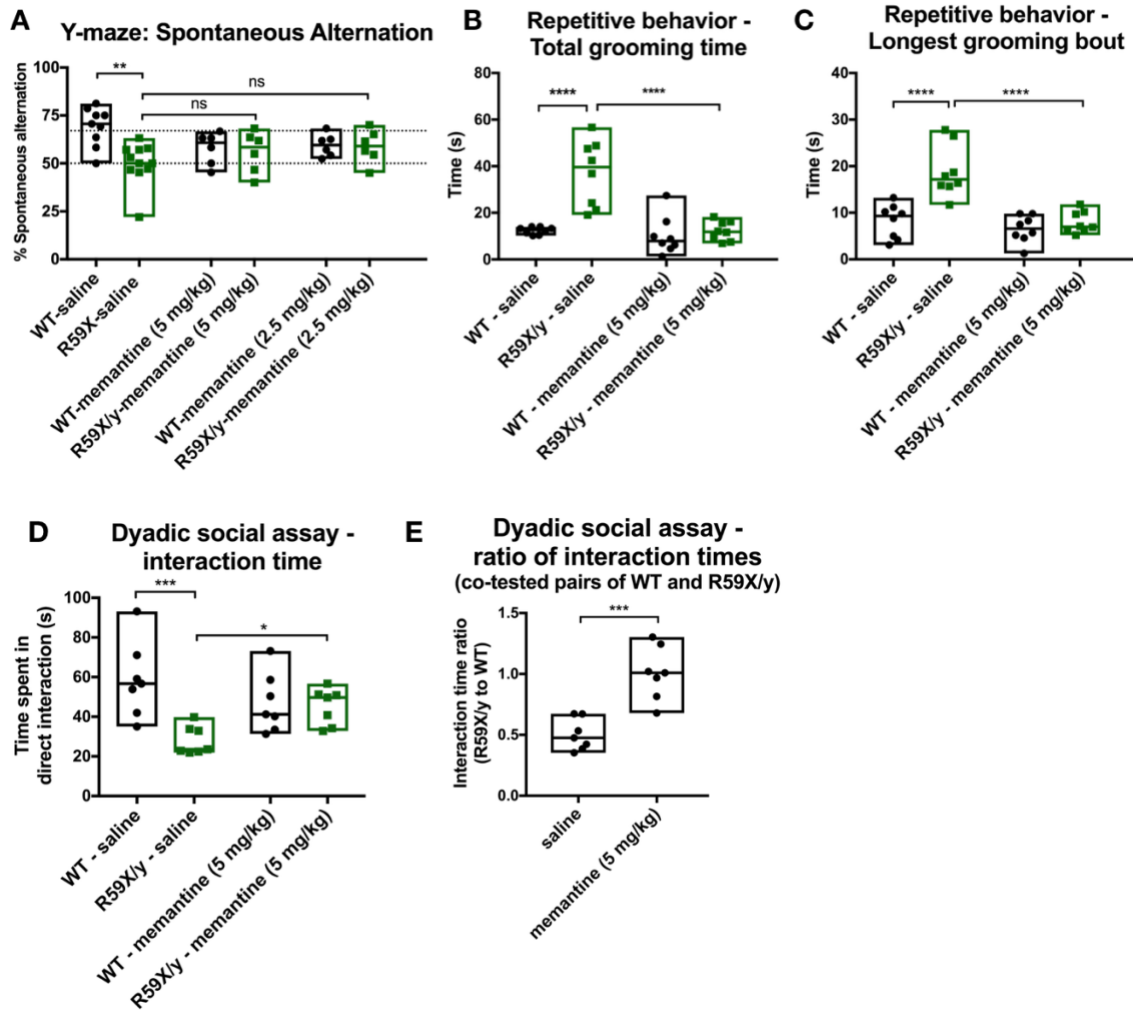


Figure 9. Acute NMDAR blockade ameliorates autistic-like features, but not learning and memory, in CDKL5-deficient mice.

(A) Spontaneous alternation percentage is significantly reduced in saline-treated R59X mice in comparison to WT mice. However, acute memantine administration at either 2.5 or 5 mg/kg doses did not significantly rescue the spontaneous alternation deficit (WT-saline, $n = 9$; R59X-saline, $n = 11$; WT-memantine (5 mg/kg), $n = 6$; R59X-memantine (5 mg/kg), $n = 6$; WT-memantine (2.5 mg/kg), $n = 6$; R59X-memantine (2.5 mg/kg), $n = 6$; Kruskal-Wallis test with Dunn's multiple comparisons test, $p = 0.014$; WT-saline vs R59X-saline, $p = 0.0027$). (B) Total grooming in a home cage-like environment is significantly increased in saline-treated R59X mice in comparison to WT, and memantine at 5 mg/kg significantly ameliorated the increased grooming phenotype in R59X mice ($n = 8$ for all groups; one-way ANOVA with Holm-Sidak's multiple comparisons test, WT-saline vs R59X-saline, $p < 0.0001$; R59X-saline vs R59X-memantine, $p < 0.0001$). (C) The duration of the longest grooming bout is significantly increased in saline-treated R59X mice in comparison to WT, and memantine also ameliorated this aspect of repetitive behavior ($n = 8$ for all groups; one-way ANOVA with Holm-Sidak's multiple

comparisons test, WT-saline vs R59X-saline, $p < 0.0001$; R59X-saline vs R59X-memantine, $p < 0.0001$). (D) On the dyadic social assay, saline-treated R59X mice spend significantly less time initiating social interaction with a novel stimulus mouse in comparison to WT. Memantine at 5 mg/kg resulted in a significant increase in time spent in social interaction ($n = 7$ for all groups; one-way ANOVA with Holm-Sidak's multiple comparisons test, WT-saline vs R59X-saline, $p = 0.0006$; R59X-saline vs R59X-memantine, $p = 0.027$). (E) For co-tested pairs of R59X and WT mice, the ratio of time spent in direct interaction was significantly reduced in saline-treated mice. Memantine normalized this ratio, indicating a differential effect of this drug on social interaction in WT and R59X mice ($n=7$ for all groups; unpaired t -test, $p = 0.0002$).

CHAPTER 4 – CDKL5 REGULATES THE ELABORATION OF THE DENDRITIC TREE IN ADULT MICE

Contributions: Sheng Tang led this study, with help from Katarina Pance, Nicolas Sarmiento, and Barbara Terzic for the analysis of data, and Zhaolan Zhou and Douglas Coulter for the review and interpretation of data. Yolanda Cui managed mouse colonies. Sheng Tang wrote this chapter with input from all authors.

Abstract

The formation and patterning of dendrites provide the structural basis of neural circuit development and are critical for proper brain function. A single pyramidal neuron has a dendritic tree that contains up to thousands of dendritic spines, which represent the primary sites of excitatory synapses. Although much is known about the processes that regulate dendritic outgrowth and synapse formation during early development, far less is understood about the processes that regulate neuronal morphology in the adult brain. Here, we show that the loss of cyclin-dependent kinase-like 5 (CDKL5) in mice leads to a dendritic arborization deficit that is not apparent during early postnatal development, but instead emerges in adulthood. Specifically, CDKL5-deficient mice fail to show a continued elaboration of the dendritic tree from the juvenile period through adulthood, in contrast to what is observed in wild type mice. Interestingly, this dendritic arborization deficit was not accompanied by a change in dendritic spine density. Together, our results support a novel role for CDKL5 in the elaboration and patterning of the dendritic tree in the adult mouse brain and provide an intriguing example of impaired dendritic stability in a model of CDKL5 deficiency disorder.

Introduction

In early development, the outgrowth and elaboration of dendritic trees are regulated by conserved genetic programs as well as activity-dependent signaling (Jan and Jan, 2010). During this period, the dendritic tree is highly dynamic, regulated by coordinated mechanisms involving transcription, translation, various signaling pathways, cytoskeleton formation, and the organization of organelles (Jan and Jan, 2010). As the animal reaches adulthood, the dendritic tree becomes a relatively stable structure with a defined size and complexity (Koleske, 2013). Interestingly, recent work has revealed that dendritic trees are also dynamically regulated in adulthood and shed light on the underlying mechanisms (Lin and Koleske, 2010; Warren et al., 2012). In addition, examples are emerging that show evidence of altered dendritic stability in disease models (Lin and Koleske, 2010), supporting the importance of the regulation of neuronal morphology in adulthood for proper brain function.

Cyclin-dependent kinase-like 5 (CDKL5) is a protein highly conserved in mammals, showing enriched expression in various cell populations of the brain, most prominently in the pyramidal neurons of the cortex and hippocampus (Zeisel et al., 2015). Interestingly, the expression of CDKL5 is also temporally regulated, showing significant upregulation in the first few postnatal weeks (Hector et al., 2016; Ricciardi et al., 2012; Zhu et al., 2013), mirroring the timeline of primary dendritic outgrowth and excitatory synaptogenesis at pyramidal neurons. Consistent with these findings, CDKL5-deficient mice have been found to have reduced dendritic complexity across various excitatory neuron populations (Amendola et al., 2014; Fuchs et al., 2014; Tang et al., 2017). For example, hippocampal CA1 neurons in *Cdkl5* knockout and conditional knockout mice show reduced dendritic complexity in adulthood (Amendola et al., 2014;

Tang et al., 2017). However, no study to date has examined neuronal morphology in CDKL5-deficient mice across development, and therefore it remains unknown whether the dendritic arborization phenotype is due to a defect in outgrowth, maintenance, or both. Interestingly, evidence suggests that CDKL5 protein levels remains elevated throughout adulthood, suggesting a role in the maintenance of neuronal structure and function.

Here, we investigate the morphology of hippocampal CA1 pyramidal neurons, *in vivo* and across development, in a mouse model of CDKL5 deficiency disorder (CDD). We find that both dendritic complexity and spine density are unaltered in juvenile CDKL5-deficient mice. In contrast, CDKL5-deficient mice show a robust reduction in dendritic complexity in adulthood, with no significant changes in spine density. Comparing dendritic morphology across development, we observe that CDKL5-deficient mice fail to show the continued elaboration of the dendritic tree in adulthood that is apparent in wild type mice. Taken together, our results suggest a novel role for CDKL5 in the regulation of elaboration of the dendritic tree during adulthood and highlight the importance of dendritic stability in a model of CDD.

Results

Reduced dendritic complexity in CDKL5-deficient mice in adulthood

To investigate neuronal morphology *in vivo*, we generated wild type and CDKL5-deficient (R59X, see Chapter 3) mice carrying the Thy1-GFP (line M) transgenic reporter allele (Feng et al., 2000). Previous work suggests that in mice, dendritic tree formation and patterning are highly dynamic processes prior to postnatal day (P) 21, with

subsequent stabilization of the dendritic tree throughout adulthood (Koleske, 2013).

Therefore, we examined dendritic complexity in pyramidal neurons of the hippocampal CA1 region at two different developmental time points, postnatal day (P) 21 and P140, corresponding approximately to juvenile and adult stages of mouse development.

In adult (P140) R59X mice, we discovered that CA1 pyramidal neurons exhibited significantly reduced dendritic branching at both the basal and proximal apical dendritic trees (Fig. 1A, C). In addition, total apical dendritic length was also significantly reduced (Fig. 1B, D). In contrast, in juvenile (P21) R59X mice, Sholl analysis did not reveal any significant differences compared to wild type littermates and total dendritic lengths of both apical and basal trees were unaltered in R59X mice (Fig. 2). These results suggest that a dendritic branching deficit in R59X mice emerges postnatally in a delayed manner, after the first three weeks of postnatal development.

Loss of CDKL5 limits dendritic arborization in adulthood

The emergence of a dendritic arborization deficit in adult CDKL5-deficient mice can be due to 1) an impairment in continued dendritic outgrowth and/or 2) impaired stability that leads dendritic retraction. To gain insight into these two potential underlying mechanisms, we compared the dendritic complexity of hippocampal CA1 neurons in wild type and R59X mice at both P21 and P140 time points (Fig. 3). Interestingly, we found that CA1 pyramidal neurons in wild type mice show continued elaboration of the dendritic tree from P21 to P140, particularly at the proximal apical tree, leading to an increase in dendritic complexity (Fig. 3A, C) as well as an increase in overall dendritic

length (Fig. 3B, D). In contrast, R59X mice failed to show an enhancement of either dendritic complexity or overall dendritic length from P21 to P140 (Fig. 3A-D).

Unaltered dendritic spine density in CDKL5-deficient mice

The alteration in dendritic complexity in R59X mice suggests that CDKL5 may play a critical role in the development and maintenance of neuronal morphology in adulthood. We additionally examined dendritic spine density at CA1 pyramidal neurons at the same developmental time points in R59X and wild type littermate mice. No significant changes in dendritic spine density were found in either the proximal apical, distal apical, or basal dendritic trees of CA1 pyramidal neurons (Fig. 4A-F). These results suggest that the dendritic arborization deficit in R59X mice is not accompanied by a change in spine density at either the juvenile or adult developmental stages. Further work, however, is necessary to characterize the morphologic parameters of dendritic spines in wild type and R59X mice.

Discussion

The elaboration of the dendritic tree of neurons relies upon an intricate genetic program as well as activity-dependent cues throughout development (Jan and Jan, 2010). Furthermore, the patterning and stability of the dendritic tree can be modulated throughout adulthood (Koleske, 2013). The finding that dendritic complexity is reduced specifically in R59X mice in adulthood suggests that CDKL5 may specifically regulate or maintain aspects of postnatal dendritic patterning and stability. Furthermore, in comparing juvenile and adult mice, we find that R59X mice fail to show a continued

elaboration of the dendritic tree in adulthood that is apparent in wild type controls. Taken together, our results suggest that CDKL5 plays a critical role in the outgrowth, branching, and/or stability of the dendritic tree during adulthood.

We previously discovered that mice lacking CDKL5 selectively in forebrain glutamatergic neurons (Nex-cKO) recapitulate the dendritic branching deficits at the proximal apical and basal dendritic trees of CA1 pyramidal neurons (Tang et al., 2017). This result suggests that CDKL5 regulates dendritic complexity in a glutamatergic neuron-autonomous manner. However, due to the widespread expression of Nex-Cre throughout the forebrain, sustained changes in neuronal network activity during postnatal development, as well as cell-autonomous mechanisms, can both contribute to the dendritic complexity deficit in Nex-cKO mice.

Dendritic spines represent the primary sites of excitatory synapses formed onto pyramidal neurons, and their density and morphology can yield information regarding the number and distribution of synapses (Nimchinsky et al., 2002). Dendritic spine pathology is a common finding across mouse models of neurodevelopmental disorders and even in human patients (Penzes et al., 2011). Our results show that juvenile and adult R59X mice do not exhibit significant changes in dendritic spine density at CA1 pyramidal neurons. This result stands in contrast to our previous findings in Nex-cKO mice, which exhibited increased spine density (Tang et al., 2017). Further investigation is necessary to determine whether spine morphology is altered R59X mice at different points in development, which could reflect an underlying change in excitatory synaptic function. In addition, although our studies are thus far limited to hippocampal CA1 pyramidal neurons, CDKL5 is known to also be expressed in cortical regions (Wang et al., 2012). Given that distinct mechanisms may regulate cortical and hippocampal pyramidal neuron

morphology (Attardo et al., 2015), future studies should investigate the possibility the CDKL5 regulates morphology in a brain region-specific manner.

In order to determine the extent to which CDKL5 regulates neuronal morphology in a cell-autonomous manner, an approach that achieves sparse knockout of CDKL5 *in vivo* is necessary. We are currently generating mice carrying the Slick-V transgenic allele (Young et al., 2008) and a conditional *Cdkl5* knockout allele, which will allow temporally-inducible, sparse knockout of CDKL5 in various brain regions. Together with our previous findings in R59X and Nex-cKO mice, the studies in Slick-V conditional knockout mice will allow us to differentiate the pyramidal neuron-autonomous and network activity-dependent effects of CDKL5 loss on neuronal morphology. Additionally, by inducing Cre activity at distinct time points during development, we can further dissect the roles of CDKL5 in early and late postnatal development.

Materials and Methods

Wild type and R59X littermate mice carrying Thy1-GFP (genotypes: R59X/y; Thy1-GFP and +/y; Thy1-GFP) at the ages of P21 and P140 were used for neuronal morphology experiments. The methods used in this chapter are identical to those used to investigate neuronal morphology in Nex-cKO mice (Chapter 2). Additionally, we thank Dr. Mollie Meffert and her lab at the Johns Hopkins School of Medicine for sharing the Slick-V transgenic mouse line (Young et al., 2008) with us.

Figures

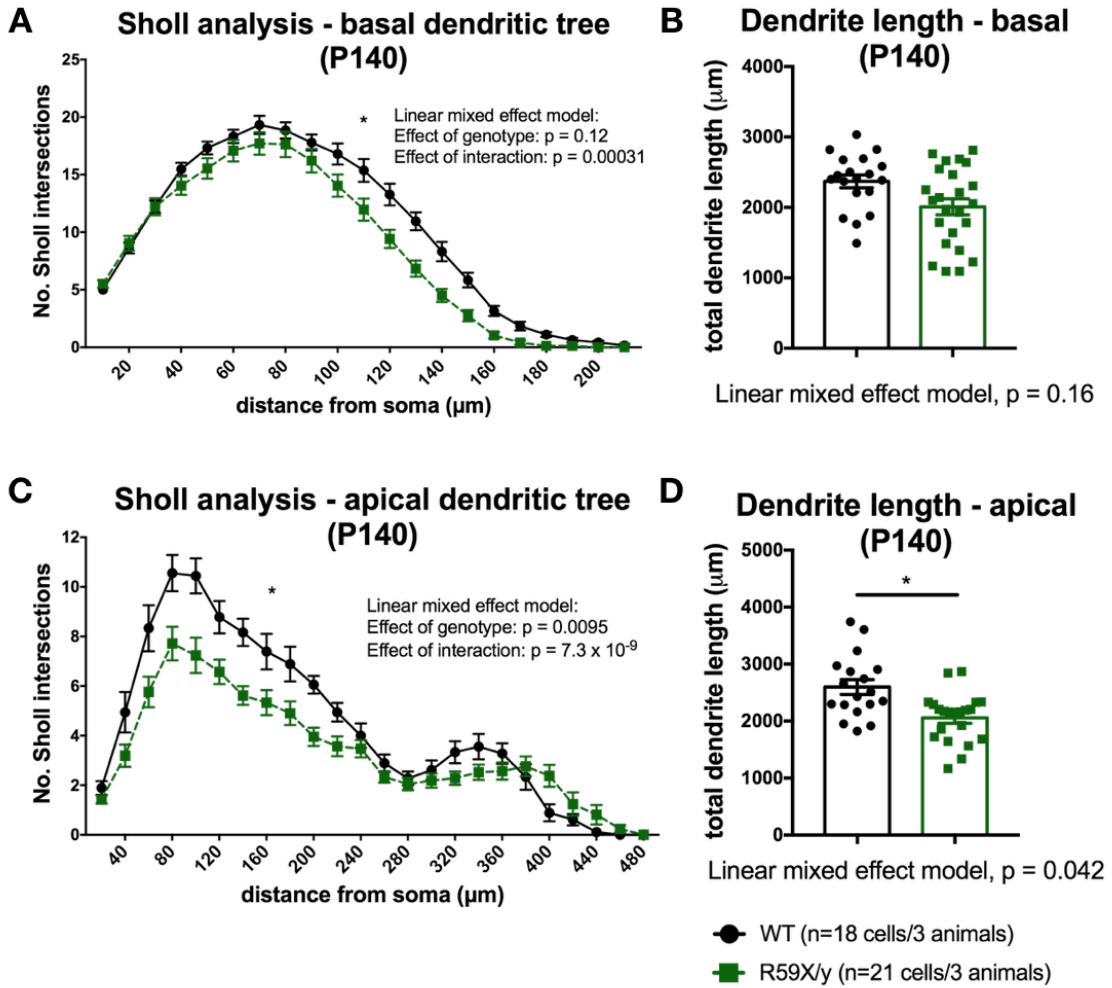


Figure 1. Reduced dendritic complexity of hippocampal CA1 pyramidal neurons in adult CDKL5 R59X mice.

(A) Reduced complexity of the basal dendritic tree in R59X mice. (B) Total basal dendrite length was not significantly altered. (C) Reduced complexity of the proximal apical dendritic tree in R59X mice. (D) Total apical dendrite length was also significantly reduced in R59X mice (n=18 cells/3 mice, wild type; n=21 cells/3 mice, R59X)

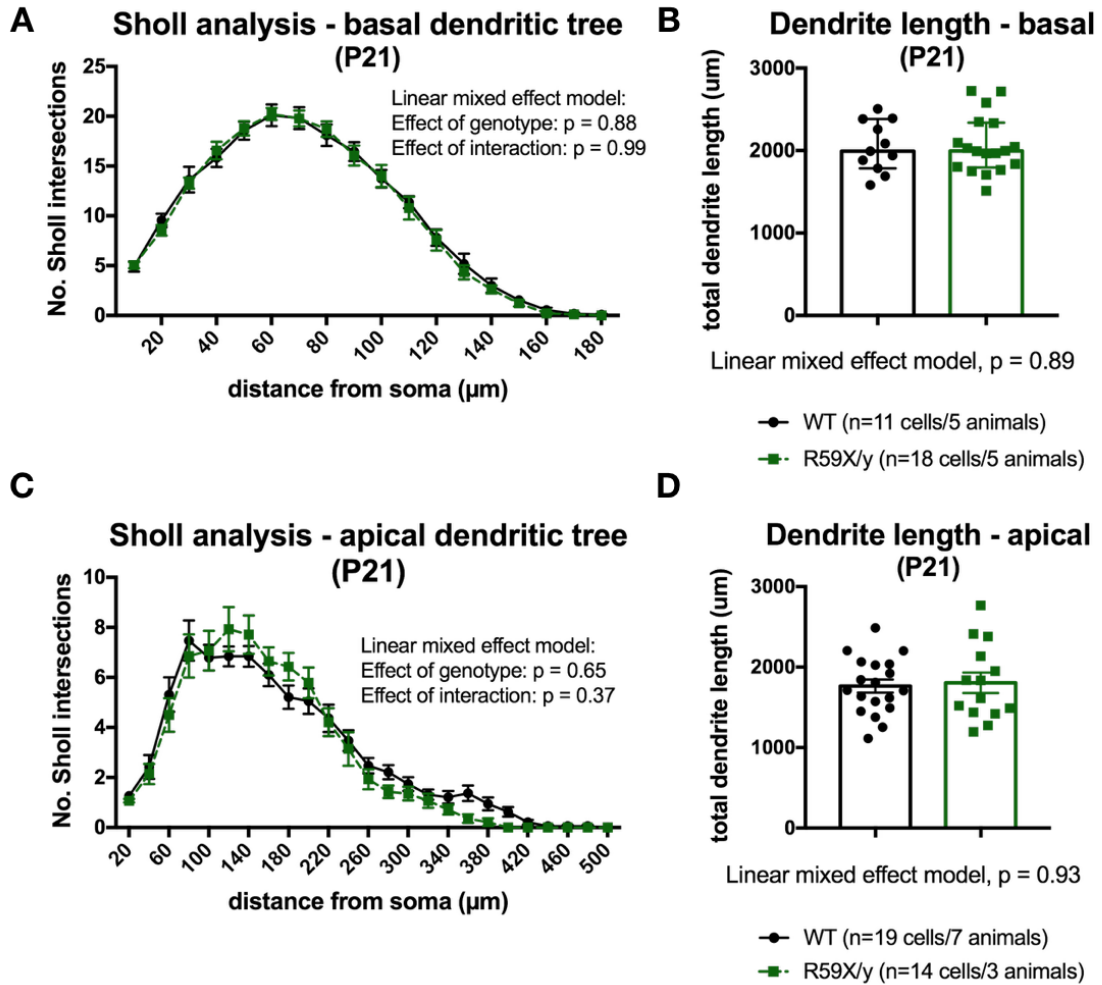


Figure 2. Unaltered dendritic complexity of hippocampal CA1 pyramidal neurons in juvenile CDKL5 R59X mice.

(A-B) Unaltered complexity and total length of the basal dendritic tree in R59X mice (n=11 cells/5 mice, wild type; n=18 cells/5 mice, R59X). (C-D) Unaltered complexity and total length of the apical dendritic tree in R59X mice (n=19 cells/7 mice, wild type; n=14 cells/3 mice, R59X)

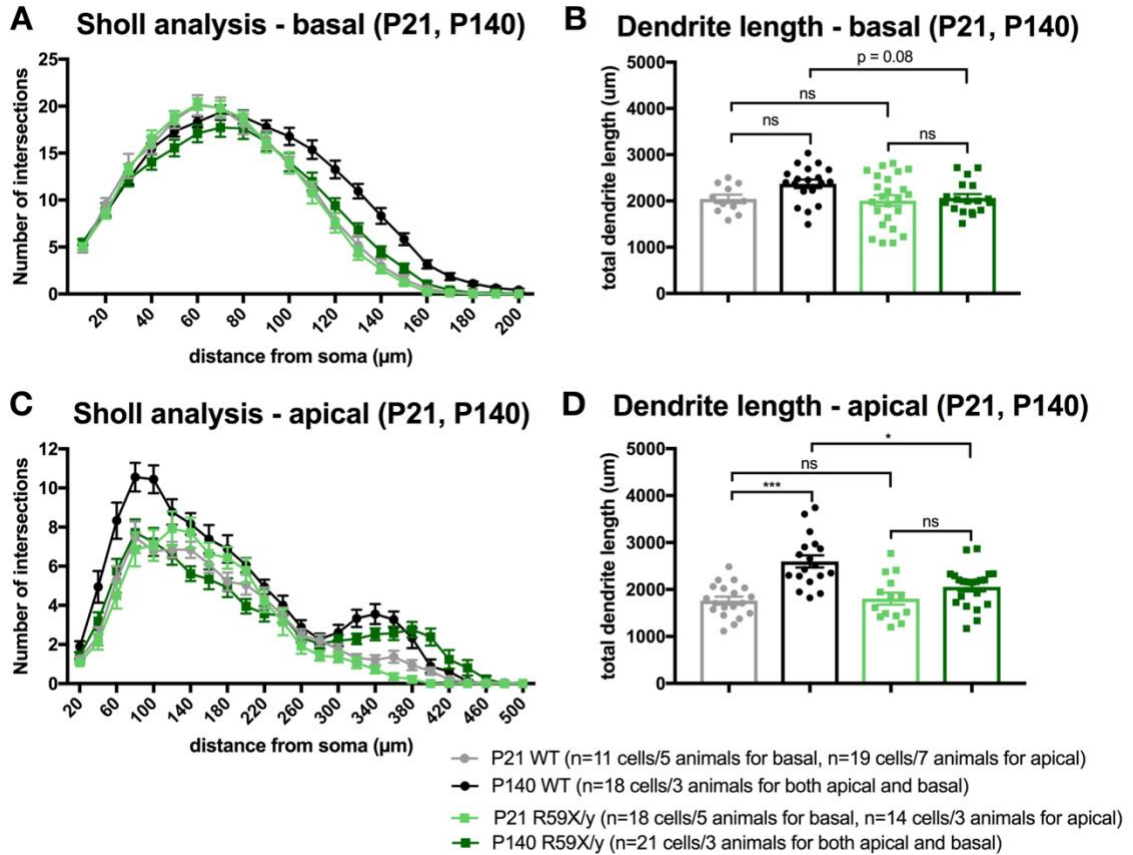


Figure 3. Loss of CDKL5 limits dendritic arborization in adulthood.

(A, C) Comparison of the Sholl analyses of the basal and apical trees of CA1 pyramidal neurons across development in WT and R59X mice. Note the continued increase in dendritic complexity of WT mice from P21 to P140, evident by the increase in number of intersections, and the lack of this increase in R59X mice. (B, D) Comparison of total dendrite length of the basal and apical trees of CA1 pyramidal neurons across development in WT and R59X mice. Note the significant increase in apical dendritic length in WT mice from P21 to P140 and the lack of this increase in R59X mice. Respective sample sizes are indicated in the figure legend.

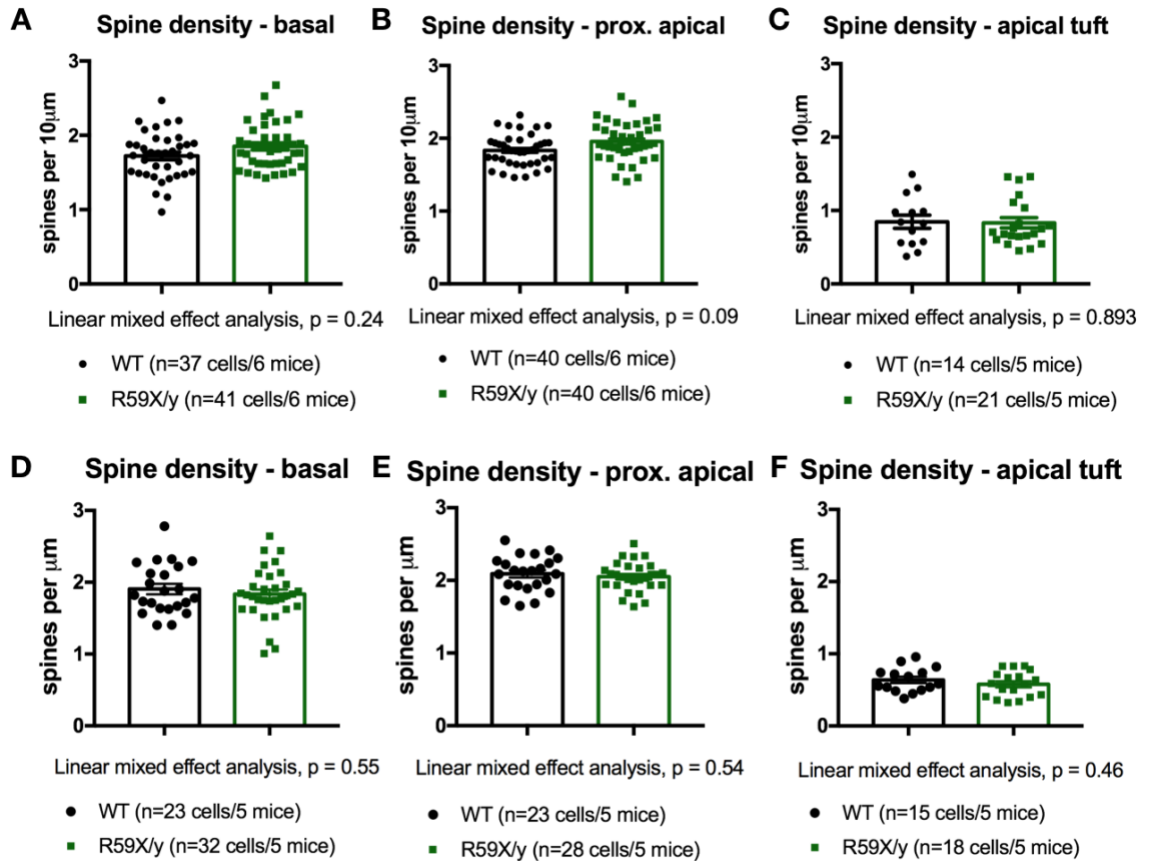


Figure 4. Unaltered spine density of hippocampal CA1 pyramidal neurons in juvenile and adult CDKL5 R59X mice.

(A-C) Unaltered density of dendritic spines in juvenile (P21) R59X mice. (D-F) Unaltered density of dendritic spines in adult (P14) R59X mice. Respective sample sizes are indicated in each figure.

CHAPTER 5 – EXTENDED DISCUSSION AND FUTURE DIRECTIONS

Cellular Origins of CDKL5 Deficiency Disorder-Related Phenotypes

The findings presented in this dissertation show that most of the behavioral phenotypes in *Cdkl5* constitutive knockout (KO) mice “segregate” in *Cdkl5* conditional knockout (cKO) mice, such that impaired learning and memory is selectively recapitulated in Nex-cKO mice and autistic-like features are selectively recapitulated in Dlx-cKO mice. These results suggest that CDKL5 function in each of these forebrain neuronal populations is necessary for the development of proper learning and memory and social behaviors, respectively. Interestingly, several important phenotypes of KO mice are not recapitulated in either Nex-cKO and Dlx-cKO mice; these include alterations in anxiety-related behavior, locomotion, and motor coordination. These phenotypes may depend on the loss of CDKL5 in cell types and brain regions not covered by either the Nex-Cre and Dlx5/6-Cre drivers alone. Moreover, future studies can conduct a side-by-side comparison of Nex-cKO, Dlx-cKO, and KO mice. This would allow a side-by-side comparison of phenotypic severity across these mouse lines, which may reveal subtle differences. Furthermore, CDKL5 may function in both populations, in a synergistic manner, to regulate aspects of learning and memory, social behavior, and stereotypic behavior.

Epilepsy in CDKL5 Deficiency Disorder

Early-onset, treatment-refractory epilepsy is a central feature of CDKL5 deficiency disorder (CDD) in humans. However, spontaneous seizures have not been observed in *Cdkl5* KO and cKO mice despite EEG studies at multiple ages conducted by

multiple laboratories. Nonetheless, these results do not rule out the possibility that *Cdkl5* KO and cKO mice have subclinical epilepsy, particularly at extreme ends of the age spectrum (infancy/juvenile period and old age) when EEG monitoring and other studies may not be feasible or practical. Furthermore, whereas human CDKL5-deficient patients nearly universally exhibit epilepsy, a lower prevalence in mice may preclude detection without large-scale studies.

Various chemoconvulsants and seizure induction paradigms have been used to attempt to assess seizure threshold in *Cdkl5* KO and cKO mice. In this regard, there are a few promising results, including the enhanced susceptibility of KO mice to the ionotropic glutamate receptor agonist N-methyl-D-aspartate (NMDA). However, other seizure paradigms have not consistently revealed a reduction in seizure threshold. At least in mice, it appears that there may be distinct pro-epileptic and anti-epileptic mechanisms underlying CDD. This finding is corroborated at the synaptic, circuit, and network levels, where there are both results suggesting hyper-excitability and hypo-excitability. Therefore, it may be appropriate to consider additional hypotheses about the mechanisms underlying epilepsy in CDD. For example, depolarizing inhibition and network hyper-synchrony are alternative, pro-epileptic mechanisms that may enhance excitatory drive in mouse models of CDD.

Phenotypic Heterogeneity in CDKL5 Deficiency Disorder

There is significant phenotypic heterogeneity in human CDD. Much of this has been attributed to variable X-chromosome inactivation in female patients, who are heterozygous for mutations in *CDKL5*. Surprisingly, significant phenotypic variability is present even in genetically inbred, male hemizygous mice carrying *Cdkl5* mutations.

Although phenotypic variability in *Cdkl5* KO mice has not been quantitatively analyzed, it has raised the possibility that there are multiple developmental trajectories associated with CDD leading to distinct phenotypic outcomes. In addition to the specific pattern of CDKL5 loss, these trajectories may depend on genetic background, parental, prenatal, or perinatal factors, and they may additionally be modulated by environment throughout postnatal life. Our studies in mice have revealed different disease mechanisms that contribute to distinct phenotypes in CDD, expanding the opportunities for mechanism-based therapeutic development for CDD patients.

CDKL5 Deficiency Disorder and Interspecies Differences

To date, mice have been the primary animal models used for investigation of the mechanisms underlying CDD. In addition to confirming the genetic etiology of CDD, mouse models have offered important insights into how CDKL5 impacts neuronal morphology, synaptic transmission, circuit architecture, and network activity. The translational value of these findings is supported by the high degree of conservation in primary sequence of the CDKL5 protein between mice and humans, as well as the similarities in many of the classic cell types and both local and long-range circuit architecture in the brain (Miller et al., 2014; Oh et al., 2014). In this respect, mice will continue to provide key insights into the pathogenic mechanisms underlying CDD.

There are, however, also significant differences between human and mouse brains that may account for the absence of key features in mouse models of CDD, such as epilepsy. CDKL5 expression is enriched in forebrain regions, most prominently in cortical glutamatergic neurons and GABAergic interneurons. Given that the cortex is also the most highly evolved region of the human brain and thought to account for many of

the unique behaviors and capabilities of the human species (Sousa et al., 2017), it is perhaps not surprising that network-level phenotypes such as epilepsy are not recapitulated in mice, which unlike humans are a lissencephalic species. Furthermore, significant differences exist between the transcriptional landscapes of the human and mouse brains during development, leading to differences in cell migration, laminar organization, myelination, synaptogenesis, and adult neurogenesis (Silbereis et al., 2016). Despite these differences, CDKL5 likely plays conserved roles in the regulation of synaptic and circuit function in many brain regions in humans and mice. Therefore, investigations into how CDKL5 modulates circuit excitability and plasticity will likely yield important insights into the mechanisms that generate epilepsy, impaired cognition, and other neurologic deficits in CDD, uncovering novel therapeutic avenues for the treatment of CDD.

BIBLIOGRAPHY

- Amendola, E., Zhan, Y., Mattucci, C., Castroflorio, E., Calcagno, E., Fuchs, C., Lonetti, G., Silingardi, D., Vyssotski, A.L., Farley, D., et al. (2014). Mapping pathological phenotypes in a mouse model of CDKL5 disorder. *PLoS ONE* 9, e91613–12.
- Ang, C.W., Carlson, G.C., and Coulter, D.A. (2005). Hippocampal CA1 circuitry dynamically gates direct cortical inputs preferentially at theta frequencies. *J. Neurosci.* 25, 9567–9580.
- Antić, S., and Zecević, D. (1995). Optical signals from neurons with internally applied voltage-sensitive dyes. *J. Neurosci.* 15, 1392–1405.
- Arellano, J.I., Benavides-Piccione, R., DeFelipe, J., and Yuste, R. (2007). Ultrastructure of dendritic spines: correlation between synaptic and spine morphologies. *Front. Neurosci.* 1, 131–143.
- Attardo, A., Fitzgerald, J.E., and Schnitzer, M.J. (2015). Impermanence of dendritic spines in live adult CA1 hippocampus. *Nature* 523, 592–596.
- Backus, A.R., Schoffelen, J.-M., Szebényi, S., Hanslmayr, S., and Doeller, C.F. (2016). Hippocampal-Prefrontal Theta Oscillations Support Memory Integration. *Curr. Biol.* 26, 450–457.
- Bahi-Buisson, N., and Bienvenu, T. (2012). CDKL5-Related Disorders: From Clinical Description to Molecular Genetics. 2, 137–152.
- Bahi-Buisson, N., Nectoux, J., Rosas-Vargas, H., Milh, M., Boddaert, N., Girard, B., Cances, C., Ville, D., Afejar, A., Rio, M., et al. (2008). Key clinical features to identify girls with CDKL5 mutations. *Brain* 131, 2647–2661.
- Bateup, H.S., Johnson, C.A., Deneffrio, C.L., Saulnier, J.L., Kornacker, K., and Sabatini, B.L. (2013). Excitatory/inhibitory synaptic imbalance leads to hippocampal hyperexcitability in mouse models of tuberous sclerosis. *Neuron* 78, 510–522.
- Bayés, A., Collins, M.O., Croning, M.D.R., van de Lagemaat, L.N., Choudhary, J.S., and Grant, S.G.N. (2012). Comparative Study of Human and Mouse Postsynaptic Proteomes Finds High Compositional Conservation and Abundance Differences for Key Synaptic Proteins. *PLoS ONE* 7, e46683.
- Bertani, I., Rusconi, L., Bolognese, F., Forlani, G., Conca, B., De Monte, L., Badaracco, G., Landsberger, N., and Kilstrup-Nielsen, C. (2006). Functional consequences of mutations in CDKL5, an X-linked gene involved in infantile spasms and mental retardation. *J. Biol. Chem.* 281, 32048–32056.

- Bloss, E.B., Cembrowski, M.S., Karsh, B., Colonell, J., Fetter, R.D., and Spruston, N. (2016). Structured Dendritic Inhibition Supports Branch-Selective Integration in CA1 Pyramidal Cells. *Neuron* 89, 1016–1030.
- Carlson, G.C., and Coulter, D.A. (2008). In vitro functional imaging in brain slices using fast voltage-sensitive dye imaging combined with whole-cell patch recording. *Nat Protoc* 3, 249–255.
- Cembrowski, M.S., Wang, L., Sugino, K., Shields, B.C., and Spruston, N. (2016). Hipposeq: a comprehensive RNA-seq database of gene expression in hippocampal principal neurons. *Elife* 5, e14997.
- Chao, H.-T., Chen, H., Samaco, R.C., Xue, M., Chahrour, M., Yoo, J., Neul, J.L., Gong, S., Lu, H.-C., Heintz, N., et al. (2010). Dysfunction in GABA signalling mediates autism-like stereotypies and Rett syndrome phenotypes. *Nature* 468, 263–269.
- Chen, Q., Zhu, Y.-C., Yu, J., Miao, S., Zheng, J., Xu, L., Zhou, Y., Li, D., Zhang, C., Tao, J., et al. (2010). CDKL5, a protein associated with rett syndrome, regulates neuronal morphogenesis via Rac1 signaling. *J. Neurosci.* 30, 12777–12786.
- Chung, W., Choi, S.Y., Lee, E., Park, H., Kang, J., Park, H., Choi, Y., Lee, D., Park, S.-G., Kim, R., et al. (2015). Social deficits in IRSp53 mutant mice improved by NMDAR and mGluR5 suppression. *Nat Neurosci* 18, 435–443.
- Colgin, L.L. (2016). Rhythms of the hippocampal network. *Nat Rev Neurosci* 17, 239–249.
- Coulter, D.A., Yue, C., Ang, C.W., Weissinger, F., Goldberg, E., Hsu, F.-C., Carlson, G.C., and Takano, H. (2011). Hippocampal microcircuit dynamics probed using optical imaging approaches. *J. Physiol.* 589, 1893–1903.
- Deacon, R.M.J. (2006). Assessing nest building in mice. *Nat Protoc* 1, 1117–1119.
- DeNardo, L.A., de Wit, J., Otto-Hitt, S., and Ghosh, A. (2012). NGL-2 Regulates Input-Specific Synapse Development in CA1 Pyramidal Neurons. *Neuron* 76, 762–775.
- Dengler, C.G., and Coulter, D.A. (2016). Normal and epilepsy-associated pathologic function of the dentate gyrus. *Prog. Brain Res.* 226, 155–178.
- Etherton, M.R., Blaiss, C.A., Powell, C.M., and Südhof, T.C. (2009). Mouse neurexin-1alpha deletion causes correlated electrophysiological and behavioral changes consistent with cognitive impairments. *106*, 17998–18003.
- Etherton, M.R., Tabuchi, K., Sharma, M., Ko, J., and Südhof, T.C. (2011a). An autism-associated point mutation in the neuroligin cytoplasmic tail selectively impairs AMPA receptor-mediated synaptic transmission in hippocampus. *Embo J.* 30, 2908–2919.

- Etherton, M., Földy, C., Sharma, M., Tabuchi, K., Liu, X., Shamloo, M., Malenka, R.C., and Südhof, T.C. (2011b). Autism-linked neuroligin-3 R451C mutation differentially alters hippocampal and cortical synaptic function. *108*, 13764–13769.
- Evans, J.C., Archer, H.L., Colley, J.P., Ravn, K., Nielsen, J.B., Kerr, A., Williams, E., Christodoulou, J., Gécz, J., Jardine, P.E., et al. (2005). Early onset seizures and Rett-like features associated with mutations in CDKL5. *Eur. J. Hum. Genet.* *13*, 1113–1120.
- Fairless, A.H., Katz, J.M., Vijayvargiya, N., Dow, H.C., Kreibich, A.S., Berrettini, W.H., Abel, T., and Brodtkin, E.S. (2013). Development of home cage social behaviors in BALB/cJ vs. C57BL/6J mice. *Behav. Brain Res.* *237*, 338–347.
- Fehr, S., Downs, J., Ho, G., de Klerk, N., Forbes, D., Christodoulou, J., Williams, S., and Leonard, H. (2016a). Functional abilities in children and adults with the CDKL5 disorder. *Am. J. Med. Genet.* 1–10.
- Fehr, S., Leonard, H., Ho, G., Williams, S., de Klerk, N., Forbes, D., Christodoulou, J., and Downs, J. (2015). There is variability in the attainment of developmental milestones in the CDKL5 disorder. *J Neurodev Disord* *7*, 2–13.
- Fehr, S., Wilson, M., Downs, J., Williams, S., Murgia, A., Sartori, S., Vecchi, M., Ho, G., Polli, R., Psoni, S., et al. (2012). The CDKL5 disorder is an independent clinical entity associated with early-onset encephalopathy. *Eur. J. Hum. Genet.* *21*, 266–273.
- Fehr, S., Wong, K., Chin, R., Williams, S., de Klerk, N., Forbes, D., Krishnaraj, R., Christodoulou, J., Downs, J., and Leonard, H. (2016b). Seizure variables and their relationship to genotype and functional abilities in the CDKL5 disorder. *Neurology* *87*, 2206–2213.
- Feng, G., Mellor, R.H., Bernstein, M., Keller-Peck, C., Nguyen, Q.T., Wallace, M., Nerbonne, J.M., Lichtman, J.W., and Sanes, J.R. (2000). Imaging Neuronal Subsets in Transgenic Mice Expressing Multiple Spectral Variants of GFP. *Neuron* *28*, 41–51.
- Figueiredo, C.P., Clarke, J.R., Ledo, J.H., Ribeiro, F.C., Costa, C.V., Melo, H.M., Mota-Sales, A.P., Saraiva, L.M., Klein, W.L., Sebollela, A., et al. (2013). Memantine rescues transient cognitive impairment caused by high-molecular-weight $\alpha\beta$ oligomers but not the persistent impairment induced by low-molecular-weight oligomers. *J. Neurosci.* *33*, 9626–9634.
- Flavell, S.W., Cowan, C.W., Kim, T.-K., Greer, P.L., Lin, Y., Paradis, S., Griffith, E.C., Hu, L.S., Chen, C., and Greenberg, M.E. (2006). Activity-dependent regulation of MEF2 transcription factors suppresses excitatory synapse number. *Science* *311*, 1008–1012.
- Fuchs, C., Rimondini, R., Viggiano, R., Trazzi, S., De Franceschi, M., Bartesaghi, R., and Ciani, E. (2015). Inhibition of GSK3 β rescues hippocampal development and learning in a mouse model of CDKL5 disorder. *Neurobiol. Dis.* *82*, 298–310.
- Fuchs, C., Trazzi, S., Torricella, R., Viggiano, R., De Franceschi, M., Amendola, E., Gross, C., Calzà, L., Bartesaghi, R., and Ciani, E. (2014). Loss of CDKL5 impairs

- survival and dendritic growth of newborn neurons by altering AKT/GSK-3 β signaling. *Neurobiol. Dis.* 70, 53–68.
- Goebbels, S., Bormuth, I., Bode, U., Hermanson, O., Schwab, M.H., and Nave, K.-A. (2006). Genetic targeting of principal neurons in neocortex and hippocampus of NEX-Cre mice. *Genesis* 44, 611–621.
- Goebel, D.J., and Poosch, M.S. (1999). NMDA receptor subunit gene expression in the rat brain: a quantitative analysis of endogenous mRNA levels of NR1Com, NR2A, NR2B, NR2C, NR2D and NR3A. *Brain Res. Mol. Brain Res.* 69, 164–170.
- Goldberg, E.M., and Coulter, D.A. (2013). Mechanisms of epileptogenesis: a convergence on neural circuit dysfunction. *Nat Rev Neurosci* 14, 337–349.
- Grosso, S., Brogna, A., Bazzotti, S., Renieri, A., Morgese, G., and Balestri, P. (2007). Seizures and electroencephalographic findings in CDKL5 mutations: case report and review. *Brain Dev.* 29, 239–242.
- Habib-E-Rasul Mullah, S., Komuro, R., Yan, P., Hayashi, S., Inaji, M., Momose-Sato, Y., Loew, L.M., and Sato, K. (2013). Evaluation of Voltage-Sensitive Fluorescence Dyes for Monitoring Neuronal Activity in the Embryonic Central Nervous System. *J Membrane Biol* 246, 679–688.
- Hagebeuk, E.E.O., van den Bossche, R.A.S., and de Weerd, A.W. (2013). Respiratory and sleep disorders in female children with atypical Rett syndrome caused by mutations in the CDKL5 gene. *Dev Med Child Neurol* 55, 480–484.
- Hanefeld, F. (1985). The clinical pattern of the Rett syndrome. *Brain Dev.* 7, 320–325.
- Hao, S., Hao, S., Tang, B., Wu, Z., Wu, Z., Ure, K., Ure, K., Sun, Y., Sun, Y., Tao, H., et al. (2015). Forniceal deep brain stimulation rescues hippocampal memory in Rett syndrome mice. *Nature* 526, 430–434.
- Harris, K.M., and Stevens, J.K. (1989). Dendritic spines of CA1 pyramidal cells in the rat hippocampus: serial electron microscopy with reference to their biophysical characteristics. *J. Neurosci.* 9, 2982–2997.
- Harris, K.D., and Mrcic-Flogel, T.D. (2013). Cortical connectivity and sensory coding. *Nature* 503, 51–58.
- Hector, R.D., Dando, O., Landsberger, N., Kilstrup-Nielsen, C., Kind, P.C., Bailey, M.E.S., and Cobb, S.R. (2016). Characterisation of CDKL5 Transcript Isoforms in Human and Mouse. *PLoS ONE* 11, e0157758–22.
- Hector, R.D., Kalscheuer, V.M., Hennig, F., Leonard, H., Downs, J., Clarke, A., Benke, T.A., Armstrong, J., Pineda, M., Bailey, M.E.S., et al. (2017). CDKL5 variants: Improving our understanding of a rare neurologic disorder. *Neurol Genet* 3, e200.

- Hébert, J.M., and Fishell, G. (2008). The genetics of early telencephalon patterning: some assembly required. *Nat Rev Neurosci* 9, 678–685.
- Jan, Y.-N., and Jan, L.Y. (2010). Branching out: mechanisms of dendritic arborization. *Nat Rev Neurosci* 11, 316–328.
- Jhang, C.-L., Huang, T.-N., Hsueh, Y.-P., and Liao, W. (2017). Mice lacking cyclin-dependent kinase-like 5 manifest autistic and ADHD-like behaviors. *Hum. Mol. Genet.* 26, 3922–3934.
- Johnson, B.S., Zhao, Y.-T., Fasolino, M., Lamonica, J.M., Kim, Y.J., Georgakilas, G., Wood, K.H., Bu, D., Cui, Y., Goffin, D., et al. (2017). Biotin tagging of MeCP2 in mice reveals contextual insights into the Rett syndrome transcriptome. *Nat Med* 23, 1203–1214.
- Joy, R.M., and Albertson, T.E. (1993). NMDA receptors have a dominant role in population spike-paired pulse facilitation in the dentate gyrus of urethane-anesthetized rats. *Brain Res.* 604, 273–282.
- Judson, M.C., Wallace, M.L., Sidorov, M.S., Burette, A.C., Bin Gu, van Woerden, G.M., King, I.F., Han, J.E., Zylka, M.J., Elgersma, Y., et al. (2016). GABAergic Neuron-Specific Loss of Ube3a Causes Angelman Syndrome-Like EEG Abnormalities and Enhances Seizure Susceptibility. *Neuron* 90, 1–15.
- Kalscheuer, V.M., Tao, J., Donnelly, A., Hollway, G., Schwinger, E., Kübart, S., Menzel, C., Hoeltzenbein, M., Tommerup, N., Eyre, H., et al. (2003). Disruption of the serine/threonine kinase 9 gene causes severe X-linked infantile spasms and mental retardation. *Am. J. Hum. Genet.* 72, 1401–1411.
- Kameshita, I., Sekiguchi, M., Hamasaki, D., Sugiyama, Y., Hatano, N., Suetake, I., Tajima, S., and Sueyoshi, N. (2008). Cyclin-dependent kinase-like 5 binds and phosphorylates DNA methyltransferase 1. *Biochem. Biophys. Res. Commun.* 377, 1162–1167.
- Kang, H.J., Kawasaki, Y.I., Cheng, F., Zhu, Y., Xu, X., Li, M., Sousa, A.M.M., Pletikos, M., Meyer, K.A., Sedmak, G., et al. (2011). Spatio-temporal transcriptome of the human brain. *Nature* 478, 483–489.
- Kang, J., and Kim, E. (2015). Suppression of NMDA receptor function in mice prenatally exposed to valproic acid improves social deficits and repetitive behaviors. *Front Mol Neurosci* 8, 17.
- Kepecs, A., and Fishell, G. (2014). Interneuron cell types are fit to function. *Nature* 505, 318–326.
- Kilstrup-Nielsen, C., Rusconi, L., La Montanara, P., Ciceri, D., Bergo, A., Bedogni, F., and Landsberger, N. (2012). What we know and would like to know about CDKL5 and its involvement in epileptic encephalopathy. *Neural Plast.* 2012, 728267–11.

- Klein, K.M., Yendle, S.C., Harvey, A.S., Antony, J.H., Wallace, G., Bienvenu, T., and Scheffer, I.E. (2011). A distinctive seizure type in patients with CDKL5 mutations: Hypermotor-tonic-spasms sequence. *Neurology* 76, 1436–1438.
- Koleske, A.J. (2013). Molecular mechanisms of dendrite stability. *Nat Rev Neurosci* 14, 536–550.
- Krey, J.F., Paşca, S.P., Shcheglovitov, A., Yazawa, M., Schwemberger, R., Rasmuson, R., and Dolmetsch, R.E. (2013). Timothy syndrome is associated with activity-dependent dendritic retraction in rodent and human neurons. *Nat Neurosci* 16, 201–209.
- La Montanara, P., Rusconi, L., Locarno, A., Forti, L., Barbiero, I., Tramarin, M., Chandola, C., Kilstrup-Nielsen, C., and Landsberger, N. (2015). Synaptic synthesis, dephosphorylation, and degradation: a novel paradigm for an activity-dependent neuronal control of CDKL5. *J. Biol. Chem.* 290, 4512–4527.
- Lee, E., Lee, J., and Kim, E. (2017). Excitation/Inhibition Imbalance in Animal Models of Autism Spectrum Disorders. *Biol. Psychiatry* 81, 838–847.
- Lenth, R.V. (2016). Least-Squares Means: The RPackage lsmeans. *J. Stat. Soft.* 69, 1–33.
- Lin, C., Franco, B., and Rosner, M.R. (2005). CDKL5/Stk9 kinase inactivation is associated with neuronal developmental disorders. *Hum. Mol. Genet.* 14, 3775–3786.
- Lin, Y.-C., and Koleske, A.J. (2010). Mechanisms of synapse and dendrite maintenance and their disruption in psychiatric and neurodegenerative disorders. *Annu. Rev. Neurosci.* 33, 349–378.
- Lu, H., Ash, R.T., He, L., Kee, S.E., Wang, W., Yu, D., Hao, S., Meng, X., Ure, K., Ure, K., et al. (2016). Loss and Gain of MeCP2 Cause Similar Hippocampal Circuit Dysfunction that Is Rescued by Deep Brain Stimulation in a Rett Syndrome Mouse Model. *Neuron* 91, 739–747.
- Luikart, B.W., Schnell, E., Washburn, E.K., Bensen, A.L., Tovar, K.R., and Westbrook, G.L. (2011). Pten knockdown in vivo increases excitatory drive onto dentate granule cells. *J. Neurosci.* 31, 4345–4354.
- Mangatt, M., Wong, K., Anderson, B., Epstein, A., Hodgetts, S., Leonard, H., and Downs, J. (2016). Prevalence and onset of comorbidities in the CDKL5 disorder differ from Rett syndrome. *Orphanet J Rare Dis* 11, 39.
- Manning, G., Whyte, D.B., Martinez, R., Hunter, T., and Sudarsanam, S. (2002). The protein kinase complement of the human genome. *Science* 298, 1912–1934.
- Mari, F., Azimonti, S., Bertani, I., Bolognese, F., Colombo, E., Caselli, R., Scala, E., Longo, I., Grosso, S., Pescucci, C., et al. (2005). CDKL5 belongs to the same molecular pathway of MeCP2 and it is responsible for the early-onset seizure variant of Rett syndrome. *Hum. Mol. Genet.* 14, 1935–1946.

- Melani, F., Mei, D., Pisano, T., Savasta, S., Franzoni, E., Ferrari, A.R., Marini, C., and Guerrini, R. (2011). CDKL5 gene-related epileptic encephalopathy: electroclinical findings in the first year of life. *Dev Med Child Neurol* 53, 354–360.
- Mertz, J., Tan, H., Pagala, V., Bai, B., Chen, P.-C., Li, Y., Cho, J.-H., Shaw, T., Wang, X., and Peng, J. (2015). Sequential Elution Interactome Analysis of the Mind Bomb 1 Ubiquitin Ligase Reveals a Novel Role in Dendritic Spine Outgrowth. *Mol. Cell Proteomics* 14, 1898–1910.
- Miller, J.A., Ding, S.-L., Sunkin, S.M., Smith, K.A., Ng, L., Szafer, A., Ebbert, A., Riley, Z.L., Royall, J.J., Aiona, K., et al. (2014). Transcriptional landscape of the prenatal human brain. *Nature* 508, 199–206.
- Mirzaa, G.M., Paciorkowski, A.R., Marsh, E.D., Berry-Kravis, E.M., Medne, L., Alkhateeb, A., Grix, A., Wirrell, E.C., Powell, B.R., Nickels, K.C., et al. (2013). CDKL5 and ARX mutations in males with early-onset epilepsy. *Pediatr. Neurol.* 48, 367–377.
- Monory, K., Massa, F., Egertová, M., Eder, M., Blaudzun, H., Westenbroek, R., Kelsch, W., Jacob, W., Marsch, R., Ekker, M., et al. (2006). The Endocannabinoid System Controls Key Epileptogenic Circuits in the Hippocampus. *Neuron* 51, 455–466.
- Müller, A., Helbig, I., Jansen, C., Bast, T., Guerrini, R., Jahn, J., Muhle, H., Auvin, S., Korenke, G.C., Philip, S., et al. (2016). Retrospective evaluation of low long-term efficacy of antiepileptic drugs and ketogenic diet in 39 patients with CDKL5-related epilepsy. *Eur. J. Paediatr. Neurol.* 20, 147–151.
- Nawaz, M.S., Giarda, E., Bedogni, F., La Montanara, P., Ricciardi, S., Ciceri, D., Alberio, T., Landsberger, N., Rusconi, L., and Kilstrup-Nielsen, C. (2016). CDKL5 and Shootin1 Interact and Concur in Regulating Neuronal Polarization. *PLoS ONE* 11, e0148634.
- Nelson, S.B., and Valakh, V. (2015). Excitatory/Inhibitory Balance and Circuit Homeostasis in Autism Spectrum Disorders. *Neuron* 87, 684–698.
- Nimchinsky, E.A., Sabatini, B.L., and Svoboda, K. (2002). Structure and Function of Dendritic Spines. *Annu. Rev. Physiol.* 64, 313–353.
- Oh, S.W., Harris, J.A., Ng, L., Winslow, B., Cain, N., Mihalas, S., Wang, Q., Lau, C., Kuan, L., Henry, A.M., et al. (2014). A mesoscale connectome of the mouse brain. *Nature* 508, 207–214.
- Okuda, K., Kobayashi, S., Fukaya, M., Watanabe, A., Murakami, T., Hagiwara, M., Sato, T., Ueno, H., Ogonuki, N., Komano-Inoue, S., et al. (2017). CDKL5 controls postsynaptic localization of GluN2B-containing NMDA receptors in the hippocampus and regulates seizure susceptibility. *Neurobiol. Dis.* 106, 158–170.
- Okuda, K., Takao, K., Watanabe, A., Miyakawa, T., Mizuguchi, M., and Tanaka, T. (2018). Comprehensive behavioral analysis of the *Cdkl5* knockout mice revealed significant enhancement in anxiety- and fear-related behaviors and impairment in both

acquisition and long-term retention of spatial reference memory. *PLoS ONE* *13*, e0196587.

O'Hare, J.K., Ade, K.K., Sukharnikova, T., Van Hooser, S.D., Palmeri, M.L., Yin, H.H., and Calakos, N. (2016). Pathway-Specific Striatal Substrates for Habitual Behavior. *Neuron* *89*, 472–479.

Penzes, P., Cahill, M.E., Jones, K.A., VanLeeuwen, J.-E., and Woolfrey, K.M. (2011). Dendritic spine pathology in neuropsychiatric disorders. *Nat Neurosci* *14*, 285–293.

Poulin, J.-F., Tasic, B., Hjerling-Leffler, J., Trimarchi, J.M., and Awatramani, R. (2016). Disentangling neural cell diversity using single-cell transcriptomics. *Nat Neurosci* *19*, 1131–1141.

Qiu, S., Anderson, C.T., Levitt, P., and Shepherd, G.M.G. (2011). Circuit-specific intracortical hyperconnectivity in mice with deletion of the autism-associated Met receptor tyrosine kinase. *31*, 5855–5864.

Reim, D., Distler, U., Halbedl, S., Verpelli, C., Sala, C., Bockmann, J., Tenzer, S., Boeckers, T.M., and Schmeisser, M.J. (2017). Proteomic Analysis of Post-synaptic Density Fractions from Shank3 Mutant Mice Reveals Brain Region Specific Changes Relevant to Autism Spectrum Disorder. *Front Mol Neurosci* *10*, 26.

Ricciardi, S., Ungaro, F., Hambrock, M., Rademacher, N., Stefanelli, G., Brambilla, D., Sessa, A., Magagnotti, C., Bachi, A., Giarda, E., et al. (2012). CDKL5 ensures excitatory synapse stability by reinforcing NGL-1-PSD95 interaction in the postsynaptic compartment and is impaired in patient iPSC-derived neurons. *Nat. Cell Biol.* *14*, 911–923.

Rubenstein, J.L.R., and Merzenich, M.M. (2003). Model of autism: increased ratio of excitation/inhibition in key neural systems. *Genes Brain Behav.* *2*, 255–267.

Rusconi, L., Salvatoni, L., Giudici, L., Bertani, I., Kilstrup-Nielsen, C., Broccoli, V., and Landsberger, N. (2008). CDKL5 Expression Is Modulated during Neuronal Development and Its Subcellular Distribution Is Tightly Regulated by the C-terminal Tail. *J. Biol. Chem.* *283*, 30101–30111.

Sahin, M., and Sur, M. (2015). Genes, circuits, and precision therapies for autism and related neurodevelopmental disorders. *Science* *350*, aab3897–aab3897.

Sala, Della, G., Putignano, E., Chelini, G., Melani, R., Calcagno, E., Michele Ratto, G., Amendola, E., Gross, C.T., Giustetto, M., and Pizzorusso, T. (2016). Dendritic Spine Instability in a Mouse Model of CDKL5 Disorder Is Rescued by Insulin-like Growth Factor 1. *Biol. Psychiatry* *80*, 302–311.

Sankoorikal, G.M.V., Kaercher, K.A., Boon, C.J., Lee, J.K., and Brodtkin, E.S. (2006). A mouse model system for genetic analysis of sociability: C57BL/6J versus BALB/cJ inbred mouse strains. *Biol. Psychiatry* *59*, 415–423.

- Scala, E., Ariani, F., Mari, F., Caselli, R., Pescucci, C., Longo, I., Meloni, I., Giachino, D., Bruttini, M., Hayek, G., et al. (2005). CDKL5/STK9 is mutated in Rett syndrome variant with infantile spasms. *J. Med. Genet.* *42*, 103–107.
- Sekiguchi, M., Katayama, S., Hatano, N., Shigeri, Y., Sueyoshi, N., and Kameshita, I. (2013). Identification of amphiphysin 1 as an endogenous substrate for CDKL5, a protein kinase associated with X-linked neurodevelopmental disorder. *Arch. Biochem. Biophys.* *535*, 257–267.
- Shcheglovitov, A., Shcheglovitova, O., Yazawa, M., Portmann, T., Shu, R., Sebastiano, V., Krawisz, A., Froehlich, W., Bernstein, J.A., Hallmayer, J.F., et al. (2013). SHANK3 and IGF1 restore synaptic deficits in neurons from 22q13 deletion syndrome patients. *Nature* *503*, 267–271.
- Shepherd, G.M.G., and Katz, D.M. (2011). Synaptic microcircuit dysfunction in genetic models of neurodevelopmental disorders: focus on Mecp2 and Met. *Curr. Opin. Neurobiol.* *21*, 827–833.
- Silbereis, J.C., Pochareddy, S., Zhu, Y., Li, M., and Sestan, N. (2016). The Cellular and Molecular Landscapes of the Developing Human Central Nervous System. *Neuron* *89*, 248–268.
- Sousa, A.M.M., Meyer, K.A., Santpere, G., Gulden, F.O., and Sestan, N. (2017). Evolution of the Human Nervous System Function, Structure, and Development. *Cell* *170*, 226–247.
- Szafranski, P., Golla, S., Jin, W., Fang, P., Hixson, P., Matalon, R., Kinney, D., Bock, H.-G., Craigen, W., Smith, J.L., et al. (2015). Neurodevelopmental and neurobehavioral characteristics in males and females with CDKL5 duplications. *Eur. J. Hum. Genet.* *23*, 915–921.
- Tang, S., Wang, I.-T.J., Yue, C., Takano, H., Terzic, B., Pance, K., Lee, J.Y., Cui, Y., Coulter, D.A., and Zhou, Z. (2017). Loss of CDKL5 in Glutamatergic Neurons Disrupts Hippocampal Microcircuitry and Leads to Memory Impairment in Mice. *J. Neurosci.* *37*, 7420–7437.
- Tao, J., Van Esch, H., Hagedorn-Greiwe, M., Hoffmann, K., Moser, B., Raynaud, M., Sperner, J., Fryns, J.-P., Schwinger, E., Gécz, J., et al. (2004). Mutations in the X-linked cyclin-dependent kinase-like 5 (CDKL5/STK9) gene are associated with severe neurodevelopmental retardation. *Am. J. Hum. Genet.* *75*, 1149–1154.
- Trazzi, S., Fuchs, C., Viggiano, R., De Franceschi, M., Valli, E., Jedynek, P., Hansen, F.K., Perini, G., Rimondini, R., Kurz, T., et al. (2016). HDAC4: a key factor underlying brain developmental alterations in CDKL5 disorder. *Hum. Mol. Genet.* *ddw231*.
- Tremblay, R., Lee, S., and Rudy, B. (2016). GABAergic Interneurons in the Neocortex: From Cellular Properties to Circuits. *Neuron* *91*, 260–292.

- Tsai, P.T., Hull, C., Chu, Y., Greene-Colozzi, E., Sadowski, A.R., Leech, J.M., Steinberg, J., Crawley, J.N., Regehr, W.G., and Sahin, M. (2012). Autistic-like behaviour and cerebellar dysfunction in Purkinje cell Tsc1 mutant mice. *Nature* 488, 647–651.
- Tyson, J.A., and Anderson, S.A. (2014). GABAergic interneuron transplants to study development and treat disease. *Trends Neurosci.* 37, 169–177.
- UniProt Consortium, T. (2018). UniProt: the universal protein knowledgebase. *Nucleic Acids Res.* 46, 2699–2699.
- Wang, D.D., and Kriegstein, A.R. (2008). GABA regulates excitatory synapse formation in the neocortex via NMDA receptor activation. *J. Neurosci.* 28, 5547–5558.
- Wang, I.-T.J., Wang, I.T.J., Allen, M., Allen, M., Goffin, D., Goffin, D., Zhu, X., Zhu, X., Fairless, A.H., Fairless, A.H., et al. (2012). Loss of CDKL5 disrupts kinome profile and event-related potentials leading to autistic-like phenotypes in mice. *109*, 21516–21521.
- Warren, M.S., Bradley, W.D., Gourley, S.L., Lin, Y.-C., Simpson, M.A., Reichardt, L.F., Greer, C.A., Taylor, J.R., and Koleske, A.J. (2012). Integrin $\beta 1$ signals through Arg to regulate postnatal dendritic arborization, synapse density, and behavior. *32*, 2824–2834.
- Weaving, L.S., Christodoulou, J., Williamson, S.L., Friend, K.L., McKenzie, O.L.D., Archer, H., Evans, J., Clarke, A., Pelka, G.J., Tam, P.P.L., et al. (2004). Mutations of CDKL5 Cause a Severe Neurodevelopmental Disorder with Infantile Spasms and Mental Retardation. *Am. J. Hum. Genet.* 75, 1079–1093.
- Wong, R.O.L., and Ghosh, A. (2002). Activity-dependent regulation of dendritic growth and patterning. *Nat Rev Neurosci* 3, 803–812.
- Yizhar, O., Fenno, L.E., Prigge, M., Schneider, F., Davidson, T.J., O’Shea, D.J., Sohal, V.S., Goshen, I., Finkelstein, J., Paz, J.T., et al. (2011). Neocortical excitation/inhibition balance in information processing and social dysfunction. *Nature* 477, 171–178.
- Young, P., Qiu, L., Wang, D., Zhao, S., Gross, J., and Feng, G. (2008). Single-neuron labeling with inducible Cre-mediated knockout in transgenic mice. *Nat Neurosci* 11, 721–728.
- Zeisel, A., Muñoz-Manchado, A.B., Codeluppi, S., Lönnerberg, P., La Manno, G., Juréus, A., Marques, S., Munguba, H., He, L., Betsholtz, C., et al. (2015). Brain structure. Cell types in the mouse cortex and hippocampus revealed by single-cell RNA-seq. *Science* 347, 1138–1142.
- Zhang, Y., Chen, K., Sloan, S.A., Bennett, M.L., Scholze, A.R., O’Keeffe, S., Phatnani, H.P., Guarnieri, P., Caneda, C., Ruderisch, N., et al. (2014). An RNA-sequencing transcriptome and splicing database of glia, neurons, and vascular cells of the cerebral cortex. *J. Neurosci.* 34, 11929–11947.

Zhu, Y.-C., Li, D., Wang, L., Lu, B., Zheng, J., Zhao, S.-L., Zeng, R., and Xiong, Z.-Q. (2013). Palmitoylation-dependent CDKL5-PSD-95 interaction regulates synaptic targeting of CDKL5 and dendritic spine development. *110*, 9118–9123.